

# **Numerical modeling of submarine hydrothermal fluid flow**

Dissertation

zur Erlangung des Doktorgrades

der Mathematisch-Naturwissenschaftlichen Fakultät

der Christian-Albrechts-Universität zu Kiel

vorgelegt von

**Nasser Bani Hassan**

Helmholz-Zentrum für Ozeanforschung (GEOMAR)

Kiel, 2012



*To Nazila*



## Erklärung

Hiermit erkläre ich, dass die vorliegende Abhandlung, abgesehen von der Beratung der Betreuer nach Inhalt und Form, meine eigene Arbeit ist. Bisher ist die Arbeit noch nicht an anderer Stelle im Rahmen eines Prüfungsverfahrens vorgelegt worden.

Nasser Bani Hassan



Referent:	Prof. Dr. Lars H. Rüpke
Koreferent:	Prof. Dr. Colin W. Devey
Tag der mündlichen Prüfung:	14 September 2012
Zum Druck genehmigt:	14 September 2012

Der Dekan  
Prof. Dr. Wolfgang J. Duschl



## Acknowledgements

First and foremost I would like to express my deepest gratitude to my advisor Prof. Dr. Lars Rüpke for his excellence guidance, caring, patience, and providing me with an excellent atmosphere for doing research. I appreciate all his contributions of time, ideas and funding to make my PhD experience productive and stimulating even during tough times in the PhD pursuit. I would also thank Prof. Dr. Colin Devey for advising me as the second supervisor and helpful discussions about new findings of hydrothermal activities and providing useful literatures from time to time.

I would also thank Dr. Karthik Iyer who was always willing to assist and give his best suggestions. His programming expertise always served me as a good example when implementing a new code or reorganizing an old one. I have to specially mention long-standing co-workers: Sonja Theissen-Krah, Ewa Burwicz and Christine Andersen. Together, we proved that we can be not only good partners but also friends and people who believe in each other. I am very grateful to all my colleagues at the GEOMAR research center. The atmosphere has always been a perfect source of motivation.

I want to express my deep thanks to Prof. Dr. Christian Berndt who provided 3D seismic data from Gjallar Ridge area and helped me with open arms to interpret it. I would also thank Prof. Andrea Borgia for helpful discussions about the observations in submarine and subaerial settings.

I would also acknowledge Integrated School of Ocean Sciences (ISOS) which provided a good interdisciplinary atmosphere to become familiar with other aspects of related sciences as well as funding several activities during my studies.

I am deeply and forever indebted to my parents. They have always been supporting me and encouraging me with their best wishes.

Finally, I offer my sincerest gratitude to my wife, Nazila. She has always been there cheering me up and stood by me through the good times and the bad.



# Abstract

Mid-ocean ridges and volcanic passive continental margins are prime regions to explore active and extinct hydrothermal systems. In both settings, a large number of hydrothermal vents have already been discovered by direct observations and/or geophysical surveys. The growing interest in these systems results from their relevance for different fields of marine sciences. For example, commercially interesting ore deposits form as a byproduct of hydrothermal venting at the seafloor, unique ecosystems evolve around submarine vent sites, and hydrothermal systems driven by sill intrusions into organic sediments are related to hydrocarbon maturation and even venting of greenhouse gases into the atmosphere. Numerical simulations of hydrothermal fluid flow can help to gain a quantitative understanding of the subsurface physicochemical processes that control these systems. This thesis contributes to a better understanding of hydrothermalism in oceanic and continental settings by presenting a newly developed hydrothermal flow model and two case studies of hydrothermal flow at mid-ocean ridges and volcanic passive margins.

To explore the effects of bathymetric relief on hydrothermal fluid flow in submarine settings, a systematic study has been carried out using 375 simulations. These simulations show that temperature-induced pressure variations in the subsurface result in the deviation of hydrothermal plumes towards bathymetric highs in submarine settings. The plume deviation from its origin is directly related to the surface slope and depth of the heat source. A case study for the fast-spreading East Pacific Rise at 9° 30'N shows that bathymetric effects help to focus venting directly onto the ridge axis – only if bathymetry is taken into account can across axis fluid flow be reconciled with exclusive on-axis venting. A second case study for the slow-spreading Lucky Strike segment of the Mid-Atlantic Ridge shows that also here venting is likely to occur at local bathymetric highs.

The effects of hydrothermal convection triggered by sill intrusions in continental settings have been explored in a case-study for the Gjallar Ridge area on the Norwegian margin. This area is affected by a swarm of sill intrusions originated from North-Atlantic continental break-up during the Paleocene-Eocene transition as well as pre-break-up faults resulting from

extensional tectonics. The structures are interpreted using 3D multichannel seismic data in combination with a structural and thermal reconstruction of the margin using TECMOD software. The reconstructed temperature is used as initial condition for sediments prior to sill injection and the detailed thermal history of sediments is modeled by a 2D fluid flow simulation. The simulation results show that high-temperature venting ( $>200^{\circ}\text{C}$ ) occurs less than 1000 years following sill emplacement. The faults play strong roles for transferring the fluids to far-off regions. As a result of circulating hot fluids, the maturity of sedimentary rocks is greatly enhanced, especially where the hot fluids are trapped below impermeable sills during their ascent, thereby suggesting potential zones for future hydrocarbon explorations.

Furthermore, solution strategies for modeling hydrothermal fluid flow by finite element, finite volume and semi-Lagrangian methods are explained in particular in order to find out how the temperature equation is solved. Different schemes of fully-implicit, Crank-Nicolson and exponential for temperature diffusion and finite volume and semi-Lagrangian for temperature advection are evaluated. The results suggest that the most accurate method for solving temperature diffusion is Crank-Nicolson. However, other methods such as fully implicit and exponential are still valid. The mass conserving finite volume method is the most accurate method for solving temperature advection; however, limited time-stepping is its major drawback and thus semi-Lagrangian method is usually preferred. Therefore, the definition of optimum method is linked to the accuracy of interest and complexity of the media.

# Zusammenfassung

Mittelozeanischen Rücken und vulkanische passive Kontinentalränder sind wichtige Regionen zur Erforschung aktiver und erloschener hydrothermalsysteme. In beiden Gebieten ist bereits eine große Anzahl von hydrothermalen Quellen durch direkte Beobachtungen und/oder geophysikalische Untersuchungen entdeckt worden. Das wachsende Interesse an diesen Systemen ergibt sich aus ihrer Bedeutung für verschiedene Bereiche der Meereswissenschaften. Zum Beispiel bilden sich kommerziell interessante Erzlagerstätten als Nebenprodukt der hydrothermalen Aktivität am Meeresboden, einzigartige Ökosysteme besiedeln den Meeresboden rund um schwarze Raucher, hydrothermalsysteme welche durch intrusion von Lagergängen in organische Sedimente angetrieben werden stehen im Zusammenhang zur Bildung von Kohlenwasserstoffen und sogar zur Abgabe von Treibhausgasen in die Atmosphäre. Numerische Simulationen hydrothermaler Konvektion können helfen, ein quantitatives Verständnis der physikalisch-chemischen Prozesse im Meeresboden zu gewinnen, welche diese Systeme kontrollieren. . Diese Doktorarbeit trägt durch neue Modelle für hydrothermale Konvektion und Fallstudien an Mittelozeanischen Rücken und vulkanischen passiven Kontinentalrändern zu einem besseren Verständnis mariner und kontinentaler Hydrothermalsystemen bei.

Um die Wirkung bathymetrischen Reliefs auf submarine hydrothermale Fluidströmungen zu untersuchen, ist eine systematische Studie mit 375 Simulationen durchgeführt worden. Diese Simulationen zeigen, dass Temperatur-induzierte Druckschwankungen im Meeresbodenhydrothermale Fluide Richtung bathymetrische Höhen lenken. Die Abweichung der Fluide von ihrem Ursprung ist direkt abhängig von der Neigung der Oberfläche und Tiefe der Wärmequelle. Eine Fallstudie des schnell spreizenden Ostpazifischen Rückens (9° 30'N) zeigt, dass bathymetrische Effekte helfen hydrothermales Venting direkt auf der Rückenachse zu konzentrieren - nur wenn Bathymetrie berücksichtigt wird, kann Strömung quer zur Rückenachse mit Venting ausschließlich auf der Achse in Einklang gebracht werden. Eine zweite Fallstudie des langsam spreizenden Lucky Strike-Segments des Mittelatlantischen Rückens zeigt, dass auch dort Venting mit hoher Wahrscheinlichkeit an lokalen bathymetrischen Höhen auftritt.

Die Auswirkungen hydrothermaler Konvektion, die von intrusiven Lagergängen angetrieben wird, ist in kontinentaler Umgebungen in einer Fallstudie des Gjallar Rückens am norwegischen Kontinentalrand erforscht

worden. Dieses Gebiet ist von einem Schwarm Lagergänge beeinflusst welche während des Aufbrechens des nordatlantischen Kontinents im Paläozän-Eozän Übergang intrudiert sind sowie von Verwerfungen die vor dem Kontinentalaufbruch durch Extensionstektonik entstanden sind. Die Strukturen sind mit Hilfe von 3D-Multikanal-seismischen Daten in Kombination mit einer strukturellen und thermischen Rekonstruktion des Kontinentalrandes mit TECMOD Software interpretiert worden. Die rekonstruierte Temperatur wird als Anfangsbedingung für die Sedimente vor der Intrusion der Lagergänge verwendet und die detaillierte thermische Entwicklung der Sedimente wird durch eine 2D Strömungssimulation modelliert. Die Simulationsergebnisse zeigen, dass Hochtemperatur-Venting ( $>200^{\circ}\text{C}$ ) weniger als 1000 Jahre nach Intrusion der Lagergänge auftritt. Die Verwerfungen spielen eine wichtige Rolle für den Transfer der Fluide zu weit entfernten Regionen. Als Folge der zirkulierenden heißen Fluide, ist die Entstehung von Sedimentgesteinen stark beschleunigt, insbesondere dort, wo die heißen Flüssigkeiten während ihres Aufstiegs unter undurchlässigen Lagergängen eingeschlossen sind. Dies sind potentielle Zonen für zukünftige Kohlenwasserstoff Erkundungen.

Darüber hinaus werden Lösungsstrategien für die Modellierung hydrothormaler Konvektion mit Finiten Elementen, Finiten Volumen und Semi-Lagrange Methoden erklärt insbesondere um herauszufinden, wie die Temperatur Gleichung am präzisesten gelöst wird. Unterschiedliche Verfahrensweisen für Wärmediffusion: voll-implizit, Crank-Nicolson und exponentiell -und für Wärmeadvektion: Finite Volumen und Semi-Lagrange wurden ausgewertet. Die Ergebnisse legen nahe, dass die die Crank-Nicolson Methode zur Lösung von Wärmediffusion die genaueste ist, jedoch sind auch andere Methoden wie die voll implizite und die exponentielle weiterhin gültig. Die massenerhaltende Finite-Volumen Methode ist die genaueste Methode zur Lösung der Wärmeadvektion, allerdings ist hier die Begrenzung des Zeitschrittes der große Nachteil und somit wird in der Regel die Semi-Lagrange-Methode bevorzugt. Deshalb hängt die Definition der optimalen Methode von der benötigten Genauigkeit und der Komplexität des Mediums ab.

# Nomenclature

Latin letters	Description	Unit
$O$	Area of finite volumes	$m^2$
$A$	Amplitude	$m$
$Ar$	Arrhenius factor	$K$
$B$	MINMOD criterion	
$C_p$	Specific heat capacity	$J\ kg^{-1}\ K^{-1}$
$D$	Relative plume deviation	
$E$	Activation energy	$J\ mol^{-1}$
$H$	Total energy stored in system	$J$
$K$	Reaction rate	
$J$	Jacobian matrix	
$L$	Length of segment	$m$
$M$	Diffusion parameter	$Wm^{-3}K^{-1}s$
$N$	Shape function	
$Nu$	Nusselt number	
$P$	Pressure	$Pa$
$Q$	Source term	
$R$	Ideal gas constant	
$Ra$	Rayleigh number	
$Rs$	Residual	
$Rc$	Reaction rate	
$S$	Saturation	

$Sc$	Specific surface area	$m^2$
$T$	Temperature	$K$
$Tr$	Transformation ratio	
$V$	Specific volume of fluid	
$W$	Wavelength	$m$
$X$	Coordinates	
$c$	Coefficient	
$d$	Thermal diffusivity	
$f$	Arbitrary function	
$g$	Gravitational acceleration	$m s^{-2}$
$h$	Enthalpy	$JKg^{-1}$
$k$	Matrix permeability	$m^2$
$l$	Length of Gaussian function	$m$
$m$	Mass	$Kg$
$\bar{n}$	Outward-pointing unit normal to segments	
$nel$	Number of elements	
$nip$	Number of integration points	
$nnod$	Number of nodes	
$r$	Area of control volume	$m^2$
$t$	Time	$s$
$\bar{u}$	Fluid velocity	$m s^{-1}$
$w$	Weight functions	
$x$	Nodal geometry	$m$
$y$	Nodal geometry	$m$

$z$	Depth of domain	$m$
$z_0$	Compaction length scale	$m$

<b>Greek letters</b>	<b>Description</b>	<b>Unit</b>
$K$	Global stiffness matrix	
$\Gamma$	Domain boundary	
$\Omega$	Computational domain	
$\Pi$	Finite control volume	
$\Upsilon$	Vector of nodal applied forces	
$\alpha$	Thermal expansion coefficient	
$\beta$	Compressibility	
$\varepsilon$	Coefficient	$K^{-1}$
$\theta$	Plume deviation angle	
$\mu$	Dynamic viscosity of fluid	
$\eta$	Scaling factor	
$\lambda$	Thermal conductivity	$Pa\ s$
$\kappa$	Matrix of domain characteristics	
$\phi$	Matrix porosity	$W\ m^{-1}\ K^{-1}$
$\tau$	Average radius of finite volumes	
$\delta$	Coefficient	
$\rho$	Fluid density	

$\omega$	Integration weight functions	$m$
$v$	Force vector for an element	
		$kg\ m^{-3}$

## Subscripts and superscripts

$T$	Transpose
$m$	matrix
$f$	fluid
$t$	total

## Abbreviations

<i>CFD</i>	Computational Fluid Dynamics
<i>CFL</i>	Courant Fredrich Levy
<i>EOS</i>	Equation Of State
<i>FDM</i>	Finite Difference Method
<i>FEM</i>	Finite Element Method
<i>FVM</i>	Finite Volume Method
<i>GFEM</i>	Generalized Finite Element Method
<i>IFDM</i>	Integrated Finite Difference Method
<i>MOR</i>	Mid Ocean Ridge
<i>PDE</i>	Partial Differential Equation

<i>PETM</i>	Paleocene-Eocene Thermal Maximum
<i>SLM</i>	Semi-Lagrangian Method
<i>TTI</i>	Time-Temperature Index
<i>TWT</i>	Two-Way Travel time
<i>VMS</i>	Volcanogenic Massif Sulfides
<i>WRM</i>	Weighted Residual Method
<i>XFEM</i>	Extended Finite Element Method

# Contents

<b>1. Introduction.....</b>	<b>1</b>
1.1. Hydrothermal systems.....	1
1.1.1. Mid-Ocean Ridge hydrothermal systems.....	2
1.1.2. Passive margin hydrothermal systems .....	5
1.2. Discovery of hydrothermal vents.....	6
1.2.1. Direct observations .....	6
1.2.2. Geophysical assessments .....	7
1.3. Hydrothermal modeling and thesis objectives .....	9
1.4. Thesis outline .....	14
<b>2. Controls of bathymetric relief on hydrothermal fluid flow at mid-ocean ridges .....</b>	<b>19</b>
2.1. Introduction.....	20
2.2. Hydrothermal convection model.....	23
2.2.1. Governing equations .....	23
2.2.2. Numerical implementation.....	25
2.3. Synthetic studies .....	27
2.3.1. Single bathymetric high .....	27
2.3.1.1. Model geometry and setup.....	27
2.3.1.2. Reference simulation.....	28
2.3.1.3. Non-reference simulations .....	28
2.3.2. Multiple bathymetric highs .....	32
2.3.2.1. Model geometry and setup.....	32
2.3.2.2. Reference simulation.....	32
2.3.2.3. Non-reference simulations .....	33
2.4. Case studies.....	38
2.4.1. East Pacific Rise vent field (9° 30'N).....	38

2.4.1.1.	Geological setting .....	38
2.4.1.2.	Model setup.....	39
2.4.1.3.	Results.....	41
2.4.2.	Lucky Strike vent field.....	43
2.4.2.1.	Geological setting .....	43
2.4.2.2.	Model setup.....	44
2.4.2.3.	Results.....	45
2.5.	Conclusions.....	47
<b>3.</b>	<b>The effects of sill intrusions on hydrothermal flow and thermal maturity in sedimentary basins: a case study from the Gjallar Ridge, off Norway.....</b>	<b>51</b>
3.1.	Introduction.....	52
3.2.	Geological setting of Gjallar Ridge .....	55
3.3.	Modeling approach .....	56
3.3.1.	One-dimensional basin reconstruction.....	57
3.3.2.	Two-dimensional fluid flow.....	57
3.4.	Basin analysis.....	62
3.4.1.	Geophysical assessment and interpretation.....	62
3.4.2.	Basin reconstruction.....	65
3.4.3.	Fluid flow simulation driven by sill intrusions .....	68
3.4.3.1.	Model setup.....	68
3.4.3.2.	Thermal evolution .....	71
3.4.4.	Discussion .....	74
3.5.	Conclusion .....	82
<b>4.</b>	<b>Solution strategies for modeling hydrothermal systems.....</b>	<b>85</b>
4.1.	Introduction.....	85
4.2.	Modeling concepts .....	88
4.2.1.	Hydrothermal flow equations.....	88
4.2.2.	Model assumptions .....	90

4.2.3.	Implementation .....	91
4.3.	Numerical discretization .....	91
4.3.1.	Finite Element Method.....	91
4.3.2.	Finite Volume Method.....	100
4.3.3.	Semi-Lagrangian.....	106
4.4.	Solution methods .....	107
4.4.1.	Advection schemes .....	107
4.4.2.	Diffusion schemes.....	111
4.4.2.1.	Analytical solution .....	113
4.4.2.2.	Explicit method.....	114
4.4.2.3.	Fully implicit method.....	115
4.4.2.4.	Crank-Nicolson method .....	116
4.4.2.5.	Exponential method .....	117
4.4.2.6.	Comparison .....	118
4.4.3.	Nusselt number .....	121
4.4.4.	Hydrothermal convection.....	123
<b>5.</b>	<b>Conclusions.....</b>	<b>131</b>
<b>6.</b>	<b>Bibliography .....</b>	<b>135</b>

## List of figures

Figure 1-1: The world's distribution of hydrothermal vent fields. ....	2
Figure 1-2: Phase diagram for pure water.....	11
Figure 1-3: Pressure and temperature pattern in submarine and subaerial settings.....	13
Figure 2-1: Simulations with a single plume and a single bathymetric high at steady-state. ....	30
Figure 2-2: a) Relative plume deviation as a function of surface slope for different model depths. b) The observed relative plume deviation for a single plume for different amplitudes, wavelengths and model depths against the relative plume deviation.....	31
Figure 2-3: Temperature plot of the reference simulation with multiple plumes and constant temperature bottom heat source.. ....	33
Figure 2-4: Simulation results showing the temperature fields for a selected number of variable bathymetric models. ....	35
Figure 2-5: Outward mass flux of vent fluid through the upper half of bathymetric high.....	37
Figure 2-6: Permeability structures used in the simulations of East Pacific Rise 9°30'N.....	41
Figure 2-7: Simulation results for the hydrothermal vent field at East Pacific Rise 9°30'N.....	42
Figure 2-8: Permeability structure defined for Lucky-Strike vent field.....	45
Figure 2-9: Two-dimensional cross-section of modeled temperature field for the Lucky Strike vent field at early and late stages. ....	46
Figure 3-1: Location of Gjallar Ridge area in Vøring Basin. ....	64
Figure 3-2: Interpreted 3D seismic reflection data in Gjallar Ridge area. ....	65
Figure 3-3: Temperature field through time obtained using 1D basin reconstruction. ....	67
Figure 3-4: Measured vitrinite reflectance and temperature in the exploration well 6704/12.....	67
Figure 3-5: A selected transect in the seismic cube on Gjallar Ridge.....	70
Figure 3-6: Thermal evolution of Gjallar Ridge after sill emplacement.....	73

Figure 3-7: Vitrinite reflectance calculated for the transect.....	80
Figure 3-8: One dimensional vitrinite reflectance at profiles in the distances of 2.2, 8.6, 12.8 and 23 km. ....	81
Figure 4-1: One dimensional finite elements. ....	93
Figure 4-2: Two dimensional unstructured finite element mesh. ....	93
Figure 4-3: Global and local coordinates of elements. ....	95
Figure 4-4: Bilinear shape functions for triangular element. ....	95
Figure 4-5: One-dimensional finite volumes. ....	101
Figure 4-6: Two-dimensional unstructured finite volume mesh.....	102
Figure 4-7: schematic model for semi-Lagrangian advection method.....	106
Figure 4-8: Total energy stored in the matrix by Semi-Lagrangian method and Finite Volume Method. ....	110
Figure 4-9: Synthetic model of spinning heat source through porous matrix..	111
Figure 4-10: The analytical solution of a localized heat source in the middle of domain after 150 ka of conduction. ....	113
Figure 4-11: Temperature ratio during one time step as a function of a diffusion parameter.....	119
Figure 4-12: Maximum difference in temperature of domain center between numerical and analytical solutions calculated at each time step. .	119
Figure 4-13: The misfit between the analytical and numerical schemes after 150 ka of conduction .....	121
Figure 4-14: Calculation of Nusselt number in a dimensionless system for Rayleigh numbers of 50 and 100.....	123
Figure 4-15: Calculation of Nusselt number as a function of domain resolution.. .....	123
Figure 4-16: Hydrothermal circulation in an open box after 3000 years of convection .....	124
Figure 4-17: Vent temperature at the seafloor for simulations carried out by Semi-Lagrangian Method and Finite Volume Method.....	126
Figure 4-18: Volume fraction of vent fluids as a function of temperature using Semi-Lagrangian method and Finite Volume Method. ....	127

## List of tables

Table 1: List of model parameters .....	25
Table 2: Model Parameters for Gjallar Ridge case study. ....	60



# Chapter 1

## Introduction



# **Introduction**

## **1.1. Hydrothermal systems**

Hydrothermal systems develop where fluids can readily circulate through the Earth's crust and the thermal gradient is high enough to drive thermal convection. Examples where active hydrothermal systems exist in nature include Mid-Ocean Ridges (MOR), subduction zones, back-arc basins and hotspots. In addition, extinct hydrothermal systems have been reported from volcanic passive margins where igneous intrusions were injected into sedimentary rocks. In this thesis, the physics of hydrothermal fluid flow at mid-ocean ridges and passive margins are explored using numerical modeling techniques.

To date, a total number of 589 submarine vent fields have been discovered of which 533 are active (confirmed and inferred) and 56 are inactive ([interridge.org/irvents/ventfields\\_list\\_all](http://interridge.org/irvents/ventfields_list_all)). Figure 1-1 shows the world's distribution of submarine vent fields. Hydrothermal circulations are estimated to be responsible for transferring 25% of the Earth's total heat loss and 35% of the ocean's heat flux (Von Herzen and Uyeda, 1963; Sclater et al., 1980; Stein and Stein, 1994; Lowell et al., 1995). McKenzie (2003) estimated that it takes about one million years to cycle the equivalent water of the global ocean through the hydrothermal systems at the sea floor. The hydrothermal zones are mainly recharged by seawater penetrating into the porous crust. The brine released by

## Introduction

magma is another source of water, particularly in subduction zones. Meteoric water and groundwater together with magmatic and metamorphic water are recharge sources for hydrothermal fluid in terrestrial systems (Audetat et al., 1998).

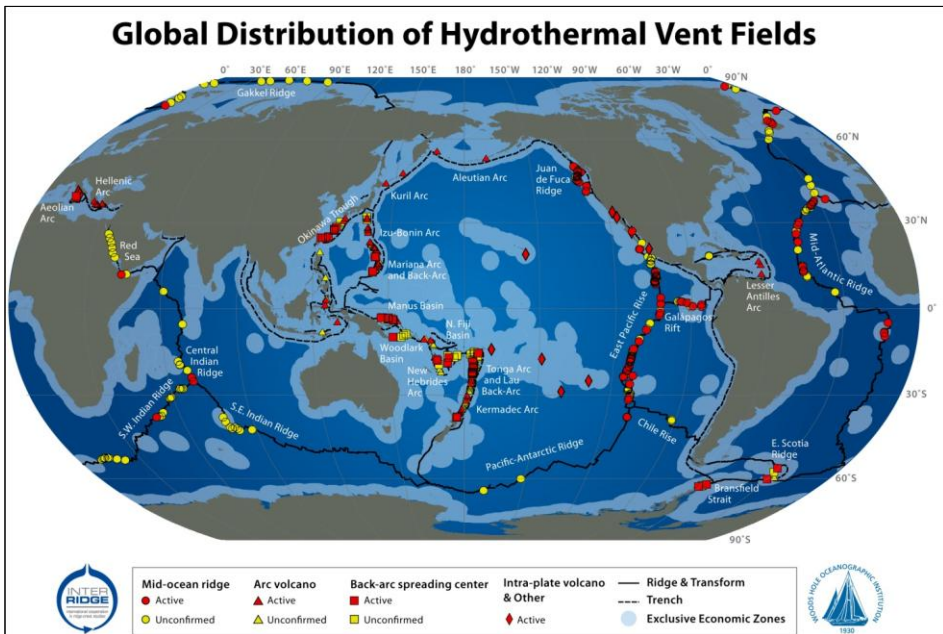


**Figure 1-1:** The world's distribution of hydrothermal vent fields ([interridge.org/irvents/maps](http://interridge.org/irvents/maps)).

### 1.1.1. Mid-Ocean Ridge hydrothermal systems

New oceanic crust is continuously created along the mid-ocean ridge systems. Upon cooling, the newly formed crust becomes porous and permeable. Seawater can, therefore, percolate through the rocks. The magma originated from melting mantle rocks heats up the infiltrated water and makes it buoyant. The buoyant hot water vents back into oceans as a mineral rich hydrothermal fluid. In the meantime, cold seawater continuously recharges the systems. In this process, large hydrothermal plumes originating from heat source form.

Mid-Ocean Ridges are generally characterized in terms of spreading rate to two end-members of fast- and slow-spreading ridges. Fast spreading ridges (full spreading rate greater than 90 mm/yr) such as the East Pacific Rise, generally show smooth bathymetric relief, usually with an axial high. The seafloor slopes away from the ridge axis up to several kilometers (Carbotte and Macdonald, 1994). Fast spreading ridges are likely to be in a steady state with a stable melt lens located below the ridge axis (Morgan and Chen, 1993). The hydrothermal vent-sites in most of the fast spreading ridges are on-axis (Baker and German, 2004). By contrast, slow-spreading ridges (<55 mm/yr) such as the Mid-Atlantic Ridge, usually exhibit wide and large rift valleys with bathymetric variations exceeding 1000 meters (e.g. Smith and Cann, 1992; Tolstoy et al., 2001). So far, the only stable melt lens is found below the Lucky Strike vent field on the Mid-Atlantic ridge (Singh et al., 2006). Observations from vent sites show that vent fields in slow spreading ridges could occur both on- and off-axis (e.g. on-axis venting at Lucky Strike (Dusunur et al., 2009); off-axis venting at TAG deMartin et al., 2007). In intermediate spreading ridges (55-90 mm/yr) such as Galapagos 85°54'W, the bathymetric variation and magma supply are somewhat between fast and slow spreading ridges. The axial high in intermediate spreading ridges is primarily a volcanic construction and it reaches up to a few hundred meters (Carbotte and Macdonald, 1994).

Faulting is a logical consequence of extensional tectonics during seafloor spreading. Normal faulting is common at near axis regions in slow-spreading ridges as the lithosphere is strong enough to support shear stresses on the axis. In contrast, there could only be a few normal faults on the axis of fast-spreading ridges and this is explained by a thin and weak lithosphere (Carbotte and Macdonald, 1994; Macdonald, 2001). In fact, deep faults and fracture networks exhibit strong controls on the location of the vent sites as they provide high permeability pathways (Anderson and Fairley, 2008). The permeability of the rocks as well as fracture connections have to be sufficient enough to attain considerable convection. In slow spreading ridges where tectonic activities are

## Introduction

---

remarkable, it is not uncommon to expect off-axis venting by bounding faults (Lowell et al., 1995).

The rate of magma supply can affect the ridge morphology as another important factor (Macdonald, 2001). The burial depth of heat source is likely inversely dependent on the spreading rate. For example, at intermediate- and fast spreading ridges, magma is buried in shallow depths, approximately 1-3 km beneath the seafloor (e.g. Buck et al., 1997; Carbotte et al., 1998). Estimations of heat source depth, calculated by Baker (2009) suggests that the depth of magma in slow spreading ridges is approximately 3-4 km. The Axial Magma Chamber discovered at Lucky Strike vent field (Singh et al., 2006) is consistent with these estimations.

A key feature, which strongly motivates scientists to explore hydrothermal fields, is the presence Volcanogenic Massif Sulfide (VMS) deposits that are associated with hydrothermal venting. The hot hydrothermal fluids react with the basaltic rocks thereby getting enriched in dissolved minerals. The mineral-rich fluids ascend towards the surface and as they cool upon contact with cold seawater, the dissolved minerals are released and form solid precipitates, such as volcanogenic massive sulfide ore deposits. These minerals deposits can accumulate around the vents as mounds or chimney structures shaped up to 45 m high (Lowell et al., 1995) and grow by up to 30 cm per day (Tivey, 1998).

In addition to metal deposits around hydrothermal vent sites, their unique ecosystems make them interesting to marine scientists. Biologists became interested in hydrothermal activities once tough extraordinary living organisms near hot springs were discovered and were explained to be a result of special environmental conditions around hydrothermal vent sites. Giant clams, tube worms and unique types of fishes are unusual creatures which have been adapted with the hydrothermal ecosystems. Since in the darkness of the abyssal oceans, there is no sunlight for photosynthesis at hydrothermal environments, the life depends on chemosynthesis instead. The chemosynthetic bacteria use chemical energy taken from oxidation of reduced gases dissolved in the hydrothermal vents (Lowell et al., 1995). These bacteria are capable to produce

organic material through the process of chemosynthesis and the basis of vent food chain. The discovery of these environments, therefore, began the dramatic shift in the perspective of scientists to elucidate the evolution and the origin of life by classification of species in hydrothermal ecosystems (Zierenberg, 2000). Corliss et al. (1981) suggested that the existence of primitive life forms could have begun near hydrothermal systems such as The Rose Garden.

### **1.1.2. Passive margin hydrothermal systems**

Passive margins form as a consequence of continental breakup and mark the transition between oceanic and continental crust. As a result of tectonic extension, the crust is pulled apart and becomes stretched and thinned. If the extension continues, continental break-up may occur.

Passive margins are classified to two types of volcanic and non-volcanic margins in terms of transitional crust. Non-volcanic passive margins, such as the Iberian margin, are formed when little mantle melting and volcanism occurs. The main characteristics of these margins are stretched continental crust and exhumed upper mantle (Boillot and Froitzhelm, 2001). In turn, volcanic passive margins, such as the Norwegian margin, are characterized by extensive magmatism and volcanism as well as thick lower crustal bodies with seismic P-wave velocities exceeding 7 km/s. Seaward dipping reflectors, indicative for breakup-related magmatism, are also distinct features of volcanic margins (Geoffroy, 2005; Gernigon et al., 2006).

Hydrothermal systems in the volcanic passive margins can potentially be driven by sill and dyke intrusions emplaced during continental break-up. The igneous intrusions in the volcanic passive margins can induce strong thermal convection, especially when large sill complexes are injected into sediments simultaneously. As the heat source is transient in such settings, the associated hydrothermal activity is likely short lived. In fact, duration of hydrothermal activity depends on several factors, including the thickness of the intrusions, their permeability, initial emplacement temperature of magma and matrix

heterogeneities. Although the hydrothermal systems in such settings become extinct rapidly, hot circulating fluids likely mature the organic matter in the sediments and produce hydrocarbon.

Another impact of fluid flow in the volcanic passive margins is climate change effects. It has been suggested that circulation of hydrothermal fluids at the Norwegian margin at the time of continental break up (~55 Ma) has led to massive release of carbon into ocean-atmosphere system (Svensen et al., 2004). It is hypothesized that considerable rapid changes in the climate is occurred during the Paleocene-Eocene Thermal Maximum (PETM). The period of the carbon release was less than 20,000 years during which the global temperature was increased by 5-8°C. Such large and rapid climate change could be a consequence of magma injection into sediments throughout the Paleocene-Eocene transition. The associated hydrothermal fluid flow may have triggered thermogenic methane release (McInerney and Wing, 2011).

## **1.2. Discovery of hydrothermal vents**

### **1.2.1. Direct observations**

Several observations from black-smokers at active hydrothermal systems have been recorded over the last decades. These observations provided a global pattern of hydrothermal fields. The earliest discoveries of submarine hydrothermal systems date back three decades when major hydrothermal fields such as TAG and Endeavour were found. As submarine hydrothermal vents are generally located at deep oceans, poor technical abilities restricted us to discover vent-sites until 1977. The first hydrothermal vent was monitored at the Galapagos rift in early 1977 reported by Corliss et al. (1979) using a deep-sea submersible called Alvin.

New technologies in deep diving instruments provide precise *in-situ* monitoring from deeper active hydrothermal vents. For example, Connelly et al. (2012) discovered the world's deepest known hydrothermal vent site using a deep-towed Side-scan Sonar TOBI, AVU autosub 6000 and ROTV HyBIS. This

vent site, located at the depth of 4960 m below sea level, is located at the Mid-Cayman Rise (MCR) in the Caribbean Sea. Moreover, detailed observations from bathymetric variations in vent fields are now possible thanks to state-of-the-art submersibles. For instance, a study by Ondreas et al. (2009) provided high-resolution bathymetry data from Lucky-Strike vent field using ROV Victor 6000.

Hydrothermal activities are different between fast- and slow-spreading ridges due to structural dissimilarities. It was initially thought that hydrothermal activities can only occur in fast spreading ridges, but black-smokers were surprisingly discovered in all types of ridges during exploration surveys (Baker and German, 2004). Besides, studies from individual vent fields along ridges with different spreading rates show that large-scale structures of deposits are more favorable in slow-spreading ridges as the convective system is less vigorous and venting is stable for longer time than fast spreading ridges (Cann et al., 1999).

Hydrothermal vents in spreading ridges can be either found on-axis (e.g. Lucky Strike (Singh et al., 2006), MAR 5°S (Koschinsky et al., 2008)) or off-axis (e.g. Nibelungen (Melchert et al., 2008), Lost City (Kelley et al., 2001), TAG (deMartin et al., 2007)). On-axis hydrothermal vents are generally results of recent volcanism, where a shallow axial magma chamber is present. By contrast, off-axis venting usually occurs where the region is tectonically active and the fluid can channel through the faults. Adjacent to high-temperature vent sites, low-temperature diffusive venting is usually abundant. A remarkable portion of heat loss in hydrothermal vent fields could be due to diffusive venting (Lowell et al., 1995).

### **1.2.2. Geophysical assessments**

Geophysical assessments are widely used for the discovery of both active and extinct hydrothermal systems. In fact, since there is no active fluid flow in extinct hydrothermal fields, it is not possible to detect the vent fields using direct observations. Most of the initial screening regarding exploration of black

## Introduction

---

smokers start in regional scale and further, more local studies and expeditions are run on the potential prospects. Several geophysical studies have been carried out since past decades to discover hydrothermal vents and to elucidate the structure of vent fields. The geophysical methods commonly used for discovery of vent fields are reflection seismic, gravity, magnetism and microseismicity.

Reflection seismic is the most accurate method to detect the sub-surface structures. However, seismic wave penetration depends on the structures, i.e. high impedance contrast between the structures cause strong reflection, thereby inhibiting wave penetration. Magmatic bodies, faults and fractures, etc. can be detected precisely from a seismic section. For example, structures such as magma chamber and bounding faults as well as the size and geometry of magma chamber are discovered by 2D reflection seismic along Lucky-Strike vent field (Singh et al. 2006). The accurate information about structures beneath seafloor may help us to understand the relationship between magmatic and tectonic processes in hydrothermal systems at MOR.

Beside the seismic methods, other geophysical methods also provide significant information beneath the hydrothermal zones. Gravity studies could facilitate detecting the magmatic hydrothermal activity. Magmatic bodies could be detected by gravity measurements if the density contrast is remarkable. For example, shallow sill complexes could presumably show positive bouguer anomaly. In addition, fluid flow affects the local Earth's gravity. For example, a numerical study by Todesco and Berrino (2005) in shallow magmatic hydrothermal system indicates that fluid density variation can produce a detectable micro-gravity anomaly.

Magnetic measurement is another method for detection of hydrothermal activity. In this method, the localized variations of Earth's total magnetic field are measured. Deposited minerals by hydrothermalism can be identified and mapped by magnetic surveys due to their magnetic properties. The magmatic body contains magnetic minerals such as magnetite. In certain environments, alteration of magnetic minerals to less magnetic minerals in hydrothermal systems is the source of reduced magnetization which can be detected from

seafloor. Although in vapor dominated systems, magnetite remains magnetic, short period of liquid dominated hydrothermal circulation above 150°C can entirely deplete magnetite by precipitation of clays such as Mg-rich smectite and chlorite (Alt, 1995; Hochstein and Soengkono, 1997 and Tivey, 2008). In some settings, substantial formation of magnetite leads to positive anomaly. The magnetite can be produced by serpentinization of ultramafic rocks (Dyment et al., 2005; Tivey, 2008) and/or deposition of minerals (e.g. Tivey, 1994).

Microseismicity is another geophysical method employed to explore the hydrothermal activities. Hydrothermal venting generally produces low seismicity that cannot be recorded by a single receiver and normally a set of stations is therefore used to detect and locate the hydrothermal vents. Based on microseismicity measurements in the southern Juan de Fuca Ridge, Sohn et al. (1995) suggested that the P- and S-wave arrivals and peaked spectra at discrete frequencies are likely related to hydraulic fracturing and can be a signature of a hydrothermal activity. Microseismicity could also reveal the depth of fluid penetration, as deep thermal fracturing can produce detectable pulses (Tolstoy et al., 2008).

### **1.3. Hydrothermal modeling and thesis objectives**

Numerical modeling can provide valuable information on the physics of subsurface hydrothermal processes and can thereby help to explain observations. An analytical solution for the physical processes is not plausible as the underlying equations are highly non-linear and coupled. Therefore, an approximate solution is achieved by numerical analysis. Numerical modeling of porous convection often suffers a number of limitations and assumptions in order to simplify the complicated processes. Most early studies were carried out by simplifying fluid properties, as the non-linear fluid properties may vary by orders of magnitude in different conditions of pressure and temperature. A number of earlier studies assumed constant fluid properties in the simulations (e.g. Cherkaoui and Wilcock, 1999). In realistic conditions, this assumption may

## Introduction

---

lead to variations in convection pattern as taking constant fluid properties suppresses the vigor of convection (Coumou et al., 2006). Other studies used the Boussinesq approximation in which transient density variations are taken sufficiently small to be neglected except in the buoyancy term (e.g. Wilcock, 1998; Schoofs and Hansen, 2000). Further studies assumed fully compressible fluids in the simulations, but pressure is steady state (Cathles, 1977).

Non-linear fluid properties are functions of pressure and temperature and the fluids may undergo phase separation. Taking the compressible fluid in single phase regime is another simplification in more recent simulations. By taking this assumption, the effects of boiling and condensation are not taken into account. This simplification can either be made by weighted averaging the fluid properties of two phases (Jupp and Schultz, 2000) or by assuming the seafloor to be deep enough, so that the hydrostatic pressure is above the critical point of water (Fontaine and Wilcock, 2007). This assumption restricts the understanding of phase separation and segregation effects in hydrothermal systems. The phase separation is a result of density difference between vapor and liquid in subcritical boiling regime and can lead to different net forces applied to the fluids. Recent numerical studies used more realistic criteria in a multi-phase fluid regime (e.g. Driesner and Geiger, 2007, Coumou et al., 2009b).

Figure 1-2 shows pure water density as a function of enthalpy and pressure. This figure can be divided into four regions of supercritical fluid, compressed water, compressed steam and two-phase fluid -where both phases coexist. Critical point of pure water is at 22.1 MPa and 374°C. Above the critical point, the fluids are at supercritical condition where a distinction between the phases is not possible. In this region, phase separation does not occur by increasing energy and therefore at a constant pressure, the temperature increases with energy. By increasing the energy at a constant pressure below the critical point of water (e.g. 10 MPa), the temperature of compressed water gradually increases until the fluids reach saturated water curve and enter two-phase region. If further heat continues to be added, the temperature remains constant at the two-phase region and saturation will decrease until the fluids hit the saturated steam

curve. By increasing energy further, only compressed steam exists. The temperature in this region increases with energy.

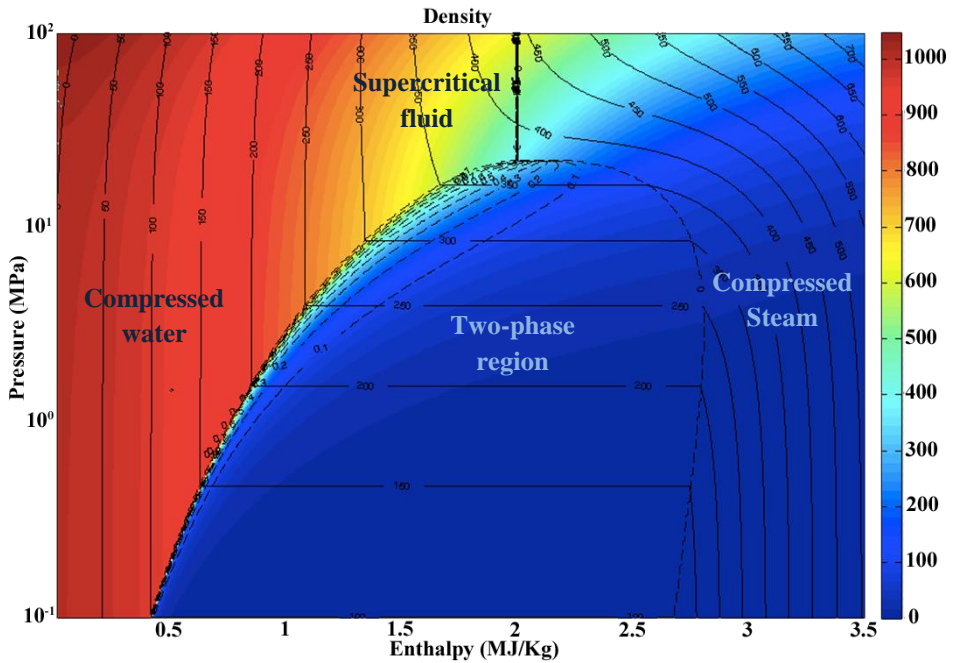


**Figure 1-2:** Phase diagram for pure water. The solid lines are temperature (°C) and dashed lines are saturation. Color contours illustrate fluid density in Kg/m<sup>3</sup>.

Using simulations of hydrothermal systems, several theories have already been investigated. For example, previous studies showed that the geometry of simulation domain affects plume distribution in magmatic hydrothermal systems. Lowell (1991) indicated effects of topography on plume deviation in subaerial and submarine settings. In general, the hydrothermal plumes tend to vent at bathymetric highs in submarine settings and at topographic lows in subaerial settings. The reason can be explained by different pressure fields in submarine and subaerial settings. The hydrothermal plumes initially form below bathymetric lows and highs. To explain the plume deviation mechanism, we consider a water column below bathymetric lows and highs. The density of

## Introduction

---

water decreases with increasing temperature. Therefore, at the same depth below sea level, the pressure below bathymetric highs is lower than below bathymetric lows, as it supports larger volume of lighter water above it. As a result, this mechanism favors venting at bathymetric highs (Figure 1-3a). In the subaerial settings, the fluid pressure at the surface of water table is constant at the atmospheric value and temperature isotherms mimic the water table topography. Consequently, in a water column directly below a topographic (water table) high, pressure is higher than below a topographic (water table) low. Therefore, venting tends to focus at bathymetric lows in subaerial settings (Figure 1-3b). The effect of topography in subaerial settings is relatively well understood (e.g. Hartline and Lister, 1981; Forster and Smith, 1988; Ingebritsen et al., 2006), but a quantitative study of the bathymetric effects on the hydrothermal flow in spreading ridges is not yet investigated. In this thesis, bathymetry-driven fluid flow is quantitatively studied by 2D simulations in submarine settings. Besides, two case studies on Lucky Strike and East Pacific Rise 9°30' vent sites are modeled to understand how bathymetric relief in real geological settings can help focusing venting at the ridge axis.

Beside seafloor bathymetry, faults and fractures and their connections also place important controls on the pathways of hydrothermal plumes. The actual geometry of faults and cracks can be identified by earthquake monitoring in regional scale, but the precise mapping is only possible by reflection seismic studies. The permeability structure remains poorly constrained as it requires *in situ* sampling in wells. Even recent simulations of real nature have not thoroughly considered the geologically complex structures and the proper quantifications are still missing. Some studies are carried out by assumption of homogeneous porous medium for the simulations (e.g. Coumou et al., 2008a; Fontaine and Wilcock, 2007; Driesner, 2010). Some other studies have been carried out on the simplified heterogeneous fractured systems (e.g. Geiger et al., 2004; Emmanuel and Berkowitz, 2007; Fairley, 2009).

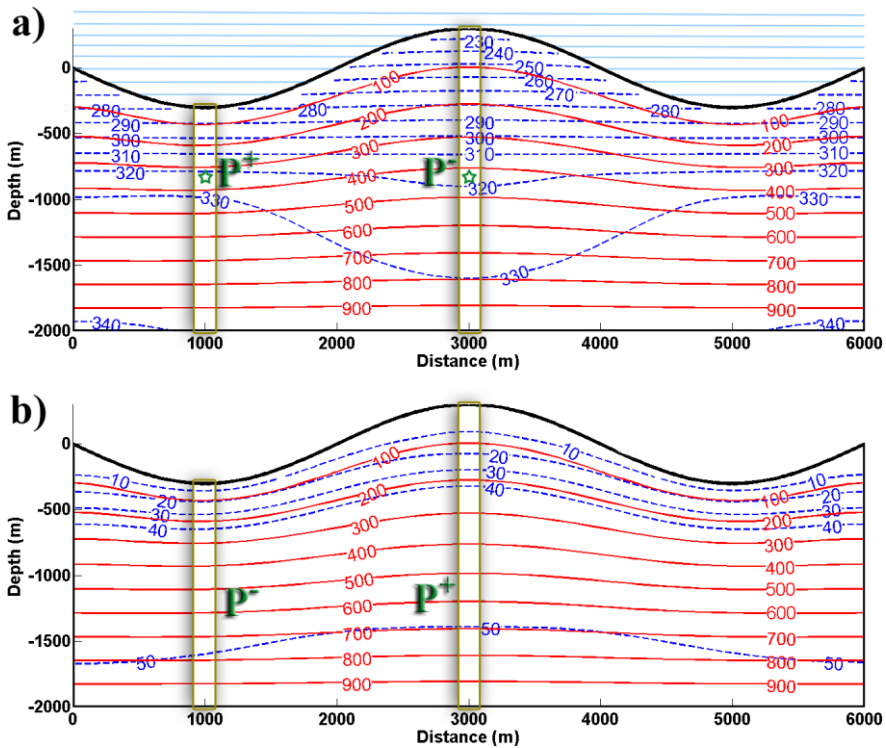


**Figure 1-3:** Pressure and temperature pattern in a) submarine and b) subaerial settings. Solid lines are temperature ( $^{\circ}\text{C}$ ) and dashed lines are pressure (bar).

In heterogeneous settings, fluid motion can be affected according to structural variations and therefore, the fluid pathways and vent sites might be affected. Similar to permanent heat sources at MOR, transient heat sources are also able to trigger a hydrothermal convection. However, the sustainability of such systems is directly linked to their heat budget and matrix permeability. An example for transient heat sources is sill intrusions emplaced during continental break-up in volcanic passive margins. The sill intrusions buried in passive margins and their associated hydrothermal systems are able to mature the source rock provided that the sediments are rich in organic matter. Previous studies on thermal maturation are mainly carried out by assumption of conductive cooling (e.g. Aarnes et al., 2010; Fjeldskaar et al., 2008). However, the convection alters the heat distribution in the porous matrix and therefore, it should be considered

in thermal maturity modeling. This thesis aims at studying the hydrothermal convection pattern triggered by sill intrusions in Norwegian passive margin as well as associated thermal maturity of source rock.

As mentioned above, many previous studies have addressed hydrothermal convection in different settings. Nevertheless it is not clear what the different strengths and limitations of previous models are and what the most promising solution strategies are for submarine hydrothermal systems. This thesis, therefore, evaluates a number of common solutions for the hydrothermal flow equations in simplified settings.

### **1.4. Thesis outline**

In this thesis, a computer code is developed in MATLAB, which resolves for two-dimensional single-phase hydrothermal fluid flow. The code is able to simulate highly heterogeneous media including surface topography. The effects of structural variations on the fluid flow can, therefore, be captured. The thesis focuses on the following subjects:

Chapter 2 discusses the effects of bathymetric relief on the pattern of hydrothermal plumes in submarine settings. This chapter aims at quantifying the bathymetry-driven flow by a series of synthetic simulations. Plume deviation from its original vent location in presence of different surface slopes as well as the depth from heat source is discussed. Two case studies of Lucky-Strike and East Pacific Rise 9°30'N as instances for slow- and fast-spreading ridges are also modeled and the bathymetry-affected flow patterns are discussed. This study is published in the journal of *Geochemistry, Geophysics, Geosystems*.

Chapter 3 discusses fluid flow triggered by sill intrusions in a continental setting. The Norwegian continental margin, where numerous sill complexes have been discovered, is taken as an example. Sills and faults geometries are obtained from interpreting a 3D multichannel seismic data recorded on Gjallar Ridge area. The simulation is performed by a 1D thermal reconstruction of basin prior to sill injection and 2D porous fluid flow calculations. The influence

of fluid flow in maturation of source rock is discussed by comparing to a model where fluid advection is not accounted for. This study is being prepared for submission in the journal of Basin Research.

Chapter 4 describes the numerical modeling techniques and the associated formulations as a short review and compares different methods of modeling by their advantages and disadvantages. Finite element and finite volume methods as components of this study are described in full detail in terms of time and space discretizations and solution in one- and two-dimensional domains. Subsequently, a number of advection and diffusion solution schemes are evaluated by numerical experiments. In this chapter, Semi-Lagrangian and Finite volume advection methods as well as Explicit, Fully implicit, Crank-Nicolson and Exponential diffusion methods are discussed and compared using simplified simulations. The Nusselt number that presents the ratio of convective to conductive heat transfer, is then computed for a series of simulations. These analyses suggest the minimum resolution required for the simulations. Finally, a real hydrothermal convection is simulated using semi-Lagrangian and Finite Volume Method advection schemes.

Chapter 5 concludes the results obtained from the simulations in different setups and settings and possible future fluid flow studies.



## Chapter 2

Controls of bathymetric relief  
on hydrothermal fluid flow at  
mid-ocean ridges



# Controls of bathymetric relief on hydrothermal fluid flow at mid-ocean ridges<sup>1</sup>

*Bani-Hassan, N., Iyer, K., Rupke, L., Borgia, A.*

## *Abstract*

We present quantitative modeling results for the effects of surface relief on hydrothermal convection at ocean-spreading centers investigating how vent site locations and subsurface flow patterns are affected by bathymetry induced sub-seafloor pressure variations. The model is based on a 2D FEM solver for fluid flow in porous media and is used to simulate hydrothermal convection systematically in 375 synthetic studies. The results of these studies show that bathymetric relief has a profound effect on hydrothermal flow: bathymetric highs induce subsurface pressure variations that can deviate upwelling zones and favor venting at structural highs. The deviation angle from vertical upwelling can be expressed by a single linear dependence relating deviation angle to bathymetric slope and depth of the heat source. These findings are confirmed in two case studies for the East Pacific Rise at 9°30'N and Lucky Strike hydrothermal fields. In both cases, it is possible to predict the observed

---

<sup>1</sup> Published in *Geochemistry Geophysics Geosystems*, Vol. 13, Q05002, 17 PP., 2012, doi:10.1029/2012GC004041

vent field locations only if bathymetry is taken into account. Our results thereby show that bathymetric relief should be considered in simulations of submarine hydrothermal systems and plays a key role especially in focusing venting of across axis hydrothermal flow onto the ridge axis of fast spreading ridges.

### **2.1. Introduction**

Hydrothermal systems are ubiquitous geological features in areas where heat flow is high and fluids can readily circulate through a permeable matrix. In fact, hydrothermal flow through the Earth's crust has frequently a first order control on major geological processes active on the seafloor. For example, hydrothermal venting is closely linked to the genesis of oceanic crust. Seawater enters the young ocean floor along fractures and cracks to reach and react with a hot magmatic intrusion forming mineral-rich buoyant hydrothermal brine. Regardless of setting, a challenge to submarine hydrothermal research is that the physicochemical processes that control them occur deep inside the Earth's crust and are largely inaccessible to direct sampling. Nevertheless, much has been learned from fluid geochemistry, petrological and geochemical studies, geophysical imaging, thermodynamics, and numerical simulations (e.g. Vondamm, 1990; Murton et al., 1994; Charlou et al., 1996; Wilcock, 1998; Charlou et al., 2002; Allen and Seyfried, 2003; Cherkaoui et al., 2003; Bach et al., 2004; Iyer et al., 2008; Coumou et al., 2009b; Iyer et al., 2010). The venting of these hydrothermal fluids back into the ocean is of major importance as it is associated with enhanced cooling of the ocean floor, formation of deep-sea ore deposits, and unique ecosystems that exist around vent sites in extreme environmental conditions (Lister, 1980; Tufar et al., 1986; Haymon et al., 1989; Fouquet et al., 1995; Cathles et al., 1997; Boetius, 2005; Kelley et al., 2005; Marques et al., 2007).

Mid-ocean ridges with their intense magmatic and hydrothermal activities are good examples where we can study the effects of bathymetry on submarine hydrothermal flow. At both, fast and slow spreading ridges, formation of new oceanic crust is controlled by a combination of magmatic, tectonic and

hydrothermal processes. Fast spreading ridges, like the East Pacific Rise, are likely to be in steady state and have a stable melt lens beneath the ridge axis (Morgan and Chen, 1993; Baran et al., 2005). Their topography is characterized by an axial high on the order of hundred meters in height whereas the lateral extension may reach several kilometers (Carbotte and Macdonald, 1994) and hydrothermal venting appears to be exclusively located directly on-axis (Baker and German, 2004). Slow-spreading ridges are more complex and undergo shifting periods of magmatic and tectonic phases (Escartin et al., 2008). They are most likely not in steady state and a stable melt lens has so far only been imaged beneath the magmatically active Lucky Strike segment on the Mid-Atlantic Ridge (Singh et al., 2006). The bathymetry of slow-spreading ridges show mostly wide, deep median valleys with highly variable relief in excess of 1000 m that can be up to 10 km in width (e.g. Smith and Cann, 1992; Kleinrock et al., 1997; Coakley and Cochran, 1998; Searle et al., 1998; Tolstoy et al., 2001; Dick et al., 2003). Vent fields have been reported both on-axis (e.g. 5°S (Koschinsky et al., 2008), Lucky Strike (Dusunur et al., 2009)) as well as off-axis (e.g. Logatchev (Schmidt et al., 2007), TAG (deMartin et al., 2007)). Direct observations indicate that magmatic hydrothermal systems at mid-ocean ridges often vent at bathymetric highs. For example, the Lucky Strike vent-field is located on the ridge axis above the Axial Magma Chamber (AMC) on a central volcanic cone. At fast-spreading ridges, the situation is somewhat simpler as most hydrothermal venting occurs on-axis on top of the axial high (Baker and German, 2004). At the East Pacific Rise (9°40'N, 104°17'W), for example, a band of seismicity above the magma chamber illustrates that hydrothermal activity is aligned along the ridge axis (Tolstoy et al., 2008).

At both fast- and slow-spreading ridges, the locations of hydrothermal venting are likely to be controlled by a multitude of parameters including permeability structure, heat source location and crustal accretion mode. Previous studies have addressed submarine hydrothermal flow using numerical models of different complexities. Single phase studies were carried out by numerous researchers (e.g. Wilcock, 1998; Fontaine and Wilcock, 2007;

Coumou et al., 2008a; Coumou et al., 2009a; Theissen-Krah et al., 2011). More sophisticated multi-phase studies on convection patterns were recently performed as well (Coumou et al., 2009b). However, the effect of bathymetric relief was largely neglected in these studies. The impact of topography on subaerial systems is well known (Ingebritsen et al., 2006): groundwater flow is directed from relative highs in the water table to relative lows so that venting is likely to occur in structural lows and recharge occurs in structural highs. The opposite occurs in submarine hydrothermal systems where venting occurs in bathymetric highs. The physics of the focusing effect of bathymetric relief on hydrothermal venting into the highs can be explained by closer inspection of the temperature and pressure fields of submarine hydrothermal systems and has been already described by previous work (Ingebritsen et al., 2006). Pressure at the seafloor is controlled by water depth, while the pressure inside the crust is additionally influenced by the density of the pore fluids. Steady-state conductive geotherms mimic the bathymetric relief and are consequently deflected upwards below bathymetric highs. As fluid densities are strongly temperature dependent, this thermal structure controls the pressure field and results in relative pressure lows below structural highs. As a consequence, a lateral force will be exerted driving convection from the high towards the low pressure area (found beneath the bathymetric high) and any thermal plume will be forced to ascend towards and vent at bathymetric highs.

This effect has, to some extent, been addressed by earlier studies (e.g. Lowell, 1980; Hartline and Lister, 1981; Fisher et al., 1990). Fisher et al (1990) studied the influence of topography on the southern flank of the Costa Rican Rift and found that subcritical convection in the study area results in wide zones of fluid recharge occurring in the troughs accompanied by narrow discharge zones at the ridges. A similar result was also obtained by Fisher et al (1994) who found that basement relief and differential sediment thickness play a greater role than bathymetry in enhancing passive, off-axis convection. More recently, Kawada et al. (2011) studied the influence of seamount aspect ratio and heat flow on fluid flow patterns within and around the seamount. They established that seamounts with high aspect ratio contain multiple convection

cells irrespective of the crustal heat flow. On the other hand, small seamounts can act as a discharge zone when heat flow is low and act as a recharge zone if heat flow is high. However, a systematic study on bathymetry-driven fluid flow is still missing. Here we present a 2D single phase model that is especially tailored to address this topic. In addition to a number of synthetic studies, we use observations from sites across the East Pacific Rise (9°30'N) and the Lucky Strike vent-fields as real-world counterparts in order to understand how bathymetry affects hydrothermal convection patterns.

## 2.2. Hydrothermal convection model

### 2.2.1. Governing equations

We have developed a hydrothermal flow model that is based on Darcy flow and resolves for pure water convection in porous media. The model formulation assumes that only one fluid phase is present at any spatial location and is, therefore, restricted to single phase flow of pure water during which phase separation does not occur. This simplification is justified as most mid-ocean spreading centers are located at water depths in excess of or at least close to the critical end-point of pure water (~220 bar).

Equation (2.1) describes mass conservation in porous media, considering the fluid is compressible and porosity is constant:

$$\phi \frac{\partial \rho_f}{\partial t} = -\nabla \cdot (\rho_f \vec{u}) \quad (2.1)$$

where  $\vec{u}$  is the Darcy fluid velocity,  $\rho_f$  is fluid density,  $t$  is time and  $\phi$  corresponds to matrix porosity (See Table 1 for complete list of variables and values). The velocity is defined by Darcy's Law:

$$\vec{u} = -\frac{k}{\mu_f} (\nabla P - \rho_f \vec{g}) \quad (2.2)$$

Here  $k$  is the rock permeability,  $\mu_f$  is the dynamic viscosity of the fluid,  $P$  is the fluid pressure and  $\vec{g}$  is the gravitational acceleration. Substituting eqn. (2.2) into eqn. (2.1) and by splitting density changes into their pressure and temperature parts, we obtain:

$$\phi \rho_f \beta_f \frac{\partial P}{\partial t} = \nabla \cdot \left[ \frac{k \rho_f}{\mu_f} (\nabla p - \rho_f \vec{g}) \right] + \phi \rho_f \alpha_f \frac{\partial T}{\partial t} \quad (2.3)$$

where  $\alpha_f$  is fluid thermal expansion coefficient and  $\beta_f$  is fluid isothermal compressibility.

The energy equation is described by:

$$\left( \phi \rho_f c_{pf} + (1-\phi) \rho_m c_{pm} \right) \frac{\partial T}{\partial t} = -\rho_f c_{pf} \vec{u} \cdot \nabla T + \nabla \cdot (\lambda \nabla T) \quad (2.4)$$

where  $\lambda$  corresponds to effective thermal conductivity,  $T$  to temperature and  $c_p$  to specific heat capacity, which accounts for advective and conductive heat transport in addition to heat storage both in the fluid and the rock matrix. Subscript  $m$  and  $f$  denote matrix and fluid properties, respectively. Pressure-volume work and viscous dissipation are neglected in the energy equation (Garg and Pritchett, 1977). Fluid properties of density, viscosity and specific heat capacity are treated as functions of pressure and temperature and are computed at every time-step using the PROST library (Bauer, 1998 for the IAPWS-84 equation of state).

Table 1: List of model parameters

Parameter	Symbol	Value (Synthetics)	Value (Case studies)	Unit
Density of fluid	$\rho_f$	Based on PROST	Based on PROST	$kg\ m^{-3}$
Dynamic viscosity of fluid	$\mu_f$	Based on PROST	Based on PROST	$Pa\ s$
Specific heat capacity of fluid	$c_{pf}$	Based on PROST	Based on PROST	$J\ kg^{-1}\ K$
Pressure	$P$	Calculated	Calculated	$Pa$
Temperature	$T$	Calculated	Calculated	$^{\circ}C$
Darcy Velocity	$\vec{u}$	Calculated	Calculated	$m\ s^{-1}$
Density of Matrix	$\rho_m$	2700	2750	$kg\ m^{-3}$
Specific heat capacity of Matrix	$c_{pm}$	880	880	$J\ kg^{-1}\ K$
Porosity of Matrix (Synthetics)	$\phi$	0.1	0.01	
Permeability of Matrix	$k$	$5 \times 10^{-15}$	Variable	$m^2$
Thermal conductivity	$\lambda$	2	2.25	$W\ m^{-1}\ K^{-1}$
Thermal expansion coefficient	$\alpha$	Calculated	Calculated	
Compressibility factor	$\beta$	Calculated	Calculated	
Gravitational acceleration	$g$	9.81	9.81	$m\ s^{-2}$
time	$t$			$s$

### 2.2.2. Numerical implementation

The governing equations are solved using a 2D finite element approach in combination with an advection scheme. The solution is computed for every time step in sequential order: (1) thermal diffusion is resolved, (2) temperature is advected using the Darcy velocities, (3) fluid properties are evaluated, (4) new fluid pressure and porous flow velocities are then computed.

The fluid pressure equation (eqn. 3) is solved using finite elements. The weak form of this equation, derived by the Galerkin method, is:

$$\begin{aligned}
 & \int_{\Omega} N' \bar{\phi} \bar{\beta}_f \bar{\rho}_f NP^n d\Omega + \int_{\Omega} \frac{\partial N'}{\partial x} \frac{\bar{k} \bar{\rho}_f}{\bar{\mu}_f} \Delta t \frac{\partial NP^n}{\partial x} d\Omega \\
 & + \int_{\Omega} \frac{\partial N'}{\partial y} \frac{\bar{k} \bar{\rho}_f}{\bar{\mu}_f} \Delta t \frac{\partial NP^n}{\partial y} d\Omega = \\
 & - \int_{\Omega} \frac{\partial N'}{\partial y} \frac{\bar{k}}{\bar{\mu}_f} \Delta t g N \bar{\rho}_f^2 d\Omega + \int_{\Omega} N' \bar{\alpha}_f \bar{\phi} \Delta t \bar{\rho}_f N \left( \frac{\Delta T}{\Delta t} \right) d\Omega \quad (2.5) \\
 & + \int_{\Omega} N' \bar{\phi} \bar{\beta}_f \bar{\rho}_f NP^o d\Omega + \oint_{\Gamma} N' \frac{\bar{k} \bar{\rho}_f}{\bar{\mu}_f} \Delta t \frac{\partial NP^n}{\partial x} d\Gamma \\
 & + \oint_{\Gamma} N' \frac{\bar{k} \bar{\rho}_f}{\bar{\mu}_f} \Delta t \frac{\partial NP^n}{\partial y} d\Gamma + \oint_{\Gamma} N' \frac{\bar{k}}{\bar{\mu}_f} \Delta t g N \bar{\rho}_f^2 d\Gamma
 \end{aligned}$$

where  $N$  is linear shape function for three-node triangle elements. Bars and primes denote averaged properties on an element and transposes, respectively. Superscripts  $n$  and  $o$  denote new and old time steps, respectively. Symbols  $\Omega$  and  $\Gamma$  are computational domain and its boundaries, respectively. All fluid and rock properties are averaged over an element and all mass matrices are lumped. The pressure solution is obtained by implementing eqn. (2.5) into a modified version of the Matlab-based FEM solver MILAMIN by Dabrowski et al. (2008). Taking derivatives of the pressure solution provides the updated Darcy velocities at element centers. These velocities are subsequently averaged onto nodes in order to use them with a node-based semi-Lagrangian advection scheme. Note that the fluid and matrix properties are calculated on the nodes and Darcy velocities are mapped on nodes by taking equal contributions of neighboring elements. This mapping could be avoided by the use of node-centered finite-volume techniques that use velocities at element centers (Geiger et al., 2004). We have experimented with both advection schemes and find that for single-phase calculations, the semi-Lagrangian approach does not have

problems with mass conservation and allows for larger computational time-steps. We have, therefore, used a semi-Lagrangian solver for the advective part of the energy eqn. (2.4) that uses the element shape functions for temperature interpolation. The diffusive part of eqn. (2.4) is again solved with the FEM scheme. This model was validated against the results of Coumou et al. (2006) and a previous version of the model was also benchmarked against Cherkaoui and Wilcock (1999) (Iyer et al., 2010).

### **2.3. Synthetic studies**

This section aims at constraining the effects of bathymetric relief on hydrothermal convection. Two sets of simulations are carried out. The first set explores the effect of a single bathymetric high on a single plume and the second set of simulations takes into account the effect of multiple bathymetric highs on multiple plume formation. Simulations with a flat seafloor are used as reference cases for both sets which are then used to discuss the effects of bathymetry. The synthetic studies with bathymetric relief are referred to as non-references cases. All simulations are run until a quasi-steady-state is approached; i.e. the single high and multiple high simulations are run for 10,000 and 3000 years, respectively. The fluid and matrix parameters used in the simulations with bathymetric relief are the same as those used in the corresponding reference case simulation. The matrix is homogeneous and its properties are kept constant throughout the run for all synthetic simulations. The values for matrix properties are listed in Table (1). The number of elements used in the simulations is approximately 8,300 elements per square kilometer.

#### **2.3.1. Single bathymetric high**

##### **2.3.1.1. Model geometry and setup**

The domain in the single bathymetric high simulations is 4600 m wide while the depth is varied between 1000 and 2000 m. The bathymetric high is

triangular in shape and rises above the flat surface of the domain. The starting point of the bathymetric high is fixed at distance of 1450 m. The flat surface of the 2D domain is kept at a constant pressure of 30 MPa simulating a seafloor depth of ~3 km to ensure that phase separation does not occur in experiments with the highest elevation of the peak. The surface rising above the flat part is kept at a pressure corresponding to its depth. Temperature in the model is initialized to 10°C and the model is heated at the bottom boundary by a Gaussian heat source located at distance of 1500 m. The maximum temperature of the heat source is 1000°C and the width of Gaussian function is 1/12 of the box size in the x-direction. The defined width of the Gaussian heat source ensures that only a single plume is formed in the simulations. The side-boundaries of the box are insulating and the sides and bottom boundaries of the box are impermeable. An upper boundary condition is applied to allow the fluid to vent freely where the plume reaches the surface and allow water at 10°C to enter the domain in recharge zones. This condition is applied by calculating the direction of fluid vectors at the upper boundary nodes.

### 2.3.1.2. **Reference simulation**

A single hydrothermal plume forms at the bottom heat source and ascends vertically to reach the surface right above the center of the heat source. Plume-splitting is observed initially at the bottom of model, but the single plume is rapidly established. The plume vents at the surface after 750 years of convection when the model depth is 1500 m and reaches steady-state.

### 2.3.1.3. **Non-reference simulations**

The non-reference simulations are used to study the maximum deviation of the plume from its original vent location as observed in the reference simulation in the presence of a single bathymetric high. The dimensions of the high are defined by its wavelength (half-width of the high) as well as its amplitude (elevation of the summit with respect to the flat seafloor) which in turn controls how much the plume could deviate from its original vent location. The

wavelength and amplitude of the high is systematically varied from 500 to 1500 m in 250 m increments and 100 to 500 m in 50 m increments, respectively. A single plume is initially formed and vents at the seafloor, right above the center of heat source as observed in the reference simulation. The plume migrates towards the summit of the bathymetric high with time and finally reaches a steady-state. The time after which plume migration begins and the time required for migration to complete before a steady-state is reached depends on the wavelength and amplitude of the prescribed bathymetric high.

The results show that plume deviation and migration time of the plume is inversely dependent on the wavelength and directly dependent on the amplitude (Figure 2-1). An increase in wavelength results in an increase in the distance of the summit from the original plume location, thereby decreasing the control of bathymetry on convection whereas an increase in amplitude directly amplifies this effect. The plume can deviate towards the summit completely for relatively low wavelengths and high amplitudes. Conversely, if the wavelength and amplitude are relatively high and low, respectively, migration of the plume stops at some distance away from the summit. We find that the lateral deviation of the plume divided by its vertical extent, a value easily converted to the plume deviation angle relative to the vertical ( $\theta$ ), can be expressed as a linear function of bathymetric slope (amplitude/wavelength) (Figure 2-2a). In the following we will refer to this value as relative plume deviation ( $D$ =lateral plume deviation/vertical plume extent). The results show a further dependence on the depth of the heat source (Figure 2-2a), which is systematically varied between 1000 and 2000 m in 250 m increments. The deeper the heat source, the less pronounced is the impact of bathymetry on plume deviation. This can be explained by the diminishing relative pressure difference caused by the bathymetric high as depth is increased.

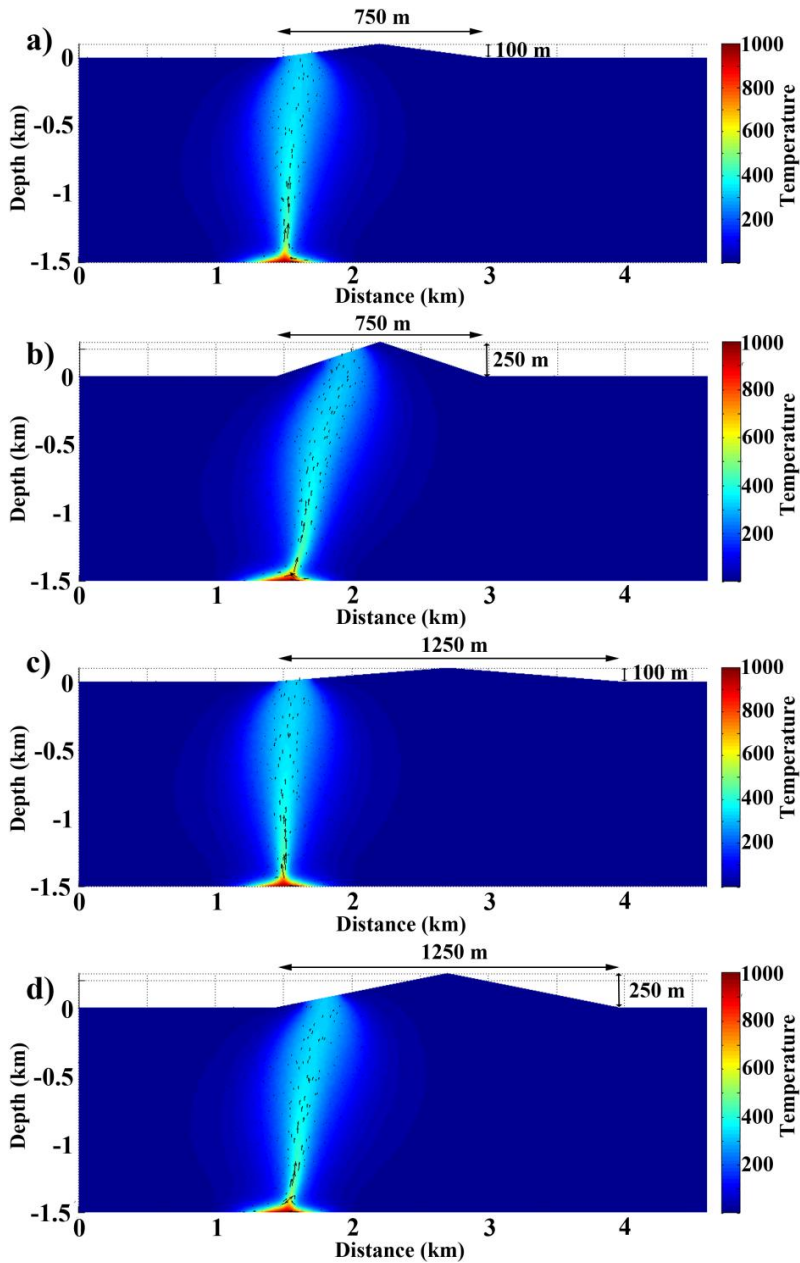


**Figure 2-1:** Simulations with a single plume and a single bathymetric high at steady-state. Four examples are presented with the bathymetric high dimensions of a) amplitude 100 m and wavelength 750 m, b) amplitude 250 m and wavelength 750 m, c) amplitude 100 m and wavelength 1250 m and d) amplitude 250 m and wavelength 1250 m. The results show that the maximum deviation of the single plume from its origin is proportional to the amplitude and wavelength of the bathymetric high.

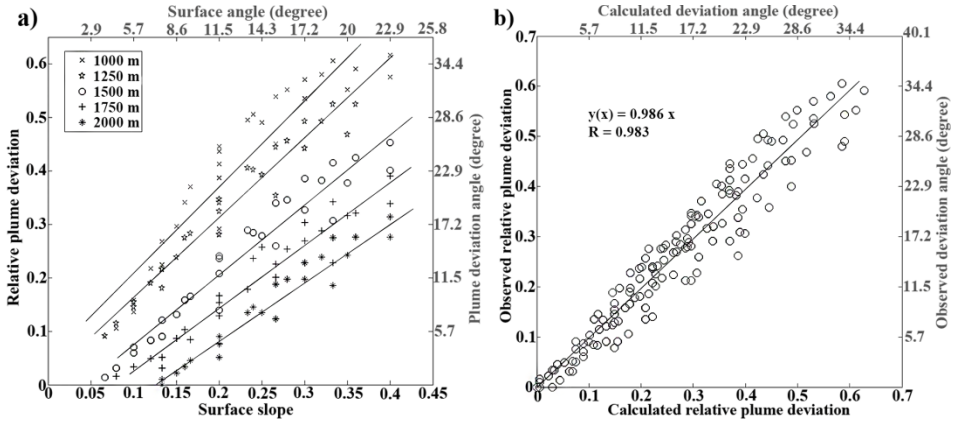


**Figure 2-2:** a) Relative plume deviation (lateral plume deviation/vertical plume extent) as a function of surface slope for different model depths. The results suggest a linear relationship between plume deviation and surface slope. Model depth also influences this relationship while retaining the linear fit. b) The observed relative plume deviation for a single plume for different amplitudes, wavelengths and model depths against the relative plume deviation derived from eqn. (2.6).

We find that the heat source depth has a linear influence on the coefficients of the dependence between relative plume deviation and bathymetric slope so that a single general relationship between relative plume deviation, bathymetric slope and depth of heat source can be formulated:

$$D\left(\frac{A}{W}, z\right) = f(z)\frac{A}{W} + h(z)$$

$$f(z) = -5.65 \times 10^{-4} z + 2.178 \quad (2.6)$$

$$h(z) = -1.82 \times 10^{-4} z + 0.229$$

$$\theta = \tan^{-1}(D)$$

Where  $A$  is the amplitude (m),  $W$  is the wavelength (m), and  $z$  is depth of the heat source (m). Figure 2-2b shows good agreement between the simulation

results and the functional dependence described in eqn. (2.6). A linear least-squares fit yields a slope of 0.986 and a regression coefficient of 0.983 showing that eqn. (2.6) can be used to approximate the effect of a single bathymetric feature on subsurface fluid flow if the location of the heat source is known.

### **2.3.2. Multiple bathymetric highs**

#### **2.3.2.1. Model geometry and setup**

The domain in the 2D synthetic simulations with multiple bathymetric highs is 3.6 km wide and 1 km deep. The bathymetric relief, in the non-reference cases, is represented by a sinusoidal wave with varying amplitudes and wavelengths.

The turning point of the sinusoidal surface in the simulated domain is overlain by 2.5 km of seawater and the temperature in the domain is initialized to 10°C. The domain is continuously heated at the bottom at a temperature of 1000 °C mimicking the effect of a stable magmatic heat source. Similar to the single bathymetric high simulations, the side-boundaries of the box are insulating and the sides and bottom boundaries of the box are impermeable. The temperature upper boundary condition is also the same as that applied to the single bathymetric high simulations. The non-reference simulations are carried out for surface wavelengths of 3600, 1800, 900, 720, 600, 514, 450, 400, 360 and 300 m corresponding to between 2 and 11 bathymetric highs, respectively, while the amplitude varies between 20 m and 300 m, by 20 m increments for all the wavelengths.

#### **2.3.2.2. Reference simulation**

In the reference simulation, several plumes are initially formed at the base of the box where the temperature gradient and subsequently, the density and viscosity gradients in the fluid are highest. These plumes coalesce during their ascent to the surface to form fewer stable upwelling zones (Figure 2-3) and sometimes exhibit plume-splitting phenomena similar to that seen by Coumou

et al. (2006). For the given model setup, the simulation evolves towards a quasi steady-state after  $\sim 1250$  years of convection where eight plumes reach the surface at a fixed distance from each other. A number of smaller plumes are formed at the base of the domain but they are quickly assimilated in the larger, established plumes (Figure 2-3). The average distance between the plumes is  $\sim 514$  m. The aspect ratio of a convection cell is defined as  $A=D/2H$ , where  $D$  is the distance between two adjacent plumes and  $H$  is the depth of the domain. The aspect ratio for the convection cells in the reference simulation is therefore 0.25, which is consistent with the results of simulations performed by Coumou et al. (2006).

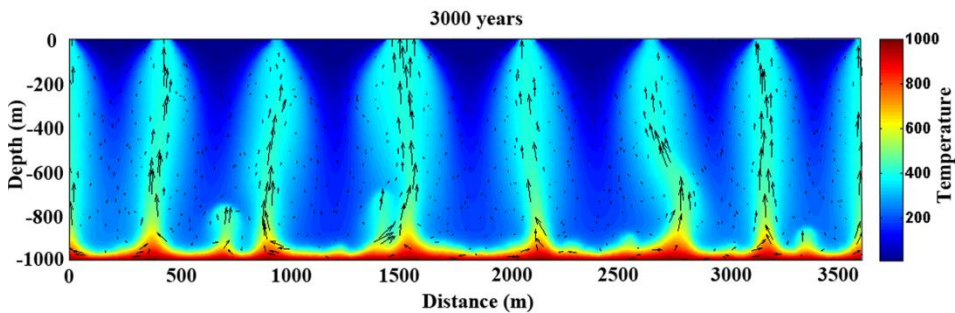


**Figure 2-3:** Temperature plot of the reference simulation with multiple plumes and constant temperature bottom heat source. The system approaches a quasi steady-state at the end of simulation with eight plumes. The aspect ratio for the convection cells is 0.25 and the average distance between plumes is 514 m.

### 2.3.2.3. Non-reference simulations

In these numerical experiments, the bathymetry is represented by a sinusoidal wave with varying amplitude and wavelength. A surface with periodic bathymetry and a constant temperature bottom boundary is selected in order to study the effect of multiple highs on multiple plumes while accounting for the interaction between different plumes.

## Controls of bathymetric relief on fluid flow

---

Figure 2-4 shows the results for selected example runs after 3000 years model run time. All left panel plots show the temperature field and all right panel plots show corresponding histograms of fluid venting as functions of bathymetric relief. Note that the depth of the surface is normalized to the amplitude of the bathymetric relief with the turning point of the surface slope taken as the zero value. A first order observation is that venting generally tends towards bathymetric highs in the presented simulations. Both wavelength and amplitude control how effectively venting is focused into bathymetric highs. Simulations in Figure 2-4a-c illustrate the effects of relief wavelength for a fixed amplitude of 40 m. The tendency of venting at bathymetric highs increases as the wavelength decreases. Figure 2-4c and i show that venting occurs exclusively in the bathymetric highs when the number of bathymetric highs is comparable to or less than the number of plumes in the reference simulation. If the wavelength is increased, venting is more widely distributed over the surface (Figure 2-4 a and g).

The amplitude of bathymetric relief also has a strong effect: as amplitude increases, venting is progressively more focused into bathymetric highs. The bottom three simulations in Figure 2-4 demonstrate the effect of amplitude for a fixed wavelength of 1800 m. The results show that at low amplitude venting may occur at the flanks or even bathymetric lows (Figure 2-4d and j), but the plumes increasingly migrate toward bathymetric highs when the amplitude is increased (Figure 2-4 e, f, k and l).

In general, stronger deviations from vertical plume ascent towards bathymetric highs are found with increasing amplitude. Plumes may vent at flanks and lows during the initial stages of the simulations but are shifted towards the highs as the plumes evolve in time.

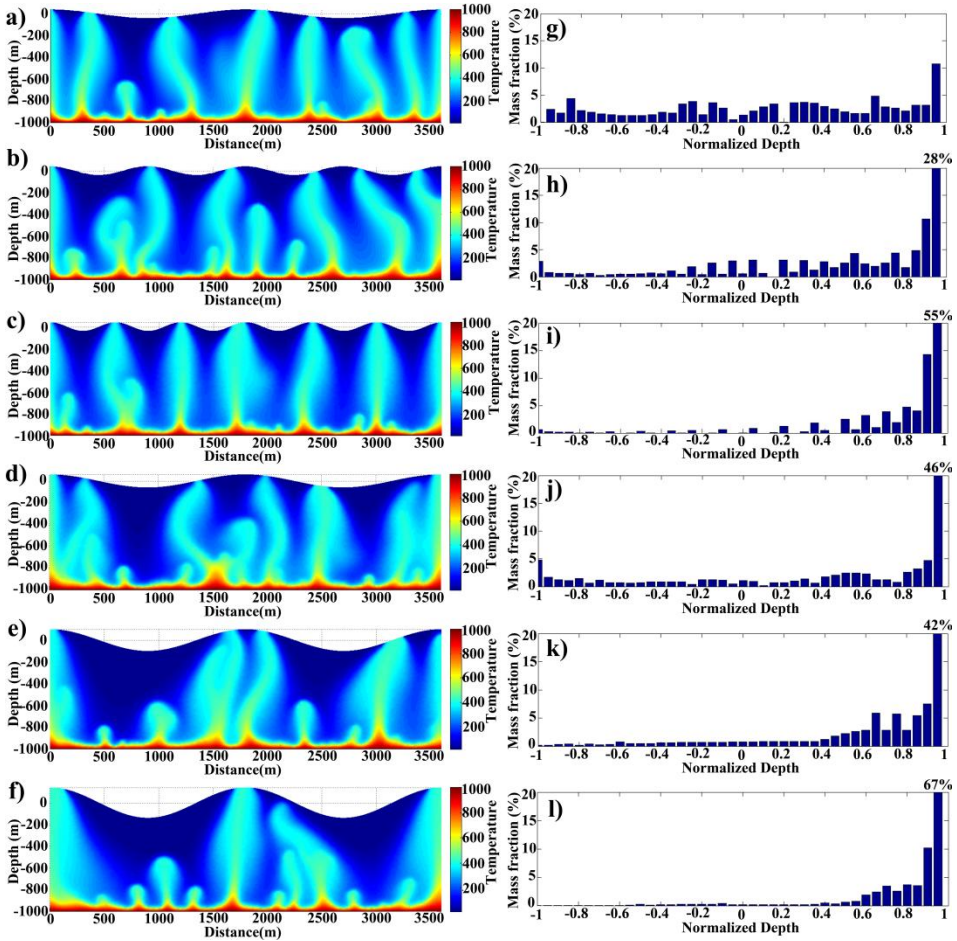


**Figure 2-4:** Simulation results showing the temperature fields for a selected number of variable bathymetric models. Figs. a-c show the late stages of the models where the amplitude of the bathymetric relief is kept at 40 m with the wavelengths of 1800, 900 and 600 m, respectively. Figs. d-f illustrate the simulations where wavelength is kept constant at 1800 m with amplitudes of 60, 100 and 140 m. Figs. g-l show histograms of mass fraction of vent fluids versus surface bathymetry normalized to itself with the depth of the turning point as zero value.

The preceding section showed that both amplitude and wavelength control vent field location. To further explore the focusing of venting at bathymetric highs, the time-integrated mass fraction of vent fluids exiting within the upper half of bathymetric highs is plotted as a function of wavelength and amplitude

in Figure 2-5a. The intersections of the gridlines are the locations of data points. The mass flux is integrated over time starting after 1000 years of convection when all the plumes have reached the surface until 3000 years of convection when the simulation is in a quasi steady-state. The plot summarizes the characteristics of the relationships between amplitude and wavelength discussed above. If the wavelength is slightly larger or smaller than the plume spacing in the reference case (~514m), a bathymetric relief of only ~40m amplitude is sufficient to focus venting into bathymetric highs. If the wavelength is now increased, venting also occurs at flanks or even lows. This de-focusing effect of increasing wavelength can be compensated by increasing amplitude. There is, however, a limit to this: if amplitudes become very large for small wavelengths, venting again tends to occur at flanks as well which occurs when the size of the ascending plume head is larger than the width of the bathymetric high. This behavior suggests that the focusing effects of amplitude and wavelength can be summarized by a single parameter. Figure 2-5b shows that all values plotted in Figure 2-5a do collapse onto a bell-shaped curve if plotted against slope at the turning point of the sinusoidal relief. The curve shows maxima approximately between  $30^\circ$  and  $60^\circ$  where all the surface slopes steeper or gentler will result in lower focusing of plumes at the bathymetric highs. Therefore, the curve can be split into three regions: low-angle ( $<30^\circ$ , zone 1), medium-angle ( $30^\circ$ - $60^\circ$ , zone 2) and high-angle ( $>60^\circ$ , zone 3) surfaces. As observed, maximum venting is achieved through the bathymetric highs where the surface angle lies in zone 2. This suggests that the probability of finding vent-sites at bathymetric highs is roughly proportional to seafloor slope. The simulations were also conducted using deeper and shallower domains. The results for these simulations do not significantly differ from those presented above and the maximum volume of venting at the highs still occurs at slopes between  $\sim 30^\circ$  and  $\sim 60^\circ$  similar to the previous simulations. The results obtained from section 2.3.1 combined with eqn. (2.6) allows for a qualitative assessment of the relation between the surface slope and amount of venting shown in Figure 2-5.

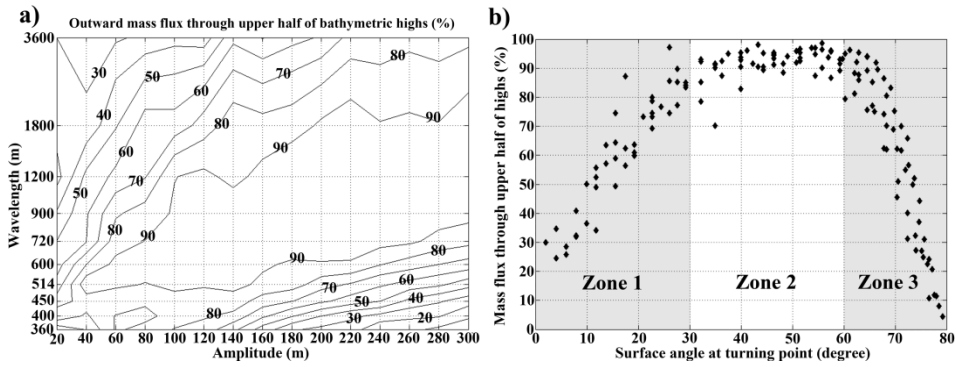


**Figure 2-5:** a) Outward mass flux of vent fluid through the upper half of bathymetric highs (counted from the turning point) relative to total outward mass flux in a semi-logarithmic scale as a function of amplitude and wavelength of the sinusoidal surface relief. The gridline intersections are the location of the simulation results. b) Outward mass flux of vent fluid through the upper half of bathymetric highs (counted from the turning point) relative to total outward mass flux for all 150 multiple-plume synthetic simulations as a function of the surface slope at the turning points. The plot can be differentiated into three zones: zone 1 (surface angle  $< 30^\circ$ ) where venting is not focused at bathymetric highs as the maximum deviation angle allowed for the plumes to reach a high calculated from the single bathymetric high simulation is less than the required deviation angle; zone 2 ( $30^\circ < \text{surface angle} < 60^\circ$ ) where venting is focused at the bathymetric highs as the calculated maximum deviation angle for the generated plumes is larger than the required deviation angle and zone 3 (surface angle  $> 60^\circ$ ) where venting is observed at flanks and lows in addition to bathymetric highs as the plume head is larger than the width of bathymetric highs.

A rigorous quantitative analysis is not possible due to the influence of plume interactions and due to the difference in slope variation used in the single and sinusoidal bathymetry simulations. Nevertheless, simulations with a surface slope of less than  $\sim 30^\circ$  show less than optimal venting as the angle of deviation required for a plume farthest away from a bathymetric high to be present at that high is larger than the maximum angle of deviation calculated by eqn. (2.6) for the given parameters. Conversely, in simulations where the surface slope angle is greater than  $\sim 30^\circ$ , the angle of deviation required for any plume to reach the closest high is less than the calculated maximum angle of deviation suggesting that complete migration to a high is possible. Simulations with a surface slope

greater than  $\sim 60^\circ$  show reduced venting at highs as the width of the plume head exceeds the width of bathymetric relief.

As a cautious note it should be added that these results are somewhat dependent on initial conditions. The presented simulations all assume an initially cold domain so that the initial pressure regime is not influenced by bathymetry. Only when a plume reaches a bathymetric feature, the pressure field is affected by bathymetric relief. Conversely, if an initial geothermal gradient is assumed, the initial pressure field is already affected by bathymetric relief. However, since we have largely restricted ourselves to the analysis of steady-states, which are only weakly dependent on initial conditions, our results keep their generality.

## **2.4. Case studies**

The preceding section has shown that bathymetric relief can have strong controls on vent site location. We will now use these insights to analyze how venting at the fast spreading EPR at  $9^\circ\text{N}$  and the slow-spreading Lucky Strike segment are influenced by bathymetric relief.

### **2.4.1. East Pacific Rise vent field ( $9^\circ 30'\text{N}$ )**

#### **2.4.1.1. Geological setting**

The EPR is characterized as a fast spreading ridge with an average full spreading rate of 110-150 mm/yr (Foulger, 2010). The bathymetry at  $9^\circ\text{N}$  at EPR shows relatively smooth relief with an axial high corresponding to the ridge axis (e.g. Toomey et al., 1994; Tolstoy et al., 2008). A nearly continuous shallow melt lens was imaged at a depth of  $\sim 1.5$  km below the seafloor (Detrick et al., 1987). The melt lens is extremely narrow with a thickness of 10-50 m and width of  $\sim 1$  km (Kent et al., 1993). Seismic tomography suggests that a “slot” of hot partially molten crust exists below the ridge axis with a width of about  $\sim 6$  km (Dunn et al., 2000); the width of this hot zone widens in the mantle region to nearly 15km. Fisher (2003) has argued that this special shape of hot crust can be

explained by off-axis hydrothermal cooling, which is consistent with the ideas on pervasive hydrothermal circulation developed at the Oman ophiolite (Nicolas et al., 2003). However, if this pervasive off-axis (and across axis) hydrothermal flow does exist, it apparently does not result in off-axis venting; nevertheless, further off-axis surveys are essential to confirm this. All currently known vent sites are located directly on axis (Haymon et al., 1991) including the sites at 2570m water depth at 9°30'N (<http://www.interridge.org/irvents/content/epr-9-30n>). Here we test if hydrothermal fluids rising along off-axis margins of the hot central temperature anomaly are likely to be focused onto the ridge axis by bathymetric relief.

### 2.4.1.2. Model setup

The East Pacific Rise (9°30'N) vent site was modeled based on a depth converted map derived from studies by Dunn et al. (2000) and a topographic sketch by Carbotte and Macdonald (1994). We modeled two scenarios: one with a flat top and one with the actual bathymetric relief. The temperature is set to 10 °C in the matrix and the pressure is set to hydrostatic values initially. A hot slot (1000°C) is assumed to start from 1.6 km below the seafloor and extends up to depth of 8 km (bottom of model). The width of this high temperature increases rapidly to up to ~20 km at the bottom of modeling domain. Relatively smooth bathymetric variations of up to 400 m occur within the modeling domain. The maximum elevation of the seafloor is located just above the melt lens. The sides of model are insulated and the sides as well as the bottom of the model are impermeable. The surface pressure varies with topography where the highest point of the domain lies at a depth of 2.57 km below sea level. The matrix permeability structure at the East Pacific Rise and at fast spreading ridges in general is not well known and few studies give quantitative estimates. Theissen-Krah et al. (2011) provided estimates for the permeability structure above the melt lens and suggest that this permeability must decrease off-axis - potentially as a consequence of alteration and mineral precipitation reactions. We largely follow the permeability model of Theissen-Krah et al. (2011) and

extend it by higher permeability values in the deeper near- to off-axis crust to allow for deep hydrothermal flow as discussed above. We achieve this by employing a permeability model, in which the surface permeability decreases exponentially with depth to the anomalously hot zone. For numerical convenience this is done by using a steady state diffusion temperature field and defining matrix permeability as a function of this initial temperature field. The computed permeability is kept fixed though and does not evolve by temperature variations during simulations. The surface permeability at the ridge axis is assumed to be  $\sim 6 \times 10^{-15} \text{ m}^2$ , which is consistent with the estimates of *Theissen-Krah et al.* (2011). The resulting permeability field is scaled by a lateral exponential decrease in permeability from 2000 m away from the ridge axis. This results in the following permeability model:

$$k = 6 \times 10^{-15} \times \exp(-3.2 \times 10^{-3} T) \quad (2.7)$$

$$k^* = k \times \exp(-7 \times 10^{-4} x) \quad (2.8)$$

where  $x$  is the absolute distance from 2000 m away from the ridge axis (m),  $k^*$  is the revised permeability which is used as a substitute for  $k$  in Eqs. (2.2), (2.3) and (2.5), and  $T$  the initial steady state conductive temperature ( $^{\circ}\text{C}$ ).

This permeability model is plotted in Figure 2-6 and is consistent with the observed melt lens depth and allows for pervasive off-axis hydrothermal flow. However, our static model setup is not suited for making estimates on permeability so that it remains our best guess on the actual permeability structure at EPR. Hopefully more data in combination with dynamical models will help to further constrain the deep permeability at ridges in the future.

The matrix properties are listed in Table 1. The number of elements used in these simulations is 1000 per square kilometer. A further assumption is that porosity is constant and that both permeability and porosity do not change during the simulations.

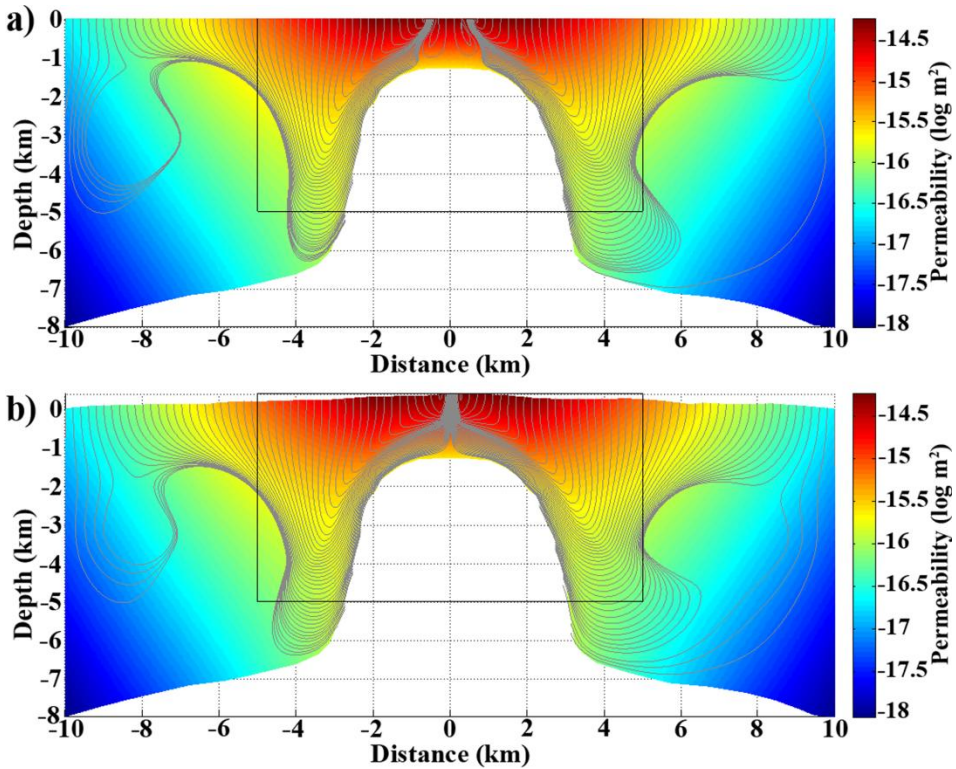


**Figure 2-6:** Permeability structures used in the simulations of East Pacific Rise 9°30'N. The permeability decreases both with depth and the distance from the ridge axis. The black boxes in the figures are the domains plotted in fig. 4-7. Panel a) shows the permeability structure and late stage flow lines for the flat top simulation and b) for the simulation with bathymetric relief. Note how the flow lines visualize pervasive off-axis hydrothermal flow.

### 2.4.1.3. Results

The modeled temporal evolution of hydrothermal convection beneath the East Pacific Rise is shown in Figure 2-7 (the figure dimensions are restricted to 5×5 km to enhance the visibility of venting region). The simulations were run for 50,000 years when a quasi-steady state is attained. The left panel plots show the result with a flat seafloor, while the right panel plots the ones with the actual bathymetric relief. In the early phases of the simulations (Figure 2-7a and c), multiple plumes form above the central slot of hot crust. The plumes later merge

## Controls of bathymetric relief on fluid flow

and form a few major upwelling zones at the top of magma lens. In both settings, small convection cells develop directly on the top of hot crust, while deep large convection cells develop off-axis with upwellings along the margins of the magma chamber and recharge zones extending several kilometers off-axis (Figure 2-6). A striking feature of the simulation with a flat seafloor is that venting does not occur on-axis but at two, near-axis locations (Figure 2-6a). This is due to the fact that upwelling hydrothermal fluids along the margins of the magma chamber are not efficiently focused onto the axis and that several convection cells develop directly above the hot crust (Figure 2-7). This simulation is therefore inconsistent with the existing observations that all venting occurs directly on-axis. In contrast, the simulation with bathymetric relief predicts exclusive on-axis venting (Figure 2-7b and d).

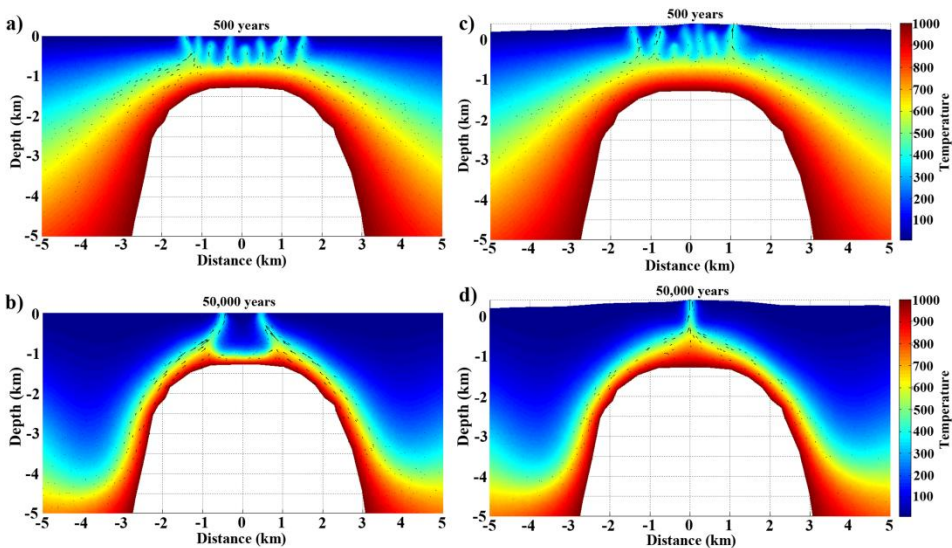


**Figure 2-7:** Simulation results (2D temperature profiles) for the hydrothermal vent field at East Pacific Rise 9°30'N. A hot crust slot is buried 1600 m below the seafloor. Figs. (a) and (c) show the early stages of simulations with and without bathymetric relief, respectively. Figs. (b) and (d) show the late stage of the simulations. Venting exclusively focuses onto the ridge axis only if bathymetric effects on hydrothermal flow are accounted for. The figures are restricted to dimensions of 5×5 km to focus on the vent-site.

The plumes forming above the hot crust and the upwelling along the magma chamber coalesce to form fewer plumes which lean towards the axial high ultimately forming a central plume that vents directly on-axis. This clearly shows the effect of bathymetry to form and focus the central plume at the axial high, even though the bathymetric relief is quite smooth. Off-axis venting is suppressed due to the assumption that permeability decreases with increasing distance to the ridge axis, which is consistent with the current observations at EPR. However, it should be noted that detailed off-axis surveys have not been conducted at EPR and may, in future, provide new constraints on vent-locations farther away from the ridge axis. This would require a reassessment of the overall flow pattern but will not change the outcome of this study showing the influence of bathymetry on on-axis vent-locations.

### **2.4.2. Lucky Strike vent field**

#### **2.4.2.1. Geological setting**

Lucky strike is one of the largest hydrothermal fields located on the slow spreading Mid-Atlantic Ridge (MAR) with 21 active chimney sites at approximately 1740 m depth [<http://www.interridge.org/irvents/content/lucky-strike>]. The full spreading rate at Lucky-Strike vent field is ~21 mm/yr Dziak et al., 2004. The field is located at 37°17' 29" N, 32°16'4" W, 400 km southwest of the Azores islands and is part of a group of four main hydrothermal vent fields (Menez Gwenn, Lucky Strike, Saldanha and Rainbow). The presence of a bathymetric high and a hydrothermal field surrounding a central lava lake led to the suggestion of a shallow axial magma chamber (Fouquet et al., 1995). Furthermore, recent data from reflection seismic, which surveyed the Lucky Strike confirmed this hypothesis (Singh et al., 2006). An AMC was discovered around 3 km beneath the Lucky Strike volcano which spreads about 7 km along the strike of the ridge with a width of 3-4 km (Singh et al., 2006).

### 2.4.2.2. Model setup

In order to simulate hydrothermal convection at the Lucky Strike vent field, a depth-converted seismic section across the ridge axis was digitized and meshed (Dusunur et al., 2009). The length of the seismic line is ~16 km and the magma chamber is buried ~3 km below the seafloor. The depth of the modeled domain is 6 km and the depth of the seafloor is 1740 m below sea level. Similar to EPR, the initial temperature and pressure are set to 10 °C and hydrostatic values, respectively. The 1000°C AMC with a maximum width of 8400 m at the bottom of model is responsible for driving hydrothermal convection. The permeability structure is unknown at the Lucky Strike vent field, but most likely influenced by bounding faults and fracture network. We nevertheless use a similar permeability model as in the preceding case study for the EPR:

$$k = 2 \times 10^{-15} \times \exp(-3.6 \times 10^{-3} T) \quad (2.9)$$

$$k^* = k \times \exp(-6 \times 10^{-4} x) \quad (2.10)$$

where  $x$  is the absolute distance from 1500 m away from the ridge axis. The temperature in equation (2.9) is again the hypothetical steady state conductive temperature for the given boundary conditions and the magma chamber is assumed to be impermeable. The surface permeability of the Lucky Strike vent field at the spreading center is assumed to be  $\sim 2 \times 10^{-15} \text{ m}^2$ , which is lower than in the EPR case study. This is assumed to account for the idea that the crustal permeability at slow spreading ridges is generally lower than at their faster counterparts (Fouquet, 1997). Figure 2-8 illustrates the permeability structure for the simulations of Lucky Strike. Strictly speaking, the Lucky Strike vent field is situated below the critical end point of water so that boiling and condensation effects could be important. Two-phase phenomena cannot be accurately resolved in the here employed single-phase model and are neglected. Two simulations, i.e. flat surface and real bathymetric relief were performed. The number of elements in these simulations is approximately 1000 per square kilometer.

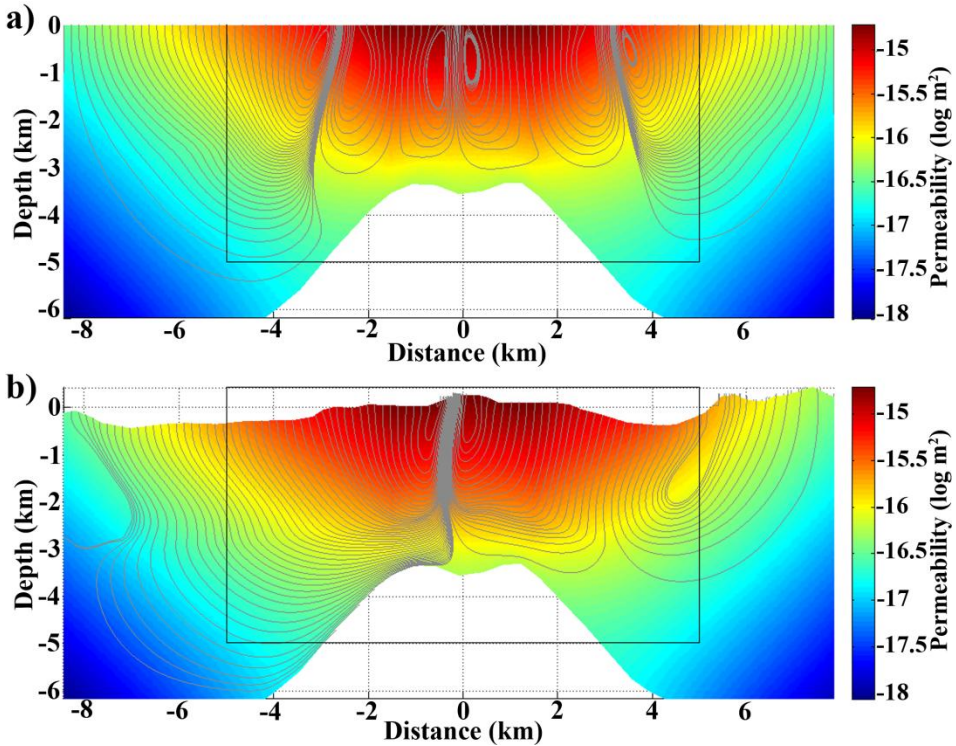


**Figure 2-8:** Permeability structure defined for Lucky-Strike vent field. The permeability decreases both with depth and the distance from the ridge axis. The black boxes in the figures are the domains plotted in fig. 4-9. Panel a) shows the permeability structure and late stage flow lines for the flat top simulation and b) for the simulation with bathymetric relief.

#### 2.4.2.3. Results

Convection initiates by the formation of several small plumes at the top of the magma chamber in the simulations with and without bathymetric relief (Figure 2-9a and c). Note that similar to EPR, the figure dimensions for presented results are limited to 5×5 km to demonstrate the vent-site more clearly. In the flat surface scheme, two plumes vent at the top of magma chamber after 3000 years of convection (Figure 2-9a). Multiple plumes are later formed which merge with previously formed plumes and cause interference resulting in the lateral movement of the vent sites at the surface. The system reaches a quasi-steady state where three plumes are present after 50,000 years of

## Controls of bathymetric relief on fluid flow

convection (Figure 2-9b). Note that far off-axis venting does not appear as the temperature gradient as well as the matrix permeability is not high enough to allow convection. The flow patterns show that relatively large convection cells appear above the magma chamber (Figure 2-8a).

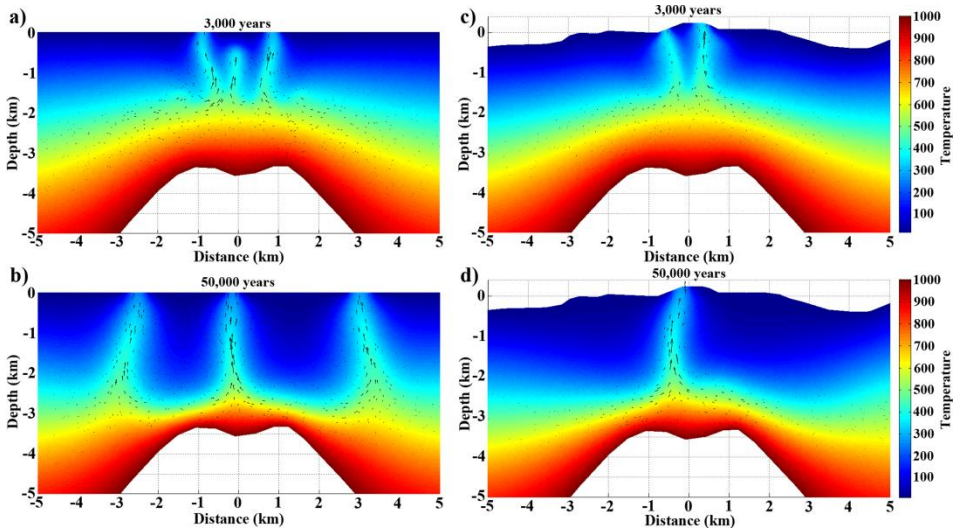


**Figure 2-9:** Two-dimensional cross-section of modeled temperature field for the Lucky Strike vent field at early (Figs. (a) and (c)) and late stages (Figs. (b) and (d)). The simulations show that in presence of topography, plumes always vent at local highs, whereas in the flat-surface simulation, plumes may vent off-axis. The late stage of the topographic model shows that vent field is located along the axis of the ridge (Figs. (b) and (d)). The figures are limited to 5×5 km to show the vent-site more clearly.

Similar to the EPR case study, the simulation that neglects bathymetric effects never predicts exclusive venting at the central volcano and is therefore inconsistent with observations. Only when the effects of bathymetric relief are included, the plumes coalesce to form a single upwelling zone below the vent field on top of the central volcano. Plumes initiating away from the central vent field (Figure 2-9d) will also merge with this central plume and system reaches a steady state. The simulations confirm that bathymetric relief can also have strong controls on vent site location at slow spreading ridges. Here we have

only looked at the special case of the Lucky Strike segment, which shows an on-axis melt lens. Due the significant bathymetric relief of slow-spreading ridges, on- as well as off-axis venting at different ridge segments may well be strongly controlled by bathymetry – in addition to detachment faulting, fracturing and phase separation in multi-component fluids.

### **2.5. Conclusions**

We have explored the effects of bathymetric relief on hydrothermal convection in a series of synthetic numerical experiments and two case studies. The presented hydrothermal convection model with unstructured meshes allows us to resolve the effects of bathymetric relief. Venting tends towards bathymetric highs as a result of bathymetry and temperature induced pressure variations in submarine hydrothermal systems. Simulation results using a single plume and bathymetric high allow us to predict the maximum plume deviation from its origin as a function of the wavelength and amplitude of seafloor relief as well as the depth to the heat source. The surface slope in simulations with multiple plumes and multiple highs controls the amount of venting expected at bathymetric highs. At fast spreading ridges, the axial high helps to focus venting directly onto the ridge axis. Pervasive and deeply penetrating across-axis flow which is thought to shape the hot crust at fast-spreading ridges can be reconciled with on-axis venting if bathymetric effects are accounted for. The Lucky Strike case study shows that also on slow-spreading ridges bathymetric relief results in focusing of hydrothermal venting at bathymetric highs – at least for systems in a magmatic phase with an axial magma chamber. Our findings demonstrate the importance of including bathymetry in simulations of submarine hydrothermal flow. In addition to the here presented results on oceanic spreading centers, bathymetric effects should also be important for other submarine vent systems like arc volcanoes, caldera structures, and seamounts.



## Chapter 3

The effects of sill intrusions on hydrothermal flow and thermal maturity in sedimentary basins: a case study from the Gjallar Ridge, off Norway



# **The effects of sill intrusions on hydrothermal flow and thermal maturity in sedimentary basins: a case study from the Gjallar Ridge, off Norway<sup>2</sup>**

*Bani-Hassan, N., Rupke, L., Berndt, C.*

## ***Abstract***

The causes and consequences of hydrothermal convection triggered by sill intrusions into sedimentary basins are explored using numerical modeling techniques. In particular we study the impact of hydrothermal convection on the thermal history of the Vøring Basin, which is part of the Norwegian volcanic margin. In the Gjallar Ridge area, multichannel seismic data show numerous sill intrusions as high velocity reflectors, likely emplaced during the opening of the Atlantic Ocean. To study their impact on the thermal history of the Gjallar Ridge, we have coupled a 1D basin reconstruction model with 2D fluid flow simulations that is based on 3D seismic data interpretation. The results show that sill intrusions are likely to trigger a short-lived phase (<10 Ka) of hydrothermal convection and that circulation pathways are highly influenced by fault and fracture networks. These findings show that hydrothermal convection

---

<sup>2</sup> In preparation for submission in the Journal of Basin Research

is a natural consequence of sill intrusions and has first order control on the maturation and thermal history of the surrounding and in particular overlying sediments, and should therefore be considered in reconstruction studies of volcanic margins as well as for the assessment of hydrocarbon maturity.

### **3.1. Introduction**

Extensional rifting of the lithosphere results in sedimentary basin. Continuous extension leads to continental break-up and formation of passive margins. Passive margins are classified based on the volume of magmatism to two end-members of volcanic and non-volcanic margins (Mutter et al., 1988). Non-volcanic margins, such as the Iberian Margin, are associated with intense crustal thinning, mantle unroofing and wide continent-ocean transition zones but only limited magmatic activity prior to seafloor spreading (Boillot and Froitzhelm, 2001). In contrast, volcanic passive margins, such as the Norwegian Margin, are characterized by extensive intrusive and extrusive magmatic activity at the time of break-up (Geoffroy, 2005). Extrusive volcanism evident as seaward-dipping seismic reflectors and intrusive sills and dikes as well as high-velocity lower crustal bodies (White et al., 1987), which are typical for this type of margin. In their sum, these volcanic rocks constitute significant magmatic crustal thickening (Gernigon et al., 2006). The thermal history of the sediments is, therefore, intrinsically linked to the intense magmatic activity at volcanic passive margins.

Several consequences can be observed as a result of sill injection into sedimentary rocks. For example, metamorphic contact aureoles around sill intrusions show that sill intrusions greatly enhance thermal maturity (Galushkin, 1997). In addition, the hot emplaced sills are able to trigger hydrothermal convection within the porous sediments saturated by sea water. The circulation of hot fluids through the rock matrix leads to physicochemical reactions between the fluids and buried organic matter thereby enhancing the susceptibility of organic rocks to generate hydrocarbons. Besides, the fluids discharging from the sediments enter into the sea and possibly into the

atmosphere. In fact, a geosphere forcing on climate through the release of greenhouse gases produced during contact metamorphism has been hypothesized for past hydrothermal events such as the Paleocene-Eocene Thermal Maximum PETM (e.g. Hesselbo et al., 2000; Svensen et al., 2004).

Former studies on thermal effects of sills on sediments have mainly focused on conductive heat transport and have neglected the complexity of hydrothermal circulation induced by sill intrusions (e.g. Fjeldskaar et al., 2008; Aarnes et al., 2010). Petrological studies demonstrate that the temperature of host rock prior to sill emplacement is generally much lower than the temperature of injected magma (Galushkin, 1997); therefore, the hot injected sills could largely influence the thermal regime of sediments. Conductive cooling models suggest that a single hot magmatic intrusion can affect the maturity of the surrounding rocks up to the distance equal to its thickness (e.g. Galushkin, 1997). The actual impact of hot sills on the adjacent sediments is, however, not accurately captured by conductive models as hydrothermal convection is neglected. While heat diffusion only affects the sediments in the direct vicinity of the sill intrusions, circulation of hot fluids may also heat sediments at greater distance. In addition, the sills having a thickness of 10s of meters cool faster when convection is accounted for and consequently, the surrounding sediments are generally affected by short-lived heat pulses as a result of moving narrow hydrothermal plumes. Since the maturity of rocks is a function of temperature and time, conductive cooling leads to over-estimation in the maturity of adjacent sediments. Therefore, to find an appropriate estimation for the maturity of rocks in volcanic passive margins, a convective model is crucial. Besides, as the passive margins generally undergo complex thermal regime throughout tectonic and possible magmatic activities before continental break-up, the thermal history of sediments should be reconstructed at the time of sill injection.

Previous studies did partially address hydrothermal convection triggered by intrusions. These numerical studies are mainly focused on the volume of sediments affected by sills (e.g. Wang et al., 2006), the burial depth of intrusions as a factor of controlling convection (e.g. Eldursi et al., 2009) and

convection patterns formed by single sills (e.g. Polyansky and Reverdatto, 2006). The impacts made by a swarm of simultaneously emplaced sills are, however, not understood yet. Another factor which controls heat dissipation is the lateral variability of sediment permeability. Thermal fracturing and extensional faulting open new pathways for fluids to move rapidly and reach distant regions. Studies considering convective cooling of transient heat sources have generally ignored matrix heterogeneities. In addition, the permeability structure and fracture networks as well as geometry of sills strongly influence the duration of hydrothermal activity. By assuming a thick pluton as an engine for hydrothermal convection in a compacted low-permeable host rock, the associated hydrothermal activity can be sustained up to a million year (Cathles, 1977). However, the duration of hydrothermal convection has not yet been modeled in presence of thin sills in a fractured host rock. In this paper, we model a complex thermal regime induced by a swarm of sills which have presumably been emplaced simultaneously, considering matrix heterogeneities and pre-break up thermal history of basin.

To explore the effects of sill intrusion into sediments, we present a 2D single-phase model that resolves hydrothermal flow, which is applied in a case study to the Vøring Basin. The sediments on Gjallar Ridge, a structural high in the Vøring Basin, are affected by a swarm of sills presumably emplaced during North-Atlantic break-up at the Paleocene-Eocene transition (Svensen et al., 2004). The importance of this region is not only due to the presence of the sills, but due to a large number of vent-sites observed in the Paleocene sediments as well. The objective of this study is to achieve an accurate thermal reconstruction of the sediments which accounts for lithospheric thinning, sediment blanketing, subsidence by compaction and isostasy effects, as well as an accurate estimation of rock maturity considering possible fluid convections and their pathways after the sills were injected.

### **3.2. Geological setting of Gjallar Ridge**

The large sedimentary Vøring Basin is located within the North Atlantic volcanic province. The Vøring Marginal High in the west and the Trøndelag Platform in the east bound the Vøring basin. Main rift episodes in the early–mid Devonian, Carboniferous, late Permian–early Triassic, Jurassic–earliest Cretaceous and latest Cretaceous–Paleogene created the present arrangement of structures in the Norwegian sea continental margin between 62°N and ~68°N (Blystad et al., 1995; Brekke et al., 2001; Bukovics et al., 1984; Doré et al., 1999; Gabrielsen et al., 1999; Reemst and Cloetingh, 2000; Roberts et al., 1999 and Ziegler, 1988).

Extensional tectonics during the Devonian to the earliest Cretaceous led to continental rifting. Extension of the mid-Norwegian margin in the late Jurassic–early Cretaceous segmented the Vøring Basin into several sub-basins generating structural highs and grabens. A long period of post-rift regional thermal subsidence followed this rift episode for 60 Ma from Ryazanian to Campanian, without major faulting (Faereth and Lien, 2002; Hansen et al., 2005). Throughout the Cretaceous, the direction of stress changed from E-W throughout the Jurassic to NW-SE (Bartholomew et al., 1993; Lundin and Dore, 1997). The structural configuration in this area is a result of complex variations in this stress regime. The last major rift episode occurred throughout the latest Cretaceous–Paleocene and break-up occurred in the latest Paleocene–early Eocene, approximately 55 Ma before present (Vogt and Avery, 1974), when North Atlantic rifting had progressed and consequently, the Vøring Marginal High and the main structure of the Gjallar Ridge were formed (Doré et al., 1999; Roberts et al., 1999; Hansen et al., 2005). The last major rift episode marks the termination of continental rifting and the beginning of seafloor spreading in the North Atlantic (Faereth and Lien, 2002). Normal and low-angle detachment faults in the Gjallar Ridge area suggest a ~20 Ma syn-rift phase prior to break-up (Ren et al., 1998). Initial basement subsidence in this rift episode from Campanian to Maastrichtian was followed by significant uplift possibly as a result of melt production and igneous rock emplacement at the

base of lithosphere as well as rift flank uplift prior to break-up; whereas, thermal subsidence is the major effective post-rift process at this stage (Ren et al., 1998).

The volcanic Vøring Marginal High and strong volcanism at the boundary between the outer edge of the earlier rift basin and the formation of oceanic crust are associated with continental break-up (Brekke, 2000). Based on seismic data acquired in the Vøring Basin, both intrusive and extrusive magmatic structures have been discovered (Eldholm et al., 1989; Skogseid et al., 1992). The huge number of semi-parallel thin sills and dykes that intrude Mesozoic sediments (Fjeldskaar et al., 2008) are recognized in a relatively wide area (100-200 km). In addition, lower crustal bodies with seismic velocities exceeding 7 km/s have been found beneath the outer Vøring margin (Skogseid et al., 1992; Mjelde et al., 1998).

The observation of mud diapirs with high-amplitude gas anomalies formed in Tertiary sediments have led to the inference of significant amounts of hydrocarbons in the Gjallar Ridge area Corfield et al., 2004. Besides, the presence of hydrocarbons is confirmed in an exploration well (6704/12) in the Gjallar Ridge area (Corfield et al., 2004). Therefore, several geophysical studies have been carried out including a 3D multichannel seismic survey to understand the subsurface structures in this area. For this study, we have interpreted the 3D seismic data including horizon, fault and sill interpretation and selected a representative transect in the dip direction of the main structural features to model the thermal evolution of the sediments after sill emplacement.

### **3.3. Modeling approach**

In order to reconstruct the thermal history of the sediments in the Gjallar Ridge region, we use a coupled approach that combines a 1D basin reconstruction model with a 2D fluid flow solver. The results of the 1D basin reconstruction elucidate the overall structural and thermal history of the Vøring Basin throughout the last three major rift episodes until the present. The reconstructed temperature at the Paleocene-Eocene transition (break-up) is then

used as the initial background temperature of the sediments for the 2D fluid flow simulations investigating hydrothermal convection driven by sill emplacement. The predicted temperature field throughout 10,000 years of convection was then fed back into the 1D basin reconstruction in order to predict the present day thermal maturity. This coupled 1D reconstruction and 2D fluid flow modeling approach gives us thorough insights into the thermal history and maturity of sediments in the Gjallar Ridge region.

### 3.3.1. One-dimensional basin reconstruction

The 1D basin reconstruction is performed using TecMod1D by GeoModelling Solutions GmbH. TecMod1D couples a lithosphere scale forward model for rifting, isostasy, temperature, sedimentation, and compaction with an inverse scheme for automated parameter update for stratigraphy fitting. The updated model parameters are crustal and mantle stretching factors as well as the paleo-water depth. The outcome of the TecMod reconstruction is a fully consistent tectonostratigraphic forward model of the formation of the Gjallar Ridge. The details of this reconstruction approach are given in Rupke et al. (2008) and Rupke et al. (2010). TecMod requires an input stratigraphy with interpreted horizons down to the basement. Here we use the stratigraphy provided by Faleide et al. (2008) for the Euromargins transect 3 that crosses the Northern Gjallar Ridge.

### 3.3.2. Two-dimensional fluid flow

To understand the effects of sills on the sediments at the time of break-up, we need to model the fluid flow driven by the sill intrusions. The two-dimensional fluid flow model is based on Darcy's law:

$$\vec{u} = -\frac{k}{\mu_f} (\nabla P - \rho_f \vec{g}) \quad (3.1)$$

where  $\vec{u}$  corresponds to Darcy velocity,  $\rho_f$  to fluid density,  $k$  to permeability,  $\mu_f$  to dynamic viscosity,  $g$  to gravitational acceleration and  $P$  to pressure.

For the relatively short time scales of hydrothermal convection around sills, sedimentation and subsidence can be neglected so that no solid movement needs to be taken into account. The energy conservation equation is therefore reduced to:

$$\left(\phi\rho_f c_{pf} + (1-\phi)\rho_m c_{pm}\right)\frac{\partial T}{\partial t} + \rho_f c_{pf}\vec{u}\cdot\nabla T = \nabla\cdot(\kappa\nabla T) \quad (3.2)$$

where  $c_p$  is specific heat capacity,  $T$  is temperature,  $t$  is time,  $\phi$  is matrix porosity and  $\kappa$  is thermal conductivity of the matrix. Subscripts  $m$  and  $f$  denote matrix and fluid, respectively. The second term on the left-hand side represents energy transfer due to fluid advection.

One more constitutive equation is mass conservation in porous media:

$$\phi\frac{\partial\rho_f}{\partial t} = -\nabla\cdot(\rho_f\vec{u}) \quad (3.3)$$

Note that porosity does not change over the runtime of the fluid flow simulations so that it can be taken out of the time derivative. A pressure equation can be derived by substituting eqn.(3.1) into eqn.(3.3) and splitting fluid density into pressure and temperature terms:

$$\phi\rho_f\beta_f\frac{\partial P}{\partial t} = \nabla\cdot\left[\frac{k\rho_f}{\mu_f}(\nabla p - \rho_f\vec{g})\right] + \phi\rho_f\alpha_f\frac{\partial T}{\partial t} \quad (3.4)$$

where  $\alpha_f$  is fluid thermal expansion coefficient and  $\beta_f$  is isothermal compressibility of fluid.

Fluid properties, i.e. density, viscosity and specific heat capacity are computed using the PROST library for given temperature and pressure at every time-step according to the IAPWS-84 equation of state (Bauer, 1998).

The matrix porosity is kept constant with time in sediments, but decreases exponentially by increasing the depth. Note that precipitation and dissolution of minerals are not taken into account. A commonly-used estimation for a simple porosity-depth relationship in the sediments is given by Athy (1930):

$$\phi = \phi_0 \exp\left(-\frac{z}{z_0}\right) \quad (3.5)$$

where  $\phi_0$  is surface porosity,  $z_0$  is compaction length scale depending on given lithology and  $z$  is the depth. The compaction laws used here are the same as the ones used in the 1D reconstruction.

Permeability substantially decreases with porosity. However, there is no specific equation describing the relationship between porosity and permeability that is valid for all porous media as it is highly dependent on the structural configuration and sediment type. This fact is due to different pore sizes and pore connectivities in different formations. Considering two parameters of lithotype-dependent scaling factor ( $\eta$ ) and specific surface area ( $S$ ) for each formation, a reasonable estimation for the permeability is derived by a revised version of the Kozeny-Carman relationship between porosity and permeability (Ungerer et al., 1990):

$$\begin{cases} k(\phi) = 2 \times 10^{16} \eta \frac{\phi^{15}}{Sc^2(1-\phi')^2} & , \text{ if } \phi' < 0.1 \\ k(\phi) = 2 \times 10^{14} \eta \frac{\phi^{13}}{Sc^2(1-\phi')^2} & , \text{ if } \phi' > 0.1 \end{cases} \quad (3.6)$$

where corrected porosity,  $\phi'$ , is given by:

## Effects of sills on fluid flow and thermal maturity

$$\phi' = \phi - 3.1 \times 10^{-10} Sc \quad (3.7)$$

**Table 2:** Model Parameters for Gjallar Ridge case study.

Parameter	Symbol	Values	Units
Density of fluid	$\rho_f$	Based on EOS	$kg\ m^{-3}$
Dynamic Viscosity of fluid	$\mu_f$	Based on EOS	$kg\ m^{-1}\ s^{-1}$
Kinematic Viscosity of fluid	$\nu_f$	Based on EOS	$m^2\ s^{-1}$
Specific heat capacity of fluid	$c_{pf}$	Based on EOS	$J\ kg^{-1}\ K^{-1}$
Pressure	$P$		$kg\ m^{-1}\ s^{-2}$
Temperature	$T$		$K$
Darcy Velocities	$\vec{u}$		$m\ s^{-1}$
Density of Matrix & Sills	$\rho_m$	2690	$kg\ m^{-3}$
Specific heat capacity of Matrix	$c_{pm}$	1000	$J\ kg^{-1}\ K^{-1}$
Porosity of Matrix	$\phi$	Based on eqn. (3.5)	
Permeability of Matrix	$k$	Based on eqn.(3.6)	$m^2$
Thermal conductivity	$\lambda$	1.86	$W\ m^{-1}\ K^{-1}$
Gravitational acceleration	$g$	9.81	$m\ s^{-2}$
Arrhenius factor	$Ar$		$K$
Ideal gas constant	$R$	8.3145	$J\ mol^{-1}\ K^{-1}$
Activation energy	$E$		$J\ mol^{-1}$
Specific surface area	$Sc$	$10^{-6}$	
Scaling factor	$\eta$	10	$m^2/m^3$
Time	$t$		$s$

The diffusion part of the energy equation and the fluid pressure equation are solved using a MATLAB-based Finite Element Method Dabrowski et al. (2008), while temperature advection is resolved with a semi-Lagrangian scheme. Details of the space and time discretization as well as implementation for the 2D fluid flow simulation are described in Bani-Hassan et al. (2012).

To explore the thermal history of the sediments, vitrinite reflectance is used as a measurement of maturity of organic matter in the rocks (e.g. Bostick, 1971; Simoneit et al., 1981; Robert, 1981; Fjeldskaar et al., 2008). Aside from the fact that this method is more accurate than other studied methods of maturity evaluation, i.e. Time-Temperature Index (TTI) to vitrinite reflectance correlation and  $\log(\%Ro)$  to depth correlation (Morrow and Issler, 1993), it is also not influenced by variations in composition of Kerogen (Dow, 1977). Vitrinite reflectance increases exponentially with rock maturity (Dow, 1977) from ~0.25% to ~4.7% Ro as a function of temperature and time. The values greater than 4.7% Ro are not reliable in this method. Sensitivity of vitrinite reflectance to the temperatures associated with hydrocarbon generation, i.e. 60-120°C, draws our interest to use it as a proxy for rock maturity. The onset of hydrocarbon generation is associated with vitrinite reflectance of 0.5% Ro. The reflectance values up to 1.0% Ro are interpreted as oil and above this value only wet or dry gas could exist (Dow, 1977).

The kinetic model of vitrinite maturation (EASY% Ro) is usually considered as the primary method for estimation of rock maturity in basin modeling. In the kinetic method, the vitrinite maturation is expressed by  $n$  independent first-order Arrhenius reactions (Sweeney and Burnham, 1990). The following correlation relationship provides good accuracy for vitrinite reflectance based on this method:

$$Ro\% = \exp(-1.6 + 3.7Tr(t)) \quad (3.8)$$

where  $t$  is time and  $Tr$  is Transformation ratio (a scale which indicates how much Kerogen can transform to hydrocarbon) which can be evaluated by (Tissot and Espitalie, 1975):

$$Tr(t) = \sum_1^n \left\{ 1 - \exp \left[ - \int_{t_0}^t K_i(t') \cdot dt' \right] \right\} \quad (3.9)$$

where  $K_i$  is  $i$ -th reaction rate and can be derived by:

$$K_i(t) = Ar_i \exp(-E_i / RT(t)) \quad (3.10)$$

where  $Ar$  corresponds to the Arrhenius factor,  $E$  to its activation energy and  $R$  to the ideal gas constant. The values for the parameters of the EASY% Ro are provided by Burnham and Sweeney (1989).

### **3.4. Basin analysis**

#### **3.4.1. Geophysical assessment and interpretation**

Figure 3-1 shows the location of Gjallar Ridge in the Vøring Basin. The 3D multichannel reflection seismic survey SG9604 was acquired by Saga Petroleum Company in 1996. The 3D-dataset covers an area of about 2000 km<sup>2</sup> with inline and crossline spacing of 18.75 m. The processing included frequency filtering, multiple suppression and post-stack time migration. Data penetration is approximately 14 km (8 s TWT) and the block is located along the north-east of Gjallar Ridge (Figure 3-1, black box). We interpreted the entire 3D seismic data set in the interactive seismic interpretation software Kingdom Suite. Interpretation revealed several sill intrusions and faults in the study area (Figure 3-2). The exploration well is located at 67° 7' 25"N 4° 42' 44.7"E northwest of the survey area. The well reaches a depth of 4100 m below the seafloor, penetrating 2.8 km below the base of the Tertiary unconformity (a discontinuity in sedimentation in Paleocene observed 2.7 to 3 km below sea level). Available well logs include sonic, bulk density, neutron porosity, resistivity and gamma

ray. For depth conversion of the two-way time seismic data we used check shot information.

Following the interpretations of Berndt et al. (2000), Planke et al., (2006), and Hansen et al. (2006) we interpret the abruptly-terminating high-amplitude reflectors as possibly sheeted olivine-gabbroic sills. Their most likely emplacement time was close to continental break-up about 55 Ma (Svensen et al., 2004). The magmatic intrusions are saucer-shaped, coherent, and semi-parallel to each other and to the bedding reflectors. The seismic cube contains numerous sills which are buried between 3.5 and 8 km below sea level in Cretaceous sediments. Seismic reflection data as well as wide-angle seismic travel time modeling and amplitude modeling suggest the thickness of sills varies between 30 and 100 m and their lateral extension reaches up to several kilometers (Berndt et al., 2000). This is consistent with field observations on Triall Øya (East Greenland). Clearly, thicker sills exhibit stronger reflections from the top and base. The top and bottom of the sills are characterized by abrupt changes in velocity, and a zone around the sills with a gradual velocity decrease from the sills toward the sediments is observed (Berndt et al., 2000). This phenomenon is explained to be a result of contact metamorphism (Fowler and Nisbet, 1982). Since the sills are highly reflective due to the high acoustic impedance contrast with the sediments, little energy transmits through the sills. In addition, heterogeneities in the matrix lead to ray scattering and diffraction; therefore, geological structures beneath the sills are not imaged well.

Several normal faults exist in the northern part of the Gjallar Ridge. They are the result of late Cretaceous rifting (Ren et al., 1998) and strike in NE-SW direction in the central and northern parts of the Gjallar Ridge area. It is possible that some of the faults detach onto a major mid-crustal detachment fault. The faults probably constitute zones of increased permeability that may control the pathways of hydrothermal flow. The faults are abundant at shallow depths (up to ~2 km below the unconformity) and terminate against the break-up unconformity. Also, there is a tier of polygonal faults within the fine-grained Miocene sediments (above the unconformity). These are probably related to

dehydration and compaction (Gay and Berndt, 2007) rather than tectonic forces. These faults have a smaller vertical extent. As there is no reliable information on the effect that they have on the permeability variations of the host rock they are not modeled in the 2D simulation.

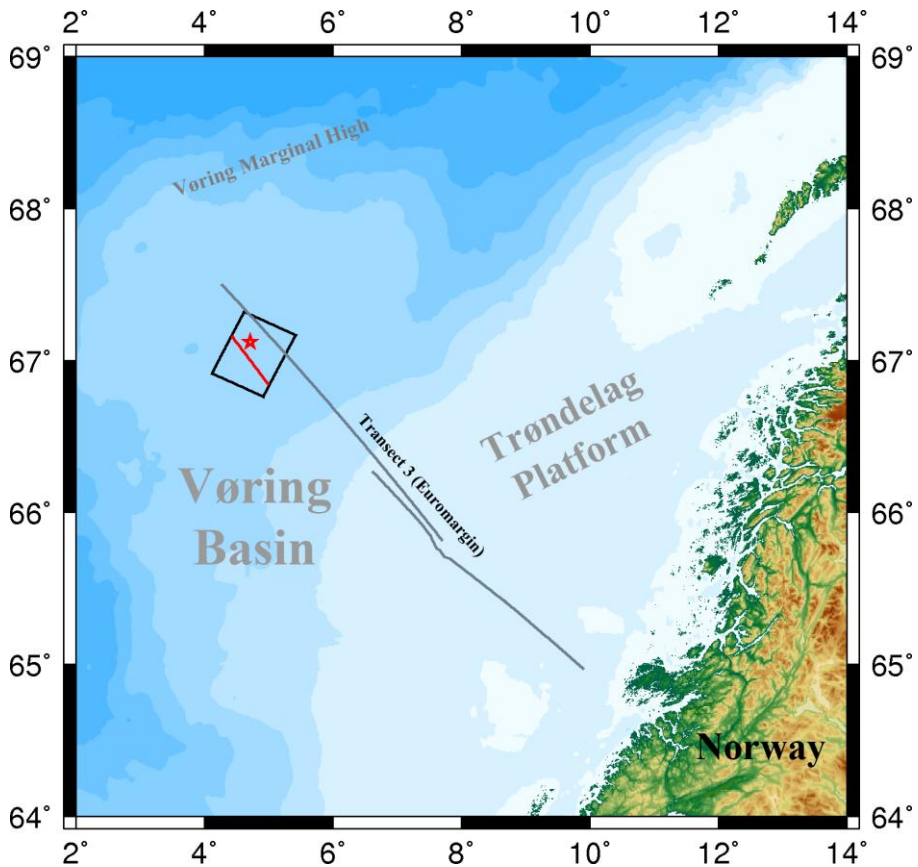


**Figure 3-1:** Location of Gjallar Ridge area in Vøring Basin. The black box is where 3D multichannel seismic is recorded. The red line in the box is the transect on which 2D hydrothermal simulation is performed and exploration well 6704/12 is marked by a star. Euromargin transect 3 is taken from the interpretation by Faleide et al. (2008) for 1D basin reconstruction.

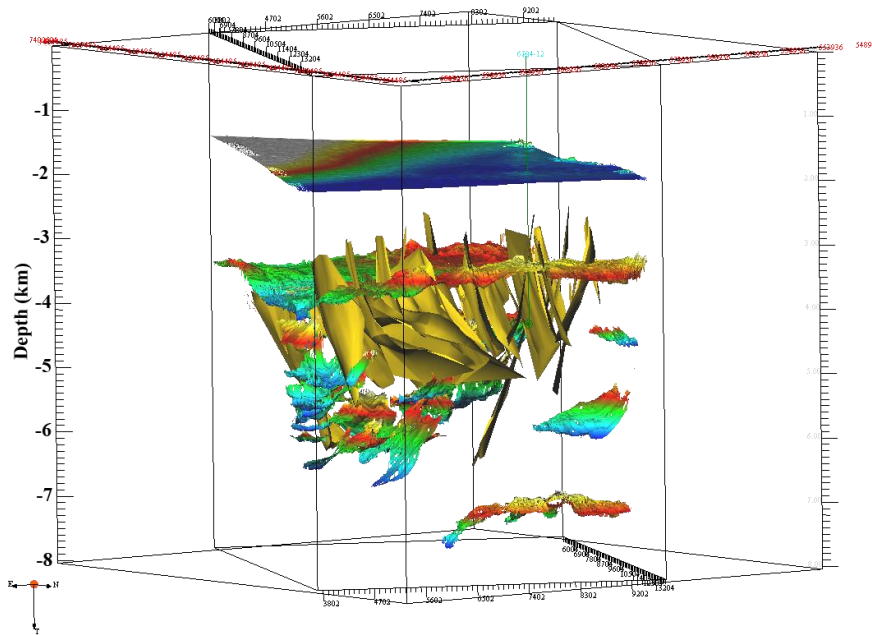


**Figure 3-2:** Interpreted 3D seismic reflection data in Gjallar Ridge area. Yellow surfaces are NE-SW faults terminated to deep-cutting faults. Several sill intrusions were detected below 3.5 km which extend up to 8 km depth. The sills are semi-parallel and supply the heat required for a hydrothermal convection. A well (6704/12) has been drilled up to 4100 m from seafloor in N-W of the region.

### 3.4.2. Basin reconstruction

The one-dimensional basin reconstruction is performed at a representative location on top of Gjallar Ridge. As an input stratigraphy for the reconstruction, we use the published interpretation of the Euromargins transect 3 by Faleide et al. (2008) and have chosen to perform a 1D reconstruction at the Gjallar Ridge. The input profile consists of 9 horizons down to the basement, including seafloor, Base Pleistocene, Base Pliocene, Top Eocene, Top Paleocene, Base tertiary, Intra Campanian, Top Turon and Base Cretaceous. The geological architecture developed throughout the last 290 Ma (Early Permian until present) which includes the last three main rift episodes of late Permian–early Triassic

(~250 Ma), Jurassic–earliest Cretaceous (~100 Ma) and latest Cretaceous–Paleogene (~55 Ma). Two other minor rift phases also occurred in Jurassic and Late Cretaceous times.

Further model parameters include an initial crustal thickness of 32 km and an isostatic compensation depth of 120 km. Bottom and surface temperatures in the model are set to 1300°C and 2°C corresponding to the temperatures of the asthenosphere and seawater, respectively. For simplicity and to facilitate consistency between the 1D and 2D simulations, we assume a homogenous sediment infill with the properties of a mixture of 80% shale and 20% sandstone. Similar to Rupke et al. (2008), we assume a constant thermal conductivity of 1.86 W/(m.K), which is within the typical range of effective thermal conductivities for fluid saturated sediments.

Figure 3-5 shows the predicted lithosphere temperatures through time. The temperature field is clearly controlled by the three rift phases. The black contour lines that mark the crust-mantle boundary, top basement, seafloor, and sea level illustrate crustal thinning. As the profile is in close proximity to the exploration well (6704/12), the data from the well can be used to benchmark the calculated values. Figure 3-3a shows the predicted present temperature structure along with the data from the well. The good match between the predicted and measured values shows that the simplified thermal conductivity model is a valid approximation. To further check that the 1D reconstruction is consistent with observations, we have computed the present vitrinite reflectance values. Figure 3-3b shows that the calculated background vitrinite reflectance values match quite satisfactorily the data measured in the well. These findings show that the results of the 1D basin model successfully reconstruct the thermal and structural evolution of Gjallar Ridge. We can therefore use the predicted temperature structure at 55 Ma as the initial boundary condition of the 2D fluid flow simulations.

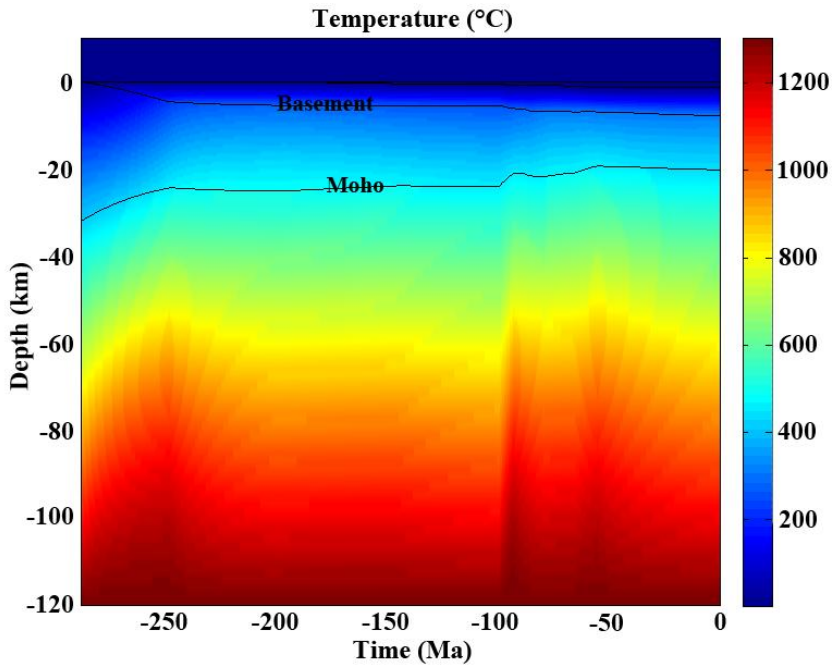


**Figure 3-3:** Temperature field through time obtained using 1D basin reconstruction. Three main rift phases at ~250 Ma, ~100 Ma and ~55 Ma lead to strong thermal variations in the basin. The thermal variation, however, does not vary much throughout main rift phases in the first 10 km in y-direction.

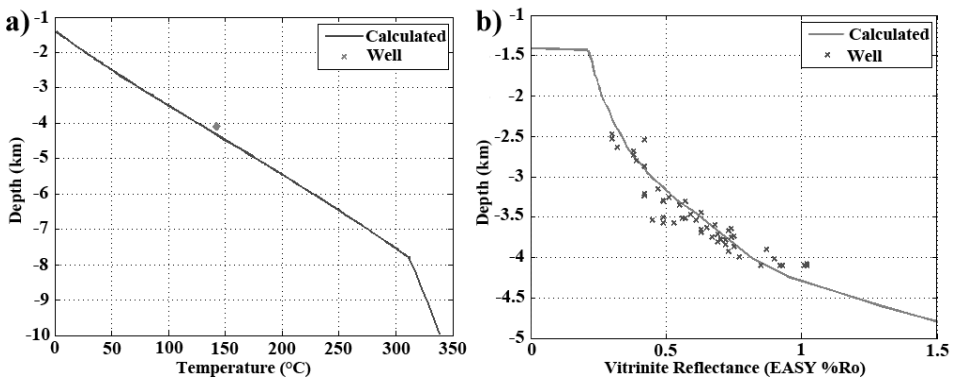


**Figure 3-4:** Measured vitrinite reflectance and temperature in the exploration well 6704/12. a) Measured well temperature is satisfactorily consistent with the values computed in the 1D basin reconstruction. b) The vitrinite reflectance values observed in the well matches with the calculated values using 1D basin reconstruction.

### **3.4.3. Fluid flow simulation driven by sill intrusions**

#### **3.4.3.1. Model setup**

To model hydrothermal fluid flow driven by sills in the Gjallar Ridge region, a straight NW-SE line in the depth-converted seismic cube is selected, interpreted and digitized (Figure 3-5). Several sills and faults as well as seismic evidence for fluid flow can be identified along the transect. Since the base Tertiary unconformity is formed prior to the break-up and sill emplacement is presumably occurred at the time of break-up, we assume that the first detected layer above the unconformity constitutes the upper boundary of the model. The mean depth of this layer is 2.8 km below the present sea level and the depth of the model extends down to 10 km below seafloor. The length of the modeled transect is 25 km. The selected line is only ~10 km away from well 6704/12 and therefore, the physical properties measured in the well can be extrapolated onto the transect.

Evidence of hydrothermal activity can be detected in the sediments beneath the unconformity. The hydrothermal activities are indicated by vertical, coherent low amplitude events towards the surface on the seismic data similar to the structures reported by Planke et al., (2006). These structures are mainly observed either near shallow sills or major faults, where hydrothermal convection likely occurred at the time of sill emplacement.

The model resolves for a 2D fluid flow simulation within a three-node unstructured mesh of elements having an average size of 1130 m<sup>2</sup>. The size of elements is set to be variable depending on the thickness of structural events to maximize the effective resolution, i.e. larger number of elements in near faults and sills; therefore the element size in the faults and sills is up to two orders of magnitude smaller than the matrix.

In this model, the upper surface allows the fluids to come into the model or leave it freely, whereas the sides as well as the bottom of the model are impermeable. In addition, no heat flux is allowed through the sides. We assume

a sill emplacement temperature of 1000°C analogous to mafic sills. The permeability in the sills is assumed three orders of magnitude less than average permeability of surrounding rocks; therefore almost no convection was allowed through them. This is realistic for the initial situation while the magma is still hot, but it is likely that after cooling the sills have significant fracture permeability. However, the assumption of low permeability for the sills should hold as contact metamorphism will seal the sills and therefore no fluids should flow through the sills once the system starts to cool. The sills are assumed to be injected into the model simultaneously and instantaneously, while no post-emplacement magmatic flow was allowed. Additionally, the permeability in the faults is prescribed three orders of magnitude higher than the average permeability of matrix.

The matrix and fluid properties are listed in Table 1. Pressure is initialized at hydrostatic values assuming that the paleo-seafloor was at 1500 m water depth. The minimum depth of sills below the upper model boundary is ~1500 m which makes the pressure at the location of sills considerably higher than the critical point of pure water; therefore, only a small portion of venting fluid goes into the two-phase region which does not affect the location of venting at large scale. Since the shallow sills cool rapidly and vent at low temperatures and therefore, two-phase effects for thermal maturation are negligible, we assume that the fluids are at supercritical condition. Similar to one-dimensional reconstruction, the constant thermal conductivity used in the simulation is an average of matrix and fluid values.

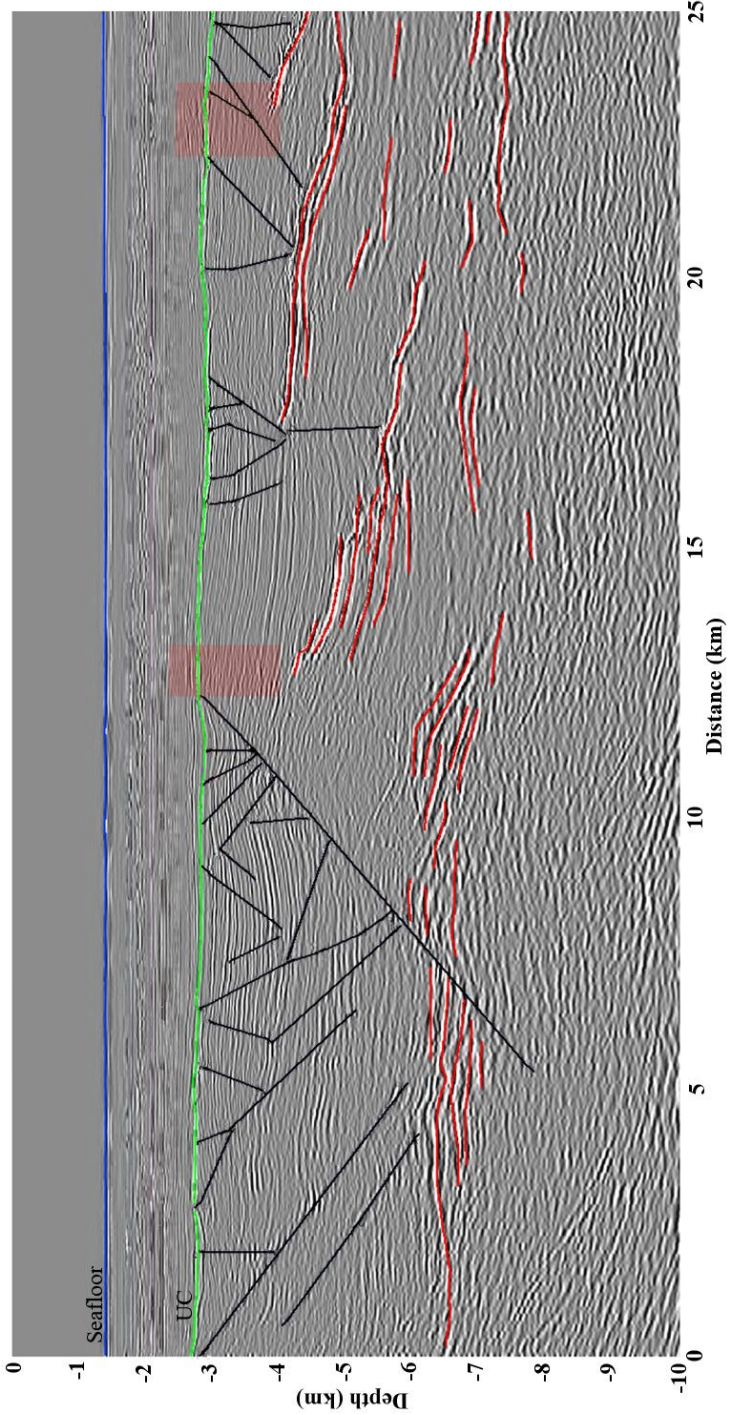


**Figure 3-5:** A selected transect in the seismic cube on Gjallar Ridge. The blue and green reflectors are seafloor and base Tertiary

unconformity, respectively. Two major vent fields are detected and marked by red shaded boxes. Several faults and sills are observed below the unconformity. Evidence for hydrothermal activity can be seen in the red shaded boxes.

### 3.4.3.2. **Thermal evolution**

As discussed earlier, the Gjallar Ridge is dissected by numerous shallow and deep-cutting faults as well as several sill intrusions. The sills provide the required heat for triggering hydrothermal circulation. To understand the thermal evolution in the sediments, two models are constructed: (i) only conduction is responsible for the cooling of sill intrusions, which provides us with a reference model for comparison, (ii) the sills are cooled by diffusion and hydrothermal convection. The models are run up to 10 ka, when the maximum temperature of the sills is approximately 1/e of the initial temperature.

Figure 3-6 shows the simulation results after 10, 50, 500 and 3000 years of convection. Several convection plumes form very quickly above the shallow sills at the initial stage of the simulation (Figure 3-6a). Since the permeability of matrix decreases exponentially with depth, convection in shallower regions is stronger and therefore, the sills cool substantially faster. Accordingly, we can conclude that in tilted sills, convection starts from the upper parts. At some regions in the model, e.g. between transect kilometers 12 and 20, sill intrusions are closely spaced and almost parallel to each other. The heat stored within each sill therefore affects the sediments in between resulting in a strong thermal zone.

After 50 years of convection, hydrothermal plumes also start to form above the deeper sills (Figure 3-6b). Numerous faults between 5 and 10 km distance act as recharge conduits. Venting occurs at numerous sites along the transect but mainly above the shallow sills. For example, at 12.8 and 23 km distance, the two vent fields confirm the hydrothermal activities observed in the seismic section. The shallow swarm of sills as well as the associated considerable thermal gradient form strong convections near the observed vent structures on

the transect which discharge hot fluid regardless of the location and distribution of faults.

Figure 3-6c illustrates the thermal history of the model after 700 years of convection. At this stage, the maximum venting temperature does not exceed 200°C as the shallow sills are already cooled down to ~300°C and the fluids originated from deeper hotter sills lose their temperature during their ascent. The results at this stage show that high-temperature venting (>200°C) is short lived, generally less than a millennium. Since faults and cracks provide very high permeability zones, several plumes are focused along faults during their ascent toward the surface. The result also suggests that the role of faults changes with cooling progress, i.e. some faults turn out to be discharging where initially they played the role of recharge zones and some other faults are both recharging and discharging zones. At transect km 8 at 5 to 6 km depth the ascending plume changes its pathway as soon as it reaches the recharging fault. Since the fault is highly permeable, it allows the hot fluid to migrate; as a result the upwelling plume partially warms up the recharging fluid and then, continues ascending towards the surface through other discharging faults present in the vicinity. Fluids barely penetrate the regions where the sills are parallel and in close proximity. Consequently, the cooling process in these regions takes longer compared to the same amount of heat provided by single separated sills. Lack of clear sediment layering in the seismic section between transect km 8 and 13 could be a result of strong episodic hydrothermal convection. This region terminates at a deep-cutting overlying fault, which suggests a dominant role of the fault in fluid migration.

Finally, Figure 3-6d shows the temperature field after 3000 years of convection. The convection currents driven by shallow sills have almost shut down. In this case, dominant ascending hot fluids originate from deeper sills and their pathways are controlled by deep faults. All the sills have contributions in the fluids discharging from the seafloor except those underlain by large sheeted sills in which hot fluids are trapped below them and form relatively hot zones.

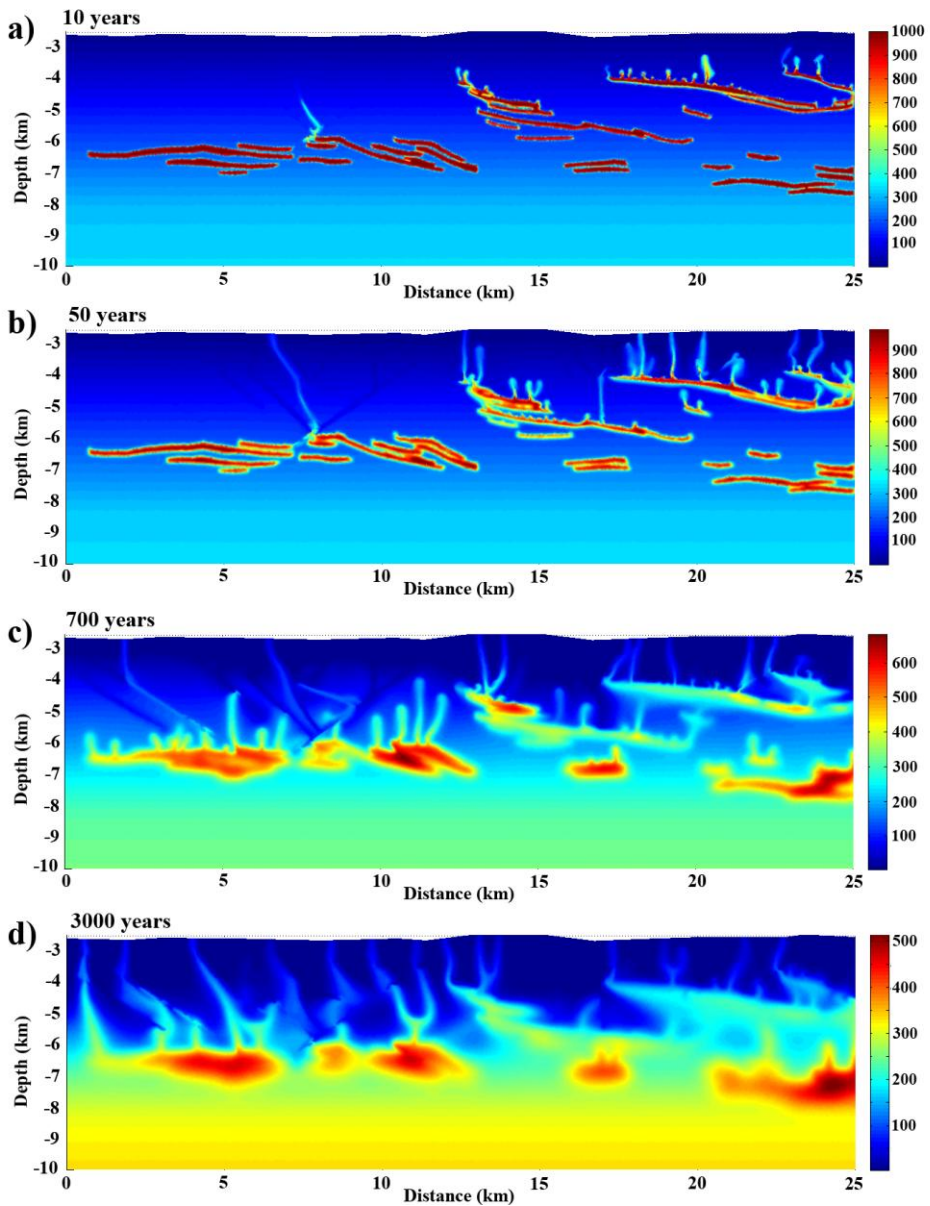


**Figure 3-6:** Thermal evolution of Gjallar Ridge after sill emplacement. a) onset of convection after 10 years. Convection starts from the top of shallow sills. b) Convection starts from deeper underlying sills after 50 years of convection. The plumes reached the surface at this stage. c) Hydrothermal convection after 700 years; in the first 10 km distance of the transect, the fluid flow is mainly fault controlled. The shallow sills cooled down up to 300°C. Parallel adjacent sills play act as a single thick sill and provide strong thermal anomaly. d) Hydrothermal

convection after 3000 years; shallow sills have been cooled down up to ~200°C and only deep sills sustain the hydrothermal circulation. Deep-cutting faults are conduits to transfer hot fluids to the surface. No high-temperature venting is observed at this stage.

### 3.4.4. Discussion

The preceding section shows that the sill intrusions are likely to trigger hydrothermal flow resulting in a highly complex temperature evolution. In order to further quantify the effects of hydrothermal flow on the thermal history of the Gjallar Ridge we use the conductive cooling scheme as a reference model and compare its calculated vitrinite reflectance to the convective scheme. For this, we store the predicted temperature field every 100 years throughout the 10,000 years of convection (or pure diffusion) simulations and subsequently calculate the vitrinite reflectance for the entire time evolution.

Figure 3-7a shows the calculated present-day vitrinite reflectance along the transect for the conduction scheme. In Figure 3-7b, vitrinite reflectance for the hydrothermal convection scenario is plotted and Figure 3-7c shows the differences between the two. In the diffusion only scenario (Figure 3-7a), only the sediments close to the sills are affected by hot intrusions due to contact metamorphism. Parallel sills act as a single thick sill and enhance the maturity of sediments in between to the maximum value. In the hydrothermal flow scenario (Figure 3-7b), the sediments above the sills are affected by hot ascending fluid up to 1 km, which indicates the importance of convection in spite of the limited thickness of the sills. Taking a closer look at the vitrinite reflectance in the convective scheme shows that the maturity associated with rising hydrothermal plumes above the sills is high at several regions, e.g. 3, 13 and 21 km distance, suggesting that the hot fluids spent more time discharging from this region and it elucidates possible long-term venting, especially driven by shallow sill complexes. Comparing the two schemes (Figure 3-7c), a narrow zone with less mature rocks with respect to the conductive scheme is revealed around the sill complexes. This phenomenon is explained by buoyancy effects which will be discussed later in this section. In the region between km 23 and

25 at depth of 4 km below present sea level, the hot fluids are trapped below an impermeable sill during their ascent. As a result, the maturity of rocks is substantially higher than surrounding rocks in this region. A similar effect is observed in other parts of the model (e.g. km 16.5 and 17.5) where a sill plays a cap-rock role over underlying counterparts.

The preceding paragraph has explored the first order effects of sill-driven hydrothermal flow on thermal maturity. For a more detailed discussion and to illustrate what likely fingerprints of hydrothermal flow should be found in well data from this area, we have created four pseudo-wells at distances of 2.2, 8.6, 12.8 and 23 km for further analysis. These sites were selected as typical examples of how recharge and discharge faults as well as hydrothermal plumes can affect maturity. Figure 3-8a, e, i and m illustrate the vitrinite reflectance derived from a scheme in which heat transfers only by conduction. Figure 3-8b, f, j and n show the vitrinite reflectance along the same profiles where also convection is present and accordingly, the differences between the two schemes are shown in Figure 3-8c, g, k and o. These results are calculated at present-day. Finally, a 1D temperature profile after 5000 years of simulation (approximately at the time of break-up) is shown in Figure 3-8d, h, l and p for the selected profiles.

In the first profile, i.e. at the distance of 2200 m, there exists only one single sill where two recharging faults cross the profile (see Figure 3-5). One of the faults turns out to be a discharge zone at later times while the other one remains recharging throughout the simulation. The major influence on vitrinite reflectance occurs at the sill located at 6500 m depth. First order observations from this profile show that the thermal aureole produced by metamorphism in the conductive scheme is thicker compared to the convective scheme. As a result, two peaks in maturity are observed above and below the sill by subtracting the vitrinite reflectance in the two schemes (Figure 3-8c), which is referred to as tapering effect in this paper. This feature can be explained by the fact that contact metamorphism causes a stable aureole around the sills where no fluid flow is present; whereas in the presence of convection, the rising hot fluids

rapidly cool the base of the sills. On the other side, convection generally starts above the sills and the plumes progress vigorously as heat pulses due to the strong thermal gradient between the sills and overlying sediments. This would lead to a smaller metamorphic aureole, but modeling indicates that finger-shaped anomalies would protrude as a result of long-term stable plumes. The thickness of the peaks produced as a result of such tapering reaches up to 400 m, showing that if convection is not accounted for, thicker zone below and above the sill intrusion is affected. This process is able to change the maturity level up to 0.4% Ro in the vicinity of sills (Figure 3-8c). Figure 3-8d shows that in the conduction scheme, the sill affects the upper and lower sediments up to 1000 m and the temperature profile shows a smooth curve, whereas in the convection scheme, the upper sediments are cooler than their initial temperature as a result of the transient nature of convection plumes. Although less sediments have apparently been affected by sill intrusion in the convective scheme in this specific profile, complex structure and anisotropic permeability are likely to change the path of hydrothermal fluids through the sediments above the sills.

Figure 3-8e and f show the result of maturity simulation for next pseudo-well at km 8.6. There exists a NE-SW recharge fault terminating at 5800 m depth which conducts the hot fluid originating from the underlying hydrothermal plume in convection scheme. In the conduction scheme however, only gentle effects of the sediments heating is observed. As a result, the difference between the conductive and convective schemes is a peak centered at 5700 m depth which coincides with an upwelling and changes the maturity level as considerable as 2.3% Ro. The difference between the convection and conduction schemes shows that overlying sediments are affected up to 500 m higher than conduction scheme. Moreover, a small drop in the difference between the two schemes observed at the depth of ~7 km (Figure 3-8g) is a result of the buoyant nature of hot fluids. Since parallel sills exist in this region, the heat transfer is conduction-dominated and convection only reduces the maturity level by as little as 0.2% Ro. The temperature profile in Figure 3-8h confirms the fact that in this region, adjacent sediments in the convection

scheme are cooler than in the conduction scheme. The low temperature in the recharging fault is observable at depth of ~5700 m.

Figure 3-8 i-k present results of calculating vitrinite reflectance for profile km 12.8. The upper portion of the profile, where hydrothermal activity is observed, is at the intersection of a major recharging fault and a group of tilted sills (see Figure 3-6c). The fault terminates nearly all the NE-SW faults and acts as a recharge zone in our model. At the depth of 4.3 km, corresponding to the apex of the present sill complex, the heat dissipates omni-directional in the conduction scheme and the surrounding sediments are affected by long-term heating; whereas in fluid flow cooling regime. The high thermal gradient present in this region makes the convection vigorous and episodic; therefore, as the convection plumes do not affect the sediments constantly for a sufficiently long time, the adjacent sediments in the convection scheme are less matured. The maximum difference in maturity level of the organic matter in the sediments in this region reaches up to 2.3% Ro. A significant recharging zone cooled the sediments from 4700 to 6700 m depth (Figure 3-8k and Figure 3-6c). The tapering effect is quite strong in the zone between 6 km and 7 km depth, despite the fact that the sills are laterally tens of meters away from the profile (Figure 3-8k). The evidence of ascending hot fluid at the vent-site is not observable in Figure 3-8l as the vigorous discharging fluids keep moving their pathways throughout the convection; however, upwelling is always present in this region (see Figure 3-6).

Finally, we take a look at profile km 23 where the second major hydrothermal activity is observed on the seismic transect. This region contains several sills buried in different depths. The hydrothermal plumes produced by sills between 7 and 8 km depth merged forming a thick hot zone as the sills are very close to each other. Since the sills are almost impermeable, the ascending plumes originated from this hot zone are trapped below the sills located at 5 km depth (see Figure 3-6). This fact can be seen in Figure 3-8p as there exists no recharge zone and the temperature profile in the convection scheme barely goes below the temperature before sill injection. In this region, the hot fluid increases

the temperature of sediments and therefore, it enhances the maturity up to 2% Ro just below the upper sills with respect to the conductive scheme. The upper part of profile, i.e. the region between 3.5 and 5 km depth, experiences tapering as the sills are shallow and therefore, strong convection rapidly cools down the sills; consequently, the difference in maturity level exceeds 2.5% Ro. The uppermost part of the profile does not show change in vitrinite reflectance as the upwelling keeps changing direction which can be observed during the simulation.

In the Gjallar Ridge area, two giant fluid pipes that reach the modern seafloor have been observed. These pipes are interpreted as hydrothermal vents that either have been active throughout 55 Ma or have been reactivated (Gay et al., 2012). As the presented simulation suggests, hydrothermal convection is relatively short-lived (<10ka) and therefore, continuous hydrothermal convection for millions of years can be ruled out as a possible origin of the observed pipe structures. These pipes could have also formed as a result of fluid migration due to recent tectonic activities. As discussed earlier, the impermeable sills may trap ascending hydrothermal fluids. Further faulting could, therefore, release the trapped fluid in the region where giant fluid pipes are observed.

Rapid climate change and major perturbation in carbon cycle at the time of break up (~56 Ma) is referred to as the Paleocene-Eocene Thermal Maximum (PETM). PETM caused massive extinction of marine species and sea level rise. The carbon was released throughout 20,000 years during which the global temperature increased by 5-8°C. Several hypothesis are proposed to explain the global temperature increase such as destabilization of methane clathrates, combustion of deposited peat and coal, release of thermogenic methane, drying epicontinental seas and permafrost (McInerney and Wing, 2011). Using Zircon dating in NE Atlantic, Svensen et al. (2010) suggested that organic-rich sediments affected by hot intrusions could be the source of greenhouse gas emission. Gu et al. (2011) suggested that under certain conditions of pressure and temperature, abundant methane hydrates could be a source of carbon during paleogene hydrothermal events. The presented simulations in this paper suggest

that hydrothermal fluid flow occurred at the time of break-up, can facilitate thermogenic methane release from the sediments buried at larger distances from the sill intrusions. As hydrothermal convection distributes heat into the sediments rapidly, it can, therefore, lead to rapid release of methane. The short time activity of hydrothermal circulations resulted from the presented simulation is consistent with this hypothesis.

In the presented simulations, we assumed that the sills are nearly impermeable, whereas the faults are prescribed to be highly permeable. As the initial injected magma is hotter than the cut-off temperature value (400-450°C (Morgan et al., 1987)), the assumption of impermeable sills is valid. As time progresses, the sills cool down and they may allow the convection through and therefore, the cooling process may be expedited. According to the results, hydrothermal convection is weak below the cut-off temperature and therefore, the associated thermal maturity is negligible. Besides, by rapid injection of hot magma, the adjacent rocks may react by thermal fracturing which results in more vigorous convection around the sills. This effect is more striking where sill complexes are injected simultaneously. Nevertheless, this effect is not accounted for in this study as more information is needed about the fracturing mechanism and therefore, should be included in future studies.

In case the faults are sealed by precipitations, they could inhibit convection and the underlying plumes may rather travel beneath the faults during their ascent. As fluid flow signatures have been observed above the major faults on the seismic data, we suggest that the faults have been permeable throughout the period of hydrothermal convection.

## Effects of sills on fluid flow and thermal maturity

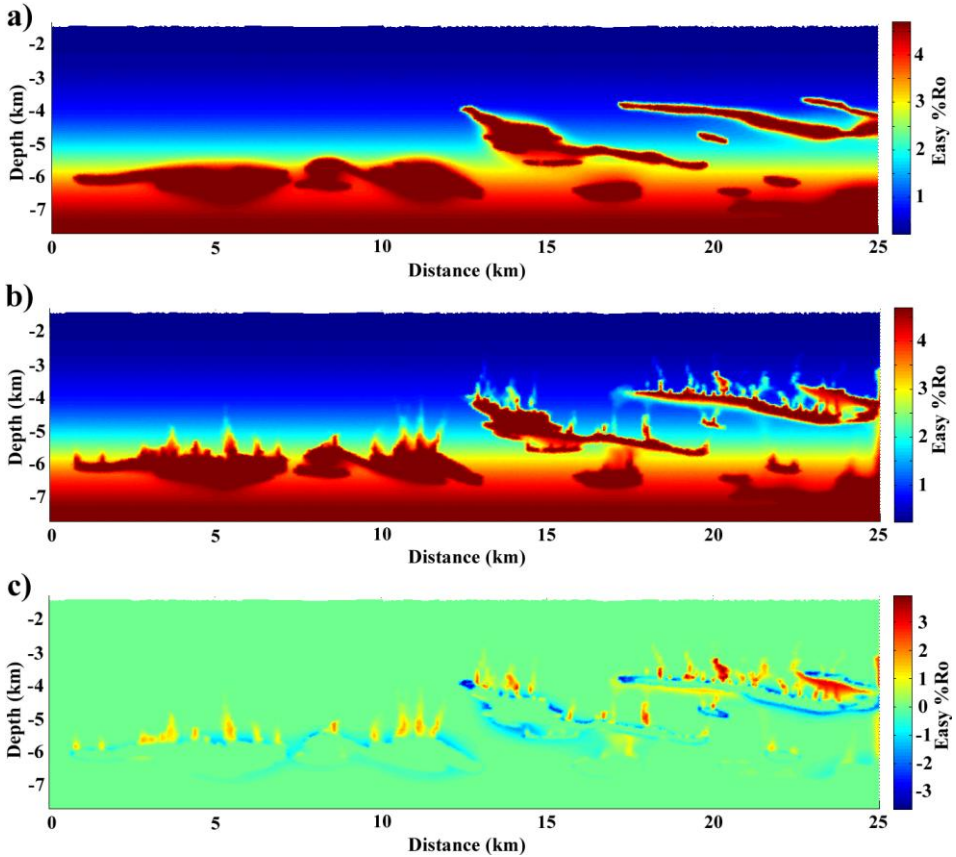


**Figure 3-7:** Vitrinite reflectance calculated for the transect. a) The scheme in which fluid convection is not accounted for. The parallel sills enhances the temperature of sediments in between and raised the maturity level to the maximum value. b) The scheme in which cooling is convection dominated. Several stable plumes at the top of sills enhanced the vitrinite reflectance. The plumes triggered by shallow sills suggest long-term venting. c) The difference in vitrinite reflectance between the two schemes. A narrow low mature zone is observed compared to the conduction scheme which is explained by buoyancy of fluids around the sills (see text). At several regions, the ascending fluids are trapped below the impermeable overlying sills resulting high maturity level of sediments.

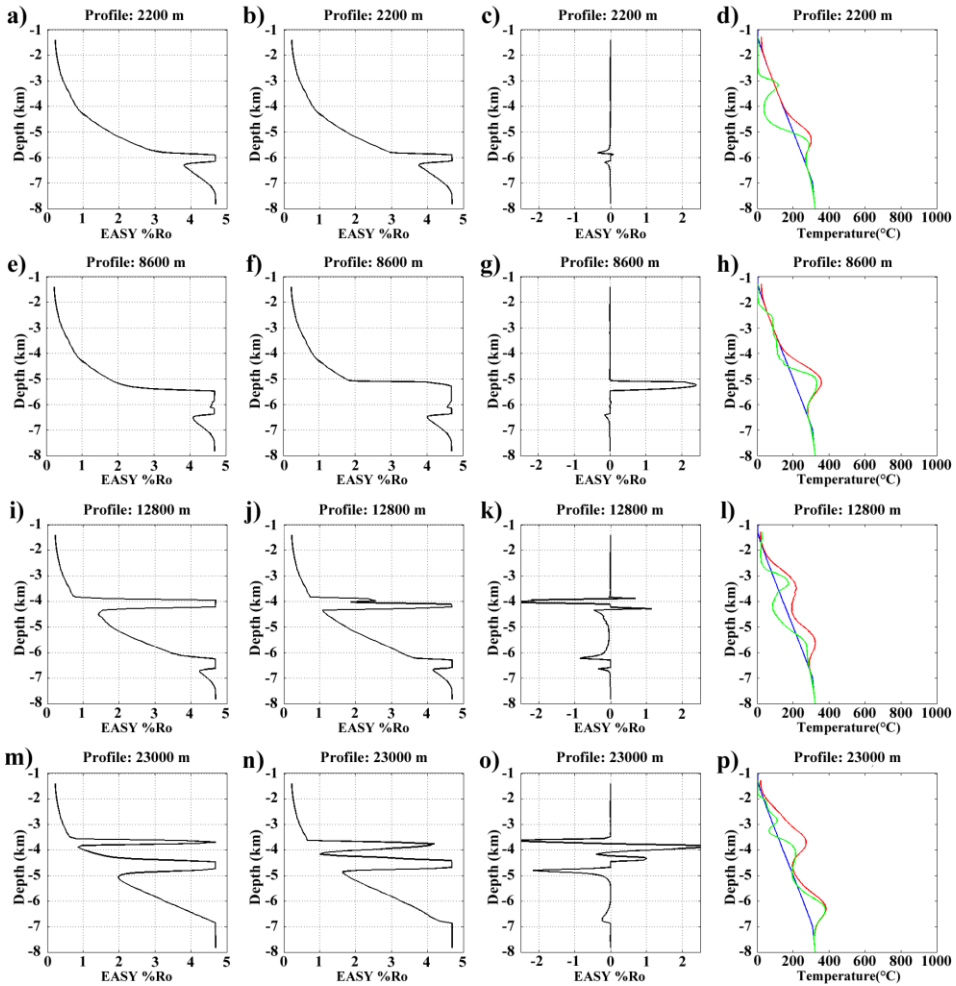


**Figure 3-8:** One dimensional vitrinite reflectance at profiles in the distances of 2.2, 8.6, 12.8 and 23 km. a, e, i, m) only conduction is responsible for cooling, b, f, j, n) the cooling is convection-driven, c, g, k, o) the difference between the Vitrinite reflectance in the two schemes and d, h, l, p) the temperatures of the profiles 5000 years of simulations. Blue lines represent the temperature when no intrusion exists, red and green lines show the temperature where conduction and where convection is responsible for cooling, respectively. Considering figs. a-d, two peaks are observed by comparing the two schemes which are explained by buoyancy of adjacent fluids (see text). In figs e-h, there exists a deep recharge fault which passes hot fluids along, however, in conduction scheme only smooth effects of sediment heating is observed, as a result a peak in vitrinite reflectance is observed in fig k. Figures i-k show the vitrinite reflectance where a hydrothermal field is detected. The upper portion of the profile is

intersection of a fault and apex of a tilted sill complex. Since convection is vigorous in this region, the change in vitrinite reflectance is as large as 2.5% Ro; and figs. m-p illustrate the effect of integrated sills where another hydrothermal field is detected. The trapped fluids below overlying sills result in large increase in the vitrinite reflectance by comparing to conduction scheme. The large differences between the two schemes in this profile suggest that conduction solely cannot explain the thermal history of the sediments.

### **3.5. Conclusion**

We have coupled a 1D basin reconstruction model with 2D simulations of sill-driven hydrothermal flow in order to reconstruct the thermal history of the Gjallar Ridge. The key conclusions of our study are:

- 1- Sill intrusions in the Gjallar Ridge area are likely to have triggered and driven hydrothermal flow at the time of their emplacement resulting in a highly complex thermal history.
- 2- These systems were relatively short-lived with high temperature venting occurring only within the first 1000 years after emplacement and convection terminating after approximately 10,000 years.
- 3- The imaged fault networks have largely controlled convection pathways although the two major hydrothermal vent-sites observed along the transect are mainly driven by shallow sill complexes where no faults are present.
- 4- Rapid hydrothermal cooling of sills reduces the volume of sediments that is affected by heat from magmatic sill intrusion. Hydrothermal plumes, however, enhance thermal maturation at greater distances from the sills.
- 5- Since the sills are nearly impermeable, rising hot hydrothermal fluids may pond underneath them thereby greatly enhancing thermal maturity. Future work should address hydrothermal flow along the fault networks in 3D, as flow along fault plains can unfortunately not be adequately addressed by our 2D setup.

## Chapter 4

# Solution strategies for modeling hydrothermal systems



# **Solution strategies for modeling hydrothermal systems**

## **4.1. Introduction**

Simulations of hydrothermal systems are gaining importance as a research tool for studying the physics of subsurface fluid flow. Modeling can be used to link and combine data sets from different fields of geosciences and can thereby help us to explain, for example, observations from vent sites or findings of laboratory experiments. A suitable hydrothermal model can make predictions on the pattern of convection and associated vent site locations, the composition of vent fluids, the venting temperature and lifetime of magmatic hydrothermal system. To make such predictions, models need to resolve equations of porous convection and be instructed by initial conditions, an equation of state for sea/pure water, and boundary conditions. Initial parameters can be obtained from geological, geophysical, geochemical and hydrological surveys. Further data from drilling can be used to refine the model parameters.

Dynamic behavior of sub-surface processes can be mathematically described by a set of coupled partial differential equations, which are highly non-linear due to their coefficients determined by an equation of state. Partial differential equations express the relationship between partial derivatives of the model variables with respect to the time and space domains. The partial

differential equations describing a hydrothermal system are adequately complex and boundary conditions are not simple enough to be solved analytically. Therefore, we need to utilize numerical methods instead. The advantage of using numerical simulations is that very complex linear and nonlinear equations can be solved by computer codes. In principle, a model should capture the physical processes of a system in accordance with the observations. Based on desired accuracy and computational efficiency, the resolution of computational domain can be defined (Ingebritsen et al., 2010).

Numerical models naturally make assumptions and have their limitations. Nevertheless, those are being continuously relaxed by using state-of-the-art computational methods and hardware. Two- and three-dimensional studies have already been carried out by taking single- and multi-phase regimes into account (e.g. Shin and Juric, 2002; Von Damm et al., 2003 ; Driesner and Geiger, 2007 and Coumou et al., 2009a). The relationship between temperature and pressure, deformation of rocks, fluid flow and chemical reactions are still challenging (e.g. Charlou et al., 2000; Von Damm et al., 2003; Tivey, 2007; Coumou et al., 2008a and Iyer et al., 2008). Nevertheless even the most accurate simulations have not considered all the realistic conditions in hydrothermal systems but acceptable solutions can still be achieved by defining appropriate boundary conditions (Ingebritsen et al., 2010).

Several numerical methods have already been used to solve partial differential equations in fluid flow simulations. Since several decades, Finite Difference Methods (FDM) are being used for approximating the solutions to partial differential equations (e.g. Aziz and Settari, 1979). In this method, the implementation is relatively easy but flexibility in the simulations is the main shortcoming. Highly heterogeneous and anisotropic media are better resolved by methods than can easily use unstructured meshes, such as FEM. Integrated Finite Difference Method (IFDM) was later introduced which combines integral formulation and finite difference gradients. This method is able to better represent heterogeneous media in any number of dimensions (Narasimhan and

Witherspoon, 1976). An alternative technique, which is used to resolve the equations more accurately over complex domains, is the Finite Element Method (FEM). Several studies have already employed this method to model heat transport and fluid flow (e.g. Zyvoloski et al., 1996). In this technique, the solution of partial differential equations (PDE) is approximated by simple functions over each finite element, while the misfit is being minimized in some average/integral sense. This method allows us to model geologically more complex structures compared to finite difference methods, thanks to flexibility in the fitting of unstructured meshes to any complex boundary (Matthäi, 2003 and Geiger et al., 2004). The finite element method was further developed in order to enable the modeling of discontinuous domains. Extended and Generalized Finite Element Methods (XFEM/GFEM) are utilized as useful techniques in space discretization and calculation of elastic cracks and dislocations (Belytschko et al., 2009).

Finite Volume Methods (FVM) are frequently used in conjunction with finite element methods (e.g. Geiger et al., 2004; Geiger et al., 2006 and Coumou et al., 2008b). In this method, finite volumes are superimposed on the elements in such a way that the finite element nodes constitute the volume centers and element centers together with midpoints on the element sides represent the corners of the volumes. In this method, flux entering a volume is equal to that leaving the neighboring volume and therefore, this method is highly flux-conservative. However, limited time-stepping leads to high calculation cost, which is the main disadvantage of this method. Nevertheless, some computational fluid dynamics (CFD) packages, such as FLUENT, Star-CD, CFX and ANSWER use this method due to its several advantages.

The partial differential equations describing hydrothermal flow are parabolic and hyperbolic in nature. Finite Element Methods are well-suited for solving parabolic equations such as pressure and temperature diffusion, whereas hyperbolic equations such as advection equations can be solved accurately either by FVM (Durlafsky, 1993) or by method of characteristics. Therefore,

many researchers recently tend to use hybrid approaches, in which the equations are decoupled by using explicit FVM together with implicit FEM. By decoupling the governing equations, we can solve each sub-equation by the best solution method. The downside of this approach is that small time steps are necessary to ensure stability and accuracy. In this chapter, the solution methods for FEM and FVM schemes as well as semi-Lagrangian methods are described in detail using the temperature equation as an example. In addition, different schemes for the solution of the temperature equation are presented and their pros and cons are discussed using both simplified and realistic simulations.

## 4.2. Modeling concepts

### 4.2.1. Hydrothermal flow equations

One main objective of this thesis is to develop a new 2D hydrothermal flow model that uses a combined FE- and FV-scheme in conjunction with unstructured meshes. In the following the governing equations of hydrothermal flow are presented before the employed FE-FV scheme is discussed.

If we assume that matrix porosity is constant, mass conservation in the single-phase state can be written in this form:

$$\phi \frac{\partial \rho_f}{\partial t} = -\nabla \cdot (\rho_f \vec{u}) \quad (4.1)$$

Where  $\rho_f$  is fluid density,  $\phi$  is matrix porosity and  $\vec{u}$  is fluid velocity which can be obtained from Darcy's law:

$$\vec{u} = -\frac{k}{\mu_f} (\nabla P - \rho_f \vec{g}) \quad (4.2)$$

Where  $k$  corresponds to matrix permeability,  $\mu_f$  to fluid viscosity,  $P$  to fluid pressure, and  $\vec{g}$  to the downward pointing acceleration of gravity.

To find an equation for fluid pressure, we substitute eqn.(4.2) into eqn.(4.1) and split fluid density into its pressure and temperature terms:

$$\phi\rho_f\beta_f\frac{\partial P}{\partial t} = \nabla \cdot \left[ \frac{k\rho_f}{\mu_f}(\nabla p - \rho_f\vec{g}) \right] + \phi\rho_f\alpha_f\frac{\partial T}{\partial t} \quad (4.3)$$

Where  $\alpha_f$  is the fluid's thermal expansion coefficient,  $\beta_f$  is isothermal compressibility and  $T$  is temperature. Finally, the energy conservation is given by:

$$\left( \phi\rho_f c_{pf} + (1-\phi)\rho_m c_{pm} \right) \frac{\partial T}{\partial t} = -\rho_f c_{pf} \vec{u} \cdot \nabla T + \nabla \cdot (\lambda \nabla T) \quad (4.4)$$

Where  $\lambda$  is thermal conductivity and  $c_p$  is specific heat capacity. Subscripts  $m$  and  $f$  denote matrix and fluid, respectively. The first term of the right hand side in eqn.(4.4) accounts for temperature advection and the second term for diffusion.

Under certain pressure-temperature conditions, fluids can undergo phase separation. The critical point of pure water occurs at a temperature and pressure of 375°C and 22 MPa, respectively. Above the critical point, the fluid is in supercritical condition and no distinction between the phases can be made, i.e. the fluids have properties between vapor and liquid. If the fluid is heated in such condition, its properties are constantly changed from liquid- to vapor-like. Below the critical point of water, the fluids are either in the single phase regime (vapor or liquid) or in the two-phase regime (boiling). Within the two-phase regime, the maximum temperature of water is constrained by its two-phase curve. Phase separation occurs when the energy in the system is increased further and as a result, both phases co-exist in the system. By further increasing the energy, only compressed steam exists in the system. Since the water depth and equivalently fluid pressure at most of the mid-ocean ridges are greater than the critical point of pure water, in the simulations of mid-ocean ridge

hydrothermal convection, it is usually assumed that the fluids are supercritical and therefore, no phase separation occurs. The temperature- and pressure-dependent fluid properties in the simulations conducted in this chapter are computed using PROST library (Bauer, 1998). The PROST library covers full range of temperature and pressure conditions present in the mid-ocean ridge setting. If the matrix is filled by seawater instead of pure water, the critical point of water shifts toward higher temperature and slightly higher pressure conditions (Geiger et al., 2006). The temperature and pressure extent over which phase separation occurs are substantially broadened and density contrast between the two phases becomes reduced (Driesner and Heinrich, 2007). Therefore, co-existence of the two-phases can be observed in a larger region beneath the seafloor. In addition, halite can be precipitated in NaCl-H<sub>2</sub>O systems under low-pressure and high-salinity conditions. This condition may lead to different rates of convection and conduction for salt and heat, resulting different flow pattern and introducing instabilities in convection (Geiger et al., 2006).

### **4.2.2. Model assumptions**

Comprehensive equations and boundary conditions for actual physical processes occurring within the Earth are excessively complicated and simulations capturing the full complexity of nature are still unachievable. Therefore, assumptions and simplifications are commonly used in numerical simulations of hydrothermal systems.

In this chapter, we assume that the matrix is homogeneous and no structural heterogeneities, i.e. faults and fractures, are present. Therefore, the fluid pathways are not affected by these structures. We further assume that the fluids are not turbulent and therefore, the fluid velocities obey Darcy's law. The rocks and fluids are in local thermal equilibrium. Although thermal conductivity generally decreases nonlinearly with increasing temperature of rocks, we assume a single effective bulk conductivity in the simulations for simplicity. This bulk conductivity is an average between rock strata and fluids present in

the system. It is also assumed that permeability is constant within the simulated domain and does not vary with depth, temperature or porosity. Moreover, alteration and fluid precipitation as well as thermal fracturing are not taken into account. As discussed earlier, the fluid is assumed single phase pure water and no chemical reactions occur between the fluids and the rocks.

### **4.2.3. Implementation**

The governing equations described in section 4.2.1 are solved using the Finite Element Method together with an advection scheme. The parabolic equations are solved using a modified version of the MATLAB based FEM solver MILAMIN by Dabrowski et.al (2008). The Galerkin method is used to obtain the weak form of the partial differential equations. We test two different advection schemes namely semi-Lagrangian and Finite Volume Method (FVM). The robustness of these methods is discussed by comparing the two in section 4.4.1. The governing equations are solved in a sequential order. For every time step, fluid properties are computed using pressure and temperature from previous time-step. Then, fluid pressure and Darcy velocities are calculated. Subsequently, the advection term in eqn.(4.4) is solved using the computed fluid velocities and finally the diffusion term of eqn.(4.4) is solved. We used linear shape functions for three-node triangular elements to map the nodes on integration points (see section 4.3.1 for details). Note that the Darcy velocities are calculated on the element centers by taking derivatives of fluid pressure.

## **4.3. Numerical discretization**

### **4.3.1. Finite Element Method**

Finite element method is a numerical procedure to find approximate solutions of Partial Differential Equations (PDE). In this technique, the modeling domain  $\Omega$  is divided into a number of finite regions called elements and over each element the solution is approximated by a simple function. The misfit between the approximate and exact solution is then minimized in an

average/integral sense over all elements. The mesh is created in such a way that there is no void between elements and therefore, every element has a number of neighbors. In the one-dimensional case, the domain is split into intervals (Figure 4-1), whereas in the two-dimensional case, the elements are generally either triangular or quadrilateral. These types of elements are common as integration over these simple shapes is relatively straightforward. Each element possesses a number of points called nodes and it is usually tried to estimate function values on such discrete coordinates. Indeed, quadrilateral elements are inferior to triangular elements in terms of accuracy and flexibility of the computational mesh where the PDE is to be solved on. Triangular unstructured meshes are commonly used due to its flexibility to cover structurally complex domains (Figure 4-2).

By choosing sufficiently small elements, the quantities of interest can be obtained by solving PDEs in each element using *so-called* shape function (also called ansatz function). The shape function interpolates the values of discrete solutions between the nodes for each arbitrary point inside an element – or said differently, the exact solution is approximated over the element by these relatively simple functions over the element. To describe the finite element solution for partial differential equations, we take the steady state thermal diffusion equation as an example:

$$\frac{\partial}{\partial \hat{x}} \lambda \frac{\partial T(\hat{x})}{\partial \hat{x}} = 0, \quad \hat{x} \in \{x, y\} \quad (4.5)$$

where  $T$  is the unknown temperature at the element nodes. The approximated value for the temperature is given by:

$$\tilde{T}(\hat{x}) = \sum_{j=1}^{nnode} T_j N_j(\hat{x}) = T_j N_j, \quad \hat{x} \in \{x, y\} \quad (4.6)$$

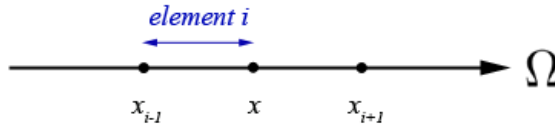


**Figure 4-1:** One dimensional finite elements.

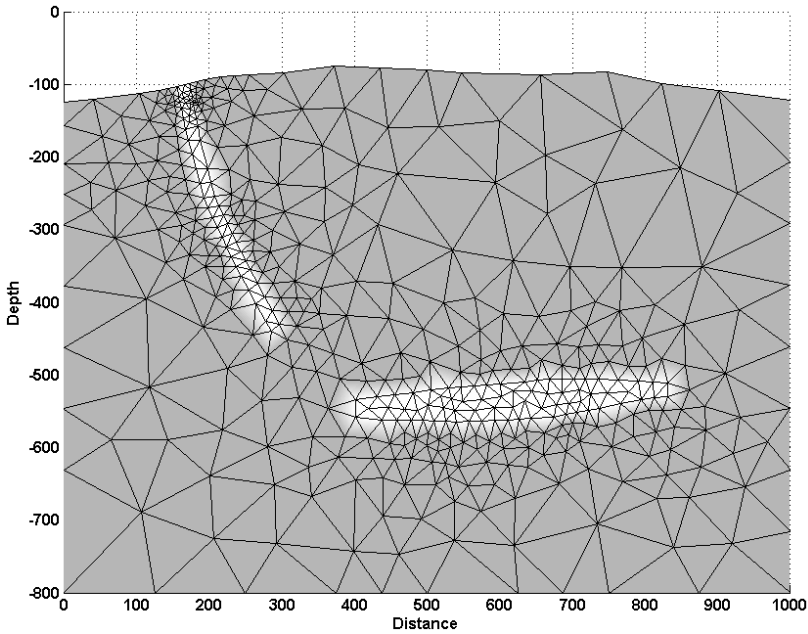


**Figure 4-2:** Two dimensional unstructured finite element mesh.

where  $N_j$  are the shape functions that approximate the solution and  $T_j$  are the unknown parameters (i.e. nodal temperatures),  $n_{nod}$  is the number of nodes. Note that the Einstein convention is used so that a summation is assumed over repeated indices. In the FEM, shape functions are chosen that have a value of 1 on the grid point  $j$  and 0 on the other grid points, so that the coefficients that are

optimized during the solution processes are directly the unknowns at the nodes, i.e. temperature in this example. Therefore, the following constrain must be satisfied:

$$\sum_{j=1}^{mod} N_j(\hat{x}) = 1, \quad \hat{x} \in \{x, y\} \quad (4.7)$$

Two types of shape functions are commonly used for 2D triangular elements according to the resolution and accuracy of interest: Lagrange linear shape function for three-node elements and Lagrange quadratic shape function for six-node elements. Also cubic shape functions are used in finite element method to achieve higher accuracy, but it is not common in fluid flow simulations. If higher-order shape functions are used, nodes are located on the intersection of elements as well as on the midpoints of the sides (and on the center of elements in seven-node elements). There are two methods to improve the accuracy of modeling: either use of a higher number of elements and linear shape function (h-adaptivity), or use of less number of elements and quadratic shape function (p-adaptivity). The latter suffers computational time drawback, especially in three dimensional modeling or in large domains due to higher number of nodes. In spite of higher accuracy of solution using quadratic shape functions, commonly linear shape functions in presence of more elements are used due to simplicity in implementation and performance of computations. This means that  $T_j$  is a linear function on each element and continuous over domain  $\Omega$ . Some commercial codes employ p-adaptivity scheme in a coarse mesh and the solution is then interpolated on a fine mesh in order to reach the convergence and numerical stability (Tu et al., 2008).

In a two-dimensional domain with three-node triangular elements, the global coordinates are transferred to local ones as shown in Figure 4-3. The bilinear shape functions, therefore, can be defined by:

$$\begin{aligned}
 N_1(\zeta, \eta) &= 1 - \zeta - \eta \\
 N_2(\zeta, \eta) &= \zeta \\
 N_3(\zeta, \eta) &= \eta
 \end{aligned}
 \tag{4.8}$$

Where  $\xi$  and  $\eta$  are two local coordinates. The shape functions are plotted in Figure 4-4. The solution within an element is thus given by:

$$NT = [N_1 \quad N_2 \quad N_3] \begin{bmatrix} T_1 \\ T_2 \\ T_3 \end{bmatrix}
 \tag{4.9}$$

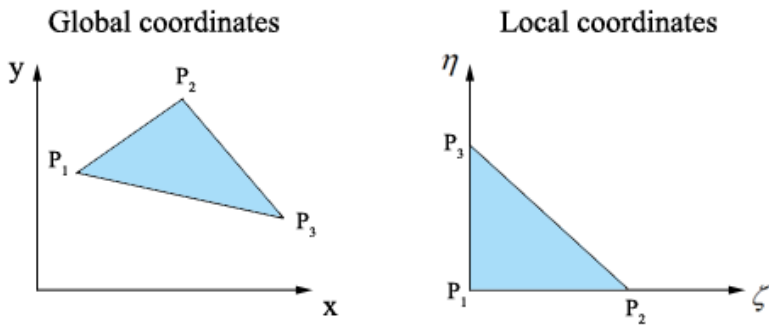


Figure 4-3: Global and local coordinates of elements.

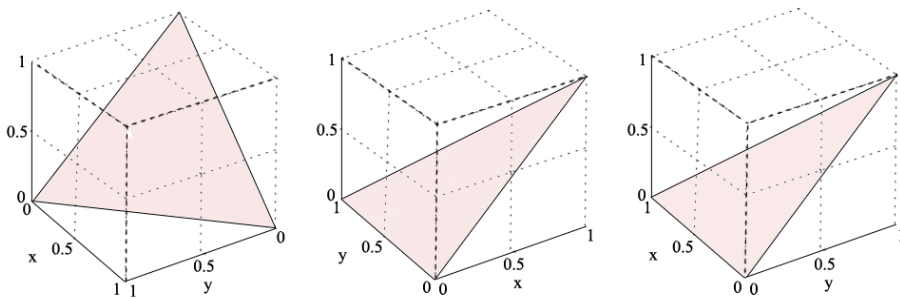


Figure 4-4: Bilinear shape functions for triangular element.

Substituting the approximated value of unknown  $T$  in the PDE, an error or residual  $R_s$  appears as a result of discrepancy between the exact and approximated temperature:

$$\frac{\mathcal{L}(\tilde{T}(\hat{x}))}{\mathcal{L}(\hat{x})} - R_s \neq 0, \quad \hat{x} \in \{x, y\} \quad (4.10)$$

To find a suitable approximation  $\tilde{T}$  for  $T$ , we need to minimize the residual. One of the methods which are commonly used to achieve this goal in the domain is called Weighted Residual Method (WRM). The basic idea is to force the residual towards zero in some weighted average way:

$$\int_{\Omega} \left( w_i(\hat{x}) \frac{\partial}{\partial \hat{x}} \lambda \frac{\partial \tilde{T}(\hat{x})}{\partial \hat{x}} \right) d\Omega = 0, \quad i = 1, 2, \dots, n_{nod} \quad (4.11)$$

where the number of weight functions ( $w_i$ ) is the same as unknowns  $T$ . The weighted residuals can be obtained by different sub-methods such as collocation method (e.g. Syam and Attili, 2006), sub-domain method (e.g. Segerlind, 1989), least square method (e.g. Choi, 2011), method of moments (e.g. Finlayson and Scriven, 1965) and Galerkin's method (e.g. Iqbal, 2011), which differ in the choice of weighting functions. If the weighting functions are the same as shape functions, this technique is called Galerkin's method (Polycarpou, 2006). This method is the most common technique to minimize the residuals and find the unknowns in the finite element method.

Integration by parts is commonly used in the integral formulation of partial differential equations. In two-dimensional domain, integration by parts represents gradient and divergence theorems. The integration by parts is used to distribute differentiation equivalently on both unknowns and weight functions as well as to use boundary conditions (Polycarpou, 2006). Using the integration by parts and Galerkin's method, the eqn. (4.11) yields:

$$\begin{aligned}
 \int_{\Omega} N_i \frac{\partial}{\partial \hat{x}} \lambda \frac{\partial N_j}{\partial \hat{x}} T_j(\hat{x}) d\Omega = - \int_{\Omega} \frac{\partial N_i}{\partial \hat{x}} \lambda \frac{\partial N_j}{\partial \hat{x}} T_j(\hat{x}) \Omega \\
 + \oint_{\Gamma} N_i \lambda \frac{\partial N_j}{\partial \hat{x}} T_j(\hat{x}) d\Gamma, \quad i = 1, 2, \dots, nnod
 \end{aligned} \tag{4.12}$$

The line integral on the right-hand side of the equation represents a flux boundary condition – for simplicity it is neglected in the remainder of this discussion. The weak form of the problem can now be written as:

$$\int_{\Omega} \frac{\partial N_i}{\partial \hat{x}} \lambda \frac{\partial N_j}{\partial \hat{x}} T_j(\hat{x}) \Omega = \sum_{nel} \int_{\Omega_{el}} \frac{\partial N_i}{\partial \hat{x}} \lambda \frac{\partial N_j}{\partial \hat{x}} T_j(\hat{x}) \Omega_{el} \tag{4.13}$$

The equation must be integrated over each element and the final stiffness or coefficient matrix is obtained by summation over all integrals/elements. On unstructured meshes, it is usually not possible to evaluate the integral analytically so that numerical methods such as Gauss-Legendre quadrature are used. This method obtains the best estimation of a definite integral of a function by weighting the values of functions at specific points. These numerical integration schemes are all defined for a *so-called* master element with local coordinates ranging [-1,1]:

$$\int_{-1}^1 \int_{-1}^1 f(\xi, \eta) d\xi d\eta \approx \sum_{i=1}^{nip} \omega_i f(\xi_i, \eta_i) \tag{4.14}$$

where  $nip$  is the number of integration points and  $\omega_i$  is integration weight function at integration point  $i$ . The coordinate transformation is only done for easier numerical integration and can be achieved via the (inverse) Jacobian matrix,  $J$ :

$$\begin{Bmatrix} \frac{\partial N(\xi, \eta)}{\partial x} \\ \frac{\partial N(\xi, \eta)}{\partial y} \end{Bmatrix} = [J^{-1}] \begin{Bmatrix} \frac{\partial N(\xi, \eta)}{\partial \xi} \\ \frac{\partial N(\xi, \eta)}{\partial \eta} \end{Bmatrix} \quad (4.15)$$

The change in domain size during the integration is obtained from the determinant of the Jacobian matrix:

$$d\Omega_e = dx dy = \det(J) d\xi d\eta \quad (4.16)$$

The weak form of each element can be written as:

$$\sum_{ip=1}^{nip} \frac{\partial N_i(\xi_{ip}, \eta_{ip})}{\partial \hat{x}} \lambda \frac{\partial N_j(\xi_{ip}, \eta_{ip})}{\partial \hat{x}} T_j(\hat{x}) \omega_i \det(J) = 0 \quad (4.17)$$

which can be written in matrix form as:

$$[\kappa_{el}] \{T_{el}\} = \{\nu_{el}\} \quad (4.18)$$

where  $[\kappa_{el}]$  is a square matrix,  $\{T_{el}\}$  is a vector with the unknown nodal temperatures, and  $\{\nu\}$  is called the force vector (which is zero in this example). After constructing a single finite element solution, we are able to develop the global form of the equation:

$$[\mathbf{K}] \{T\} = \{\nu\} \quad (4.19)$$

where  $[\mathbf{K}]$  denotes to global assemblage matrix, also known as element global stiffness matrix,  $\{T\}$  is the vector of unknowns for all the nodes and  $\{\nu\}$  is the vector of nodal applied forces. As an example for a one dimensional domain containing linear two-node elements, we can write the equations

separately for each finite element and assemble the stiffness matrix. The global form of equation can be written as:

$$\begin{bmatrix}
 \kappa_{11}^1 & \kappa_{12}^1 & 0 & 0 & 0 \\
 \kappa_{21}^1 & (\kappa_{22}^1 + \kappa_{11}^2) & \kappa_{11} & 0 & 0 \\
 0 & k_{11} & (\kappa_{22}^2 + \kappa_{11}^3) & \kappa_{12} & 0 \\
 \dots & \dots & \dots & \dots & \dots \\
 0 & 0 & \kappa_{21} & (\kappa_{22}^{n-1} + \kappa_{11}^n) & \kappa_{12}^n \\
 0 & 0 & 0 & \kappa_{21}^n & \kappa_{22}^n
 \end{bmatrix}
 \begin{Bmatrix}
 T_1 \\
 T_2 \\
 T_3 \\
 \dots \\
 T_n \\
 T_{n+1}
 \end{Bmatrix}
 =
 \begin{Bmatrix}
 u_1^1 \\
 u_2^1 + u_1^2 \\
 u_2^2 + u_1^3 \\
 \dots \\
 u_2^{n-1} + u_1^n \\
 u_1^n
 \end{Bmatrix}
 \quad (4.20)$$

To solve the set of equations (4.20) and find the unknowns  $T_j$ , iterative and direct methods are used. Iterative methods start with an initial guess for temperature and perform a sequence of algebraic operations to improve it (Canga and Becker, 1999). Direct methods lead directly to a solution to the system of equations (Habashi et al., 1991).

If a triangular element has only one degree of freedom for each node, the size of element stiffness matrix is  $3 \times 3$ . The components of the matrix are the stiffness between one node to the adjacent node or to itself. Since the stiffness matrix for the entire domain is generally too large in size, the computational cost is increased substantially; however, as the matrix is symmetric, positive definite, considerably sparse (since most of the entries are zero) and the data are concentrated close to the main diagonal, it is possible to compress the matrix using a number of computational techniques. In other words, we can calculate the contribution of each element to the stiffness matrix and then constitute these contributions.

In short, the finite element method starts from converting the partial differential equations into a weak formulation. Then, using an appropriate element type according to the geological complexity of the region of interest, the domain is divided to a number of finite regions. The shape function is then chosen based on the size of domain as well as the order of accuracy of interest. Using an integration over all the elements and discretize it by Galerkin's method, we achieve a set of equations and unknowns. The integration for each element is performed in local coordinates and then transferred to the global coordinates by the *so-called* Jacobian matrix. Finally, the global stiffness matrix as well as global force vector is formed and subsequently, the eqn. (4.20) is solved by a matrix division to find the unknown parameters.

Recently, Dabrowski et al. (2008) has introduced a computational method to solve the partial differential equations efficiently and quickly in two dimensions by MATLAB. In this technique, the standard FEM algorithm is optimized by dividing the computational domain into several groups of elements and solving for each group separately. This method enhances the performance of matrix solver by fast matrix assembly and efficient processing and enables solving large matrices; therefore, this method allows higher resolution of solution domain in a relatively short time.

### 4.3.2. Finite Volume Method

The Finite Volume Method (FVM) is another numerical discretization, which is one of the most suitable platforms to solve transport problems (e.g. Geiger et al., 2004; Geiger et al., 2006 and Coumou et al., 2008b). The finite volume mesh can be constructed on the basis of finite element method in a different mesh configuration, in that the domain is subdivided to a finite number of continuous and non-overlapping control volumes:

$$\Pi_i = \bigcup_{i=1}^N \Pi_i, \quad \Pi_i \cap \Pi_j = 0, \quad \forall i \neq j \quad (4.21)$$

Where  $\Pi$  is a control volume, subscripts  $i$ ,  $j$  and  $t$  are indexes for two adjacent volumes and total domain volume, respectively, and  $N$  is the number of volumes. In a one-dimensional simulation, the volume is the region between element centers (Figure 4-5); whereas in two dimensional simulations, finite element nodes are volume centers and element centers together with the centers in each side of the elements constitute the volume boundaries. The results are closed polygon control volumes, which cover the entire domain (Figure 4-6). Since the finite elements are able to resolve highly heterogeneous structures, finite volumes can also cover every arbitrary shape within the computational domain.

In this method, the divergence term in the transport equations is rewritten as surface integrals based on the divergence theorem. Then, fluxes normal to the volume segments are evaluated. The flux integration along each control volume resolves for a local balance equation. The integration over all the balance equations subsequently resolves the system. Since this method deals with the fluxes along the segments of the volumes, this method is highly conservative. It means that everything comes from a particular volume, enters into adjacent volume; however, appropriate boundary conditions must be applied.

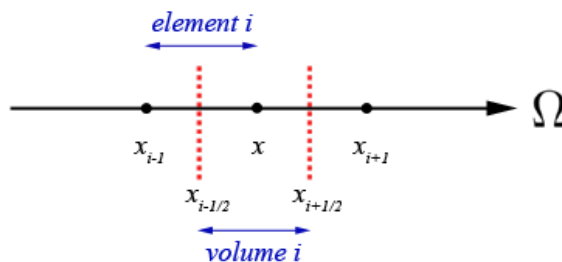


**Figure 4-5:** One-dimensional finite volumes.

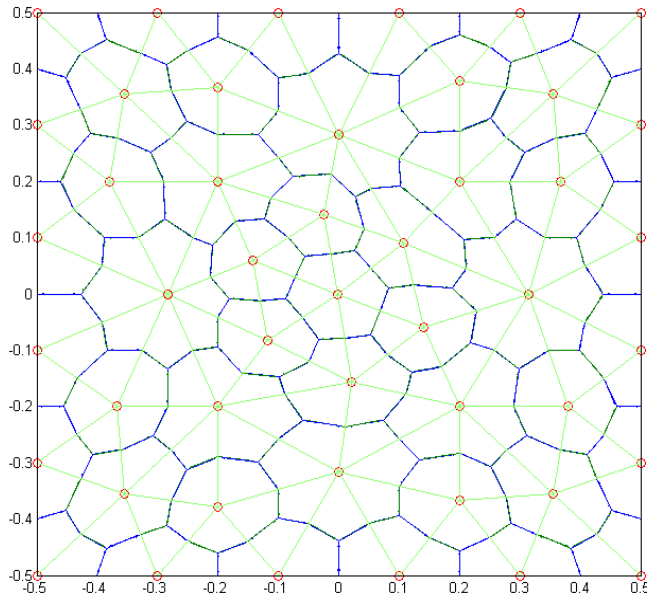


**Figure 4-6:** Two-dimensional unstructured finite volume mesh.

As discussed earlier, the advection part of temperature equation is solved either by FVM or by Semi-Lagrangian method. In this section, the FVM solution for the advection equation is explained in detail. The solution by semi-Lagrangian method comes in the next section. The temperature advection equation can be written as:

$$\frac{\partial T}{\partial t} = -\vec{u}^* \cdot \nabla \hat{T} \quad (4.22)$$

where  $\hat{T}$  is the temperature obtained from diffusion solution and the scaled velocities are defined by:

$$\bar{u}^* = \frac{\rho_f c_{pf}}{(1-\phi)\rho_m c_{pm} + \phi\rho_f c_{pf}} \bar{u} \quad (4.23)$$

The eqn. (4.22) could be rewritten as:

$$\frac{\partial T}{\partial t} = -\nabla \cdot (\bar{u}^* \hat{T}) + \hat{T} \nabla \cdot (\bar{u}^*) \quad (4.24)$$

Both terms of right hand side are solved using FVM. For simplicity, we here only describe the solution to the first term on the right-hand side. By integrating eqn. (4.24) over finite volume  $\Pi$  at node  $i$ :

$$\int_{\Pi_i} \frac{\partial T}{\partial t} dS_i = - \int_{\Pi_i} \nabla \cdot (\bar{u}^* \hat{T}) dS_i \quad (4.25)$$

The velocities are calculated at the center of elements; therefore, they are continuous along the volume boundaries. Using Green's theorem, we can approximate the right hand side integral in eqn. (4.25) over the faces of control volume:

$$r_i \frac{\partial T_i}{\partial t} = - \oint_{x_i} \bar{u}^* \hat{T} \cdot \bar{n} dX \quad (4.26)$$

where  $\bar{n}$  is outward-pointing unit normal to the segment and  $r_i$  is the area of the control volume  $i$ . By discretizing the eqn. (4.26) using Euler method, the temperature value will be obtained:

$$T_i = \hat{T}_i - \frac{\Delta t}{r_i} \sum_j^{N_i} L_j \bar{u}_j^* \hat{T}_j \cdot \bar{n}_j \quad (4.27)$$

where  $L_j$  is the respective length of the segment  $j$  and  $N_i$  denotes the number of segments in the control volume  $i$ . The flux term over the finite volume  $i$  is computed using fluid velocities from previous time step. The value  $\hat{T}_j$  in the flux term is obtained from the upwind finite volume at the segment  $j$ . For many problems, a slight dispersion (artificially broadened temperature fronts (Geiger et al., 2006)) in the result is not important, but care must be taken if such dispersions produce small negative values.

The first-order accurate solution for equation (4.27) leads to highly diffusive non-physical results; therefore, we need to apply a second order accuracy in space on the solution (Geiger et al., 2004). To achieve this goal, a plane is fitted through the quantity  $T_i$  at the volume of interest and the quantities of  $T_j$  at the adjacent volumes using least square method. In two dimensions, the gradient meets the following condition:

$$\sum_{l=1}^2 M_{kl} a_l = b_k \quad (4.28)$$

where

$$M_{kl} = \sum_{j=1}^n (x_{jk} - x_{ik})(x_{jl} - x_{il}) \quad (4.29)$$

and

$$b_k = \sum_{j=1}^n (T_j - T_i)(x_{jk} - x_{ik}) \quad (4.30)$$

where  $x$  is the spatial coordinates for center of volume of interest and adjacent volumes and  $n$  is the number of neighboring finite volumes. Therefore, the linear approximation for  $T_i$  anywhere in the volume is given by:

$$\tilde{T}_i = T_i + \bar{a}_i(x - x_i), \quad x \in \Pi_i \quad (4.31)$$

In order to avoid spurious oscillations during the finite volume simulation caused by the approximation in the eqn.(4.31), a slope limiter should be applied to smooth the gradient of  $T_i$ . Therefore, the second term in the eqn. (4.31) should be limited by a coefficient  $\delta_i$  which varies between 0 and 1:

$$\tilde{T}_i = T_i + \delta_i \bar{a}_i(x - x_i), \quad \delta_i \in (0,1) \quad (4.32)$$

When the coefficient  $\delta_i = 0$ , the result will be in first-order accuracy, whereas  $\delta_i = 1$  results in second-order accuracy. To find the value of  $\delta_i$ , we need to apply a MINMOD limiter technique:

$$\delta_i = \min(B_i, 1) \quad (4.33)$$

where

$$B_i = \begin{cases} (T_i^{\max} - T_i) / (\tilde{T}_j - T_i) & \tilde{T}_j > T_i \\ (T_i^{\min} - T_i) / (\tilde{T}_j - T_i) & \tilde{T}_j < T_i \\ 1 & \tilde{T}_j = T_i \end{cases} \quad (4.34)$$

where  $T_i^{\max}$  and  $T_i^{\min}$  are maximum and minimum values of  $T_i$ , respectively.

The equations are solved in an iterative procedure where the time step is explicit and limited by the *so-called* Courant Friedrich Levy (CFL) condition. The CFL condition is a necessary criterion which is applied to ascertain the stability of solution by FVM. If  $\tau_i$  is the mean radius of a control volume  $i$ , and

$\bar{u}_{\max}$  is the maximum velocity in the elements contributing in the control volume  $i$ , the CFL condition in the simplest form is given by:

$$\Delta t_{CFL} = \left( \frac{\tau_i}{\bar{u}_{\max}} \right)_{\min} \quad (4.35)$$

### 4.3.3. Semi-Lagrangian

An alternative way for solving transport problems is the method of characteristics, or Semi-Lagrange method (SLM). The reason to use this method is to be able to use larger time-steps while the solution is still stable and accurate. The basic idea of the scheme is that a conserved quantity does not change along a flow line. In the SLM backtracking along flow lines occurs in order to solve advection problems. Figure 4-7 shows a 1D regular grid of nodes where a specific particle moves through the matrix.

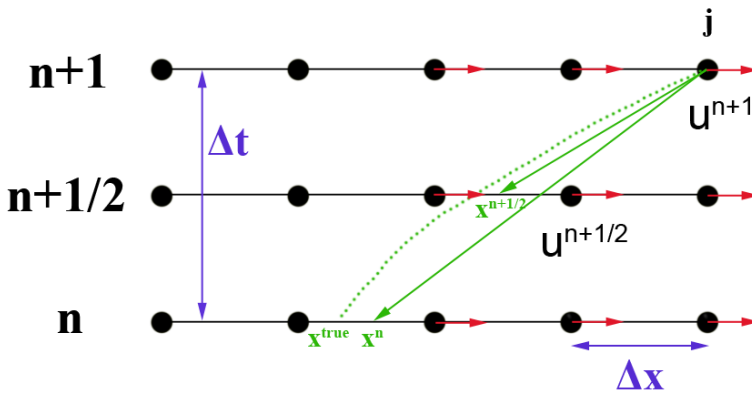


**Figure 4-7:** schematic model for semi-Lagrangian advection method.

In this method, temperature should be conserved during one time-step. Since it is possible to move backward in time while the solution is stable in

transport equations, we start at the new point in time step  $\mathbf{n}+1$  and move backward in time to find the point at time step  $\mathbf{n}$ , instead of taking a guess for the point in time step  $\mathbf{n}$  and move it forward. In other words, we find a particle in time step  $\mathbf{n}$  which passes through a grid point at time step  $\mathbf{n}+1$  (point  $\mathbf{j}$ ) by tracking the position of particle. A common scheme to do so is mid-point scheme: using the velocity at time step  $\mathbf{n}+1$ , we find the location of particle at half time step back (time step  $\mathbf{n}+1/2$ ). The coordinate of particle will be:

$$x^{n+1/2} = x^{n+1} - \frac{u^{n+1} \Delta t}{2\Delta x} \quad (4.36)$$

Then using an interpolation scheme we find the velocities at time step  $\mathbf{n}+1/2$ . Using the velocity at half time step back, we move full time step back and find the location at time step  $\mathbf{n}$ , where the particle has come from:

$$x^n = x^{n+1} - \frac{u^{n+1/2} \Delta t}{\Delta x} \quad (4.37)$$

And since the actual characteristics follow the dashed line and the actual location of particle at time step  $\mathbf{n}$  is  $x^{true}$ , we use an interpolation scheme to find the value of particle  $T$  at  $x^n$ . In fluid flow problem, this method is especially useful in single-phase fluid transport where boiling effects are not taken into account.

## 4.4. Solution methods

### 4.4.1. Advection schemes

The partial differential equation for thermal advection is hyperbolic and can be solved by a number of schemes. The concept and formulation of two common advection schemes, i.e. Semi-Lagrangian and Finite Volume Method

(FVM), are explained in detail in sections 4.3.2 and 4.3.3. This section aims at addressing a few simple simulations to point out the advantages and disadvantages of the two schemes. The models used in this section are set up by a simple localized heat source in a unique coordinate system rotating inside the medium where all the boundaries are permeable and diabatic. In this analysis, we quantify the total energy stored in the system in both schemes of semi-Lagrangian and FVM, where all the fluid properties are set to 1 for simplicity. The fluid velocities are initialized as functions of the nodal coordinates:

$$\left\{ \begin{array}{l} \bar{u}_x = -\sin\left(\pi\left(x + \frac{X}{2}\right)\right) \times \cos\left(\pi\left(y + \frac{Y}{2}\right)\right) \\ \bar{u}_y = \cos\left(\pi\left(x + \frac{X}{2}\right)\right) \times \sin\left(\pi\left(y + \frac{Y}{2}\right)\right) \end{array} \right. , X, Y \in [-0.5, 0.5] \quad (4.38)$$

where  $x$  and  $y$  are coordinates of the nodes and  $X$  and  $Y$  are coordinates of domain boundaries. The heat source is defined using the following spatial relation:

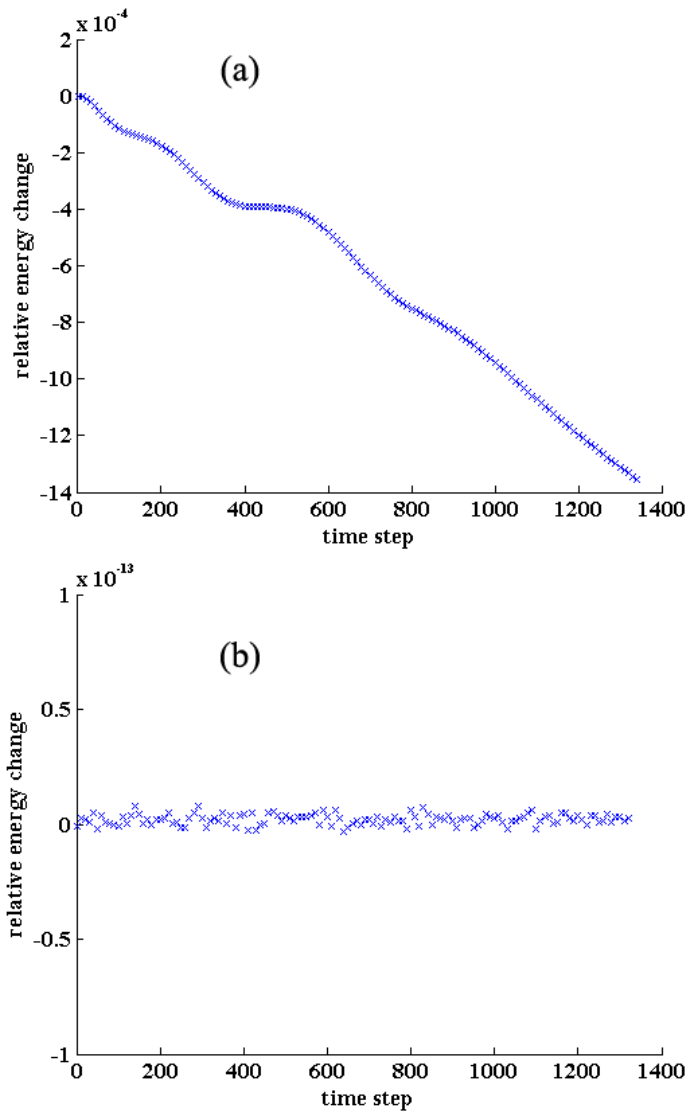
$$T = 1 + 2 \exp\left(\frac{-((x + x_s)^2 + y^2)}{l^2}\right) \quad (4.39)$$

where  $x_s$  is an initial lateral shift applied to the center of heat source with respect to domain center which is set to 0.25 in the simulations and  $l$  is localization factor set to 0.07. A total number of 17,000 elements are used in the model to minimize possible numerical dispersion associated with the resolution. Figure 4-8 shows the total energy stored in the system after each time step. The simulation of heat transfer by semi-Lagrangian method using linear shape functions shows that total energy in the system decreases rapidly as time progresses (Figure 4-8 a). Similar model conducted by finite volume method is shown in Figure 4-8 b. In this model, the variation in total energy in the system

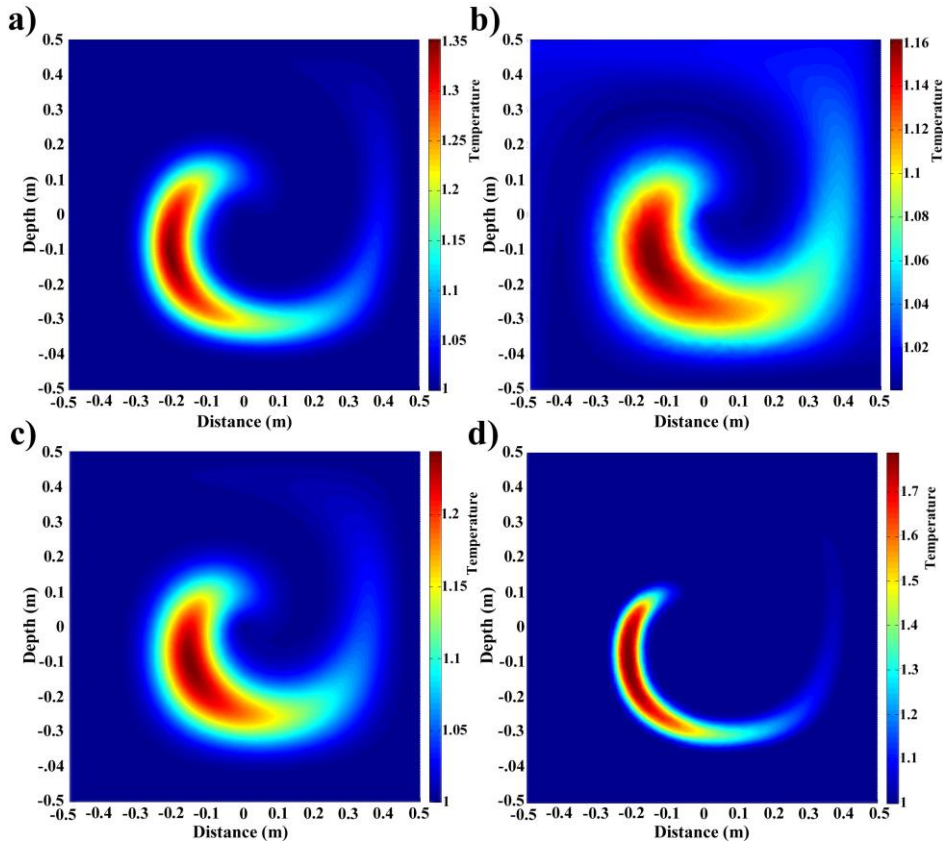
is  $\sim 10$  orders of magnitude less than that of semi-Lagrangian, pointing to the fact that the FVM is perfectly conservative.

Figure 4-9 shows the results of a spinning heat source around the center after one complete cycle solved by different schemes. In Figure 4-9 a, the simulation is performed by semi-Lagrangian scheme. In this case, the time-step is defined at the way that fluid particles are not allowed to move more than 0.05 of the element size at each time-step by given velocities. In the following, we address this time-stepping by SL criterion. Figure 4-9 b exhibits the same simulation with semi-Lagrangian method, but the time step definition meets the CFL criterion (see section 4.3.2) instead, resulting considerably smaller time steps compared to SL criterion. Figure 4-9 c shows the solution by FVM using first order accuracy (see section 4.3.2), where CFL criterion is applied for time stepping. Finally, Figure 4-9 d shows simulation result of advection by FVM using second order accuracy and CFL criterion. The solution by FVM using second order accuracy, apparently better resolves the heat advection due to its mass conserving attribute. By comparing the simulations conducted by semi-Lagrangian scheme (Figure 4-9 a and b), it is shown that choosing an appropriate time step reduces numerical dispersion and the model does not produce an unrealistic result. In this particular analysis, the time step calculated for semi-Lagrangian method is approximately one order of magnitude larger than that of FVM. Now, if we compare the solutions by semi-Lagrangian and FVM (first order accuracy) at similar time-stepping (Figure 4-9 b and c), we clearly see that FVM resolves the fluid advection with less dispersion. The second-order accuracy in the FVM, however, exhibit more localized heat transport by comparing the maximum temperature present in the matrix. A remarkable finding based on these results is that the advection scheme using semi-Lagrangian and SL criterion (Figure 4-9 a) for time stepping apparently confronts less dispersion compared to FVM solution in first order accuracy and CFL criterion (Figure 4-9 c). This result suggests that the simulations should be performed either by FVM using second-order accuracy or by semi-Lagrangian using SL criterion, i.e. both solution method and time-stepping contribute in the

accuracy of the results. The main drawback for FVM is its time stepping limitation, as taking large time steps result in non-physical solutions. This obstacle will be faded away by employing future fast computers.



**Figure 4-8:** Total energy stored in the matrix. a) Semi-Lagrangian method b) Finite Volume Method. Note that the vertical axis is scaled.



**Figure 4-9:** Synthetic model of spinning heat source through porous matrix. a) Semi-Lagrangian scheme, where time-step is restricted to the element size and fluid particle velocities (LS time-stepping), b) Semi-Lagrangian scheme with CFL criterion for time-stepping, c) Finite volume method (first order accuracy), where time step meets the CFL criterion and d) Finite volume method (second order accuracy), using CFL time-stepping.

#### 4.4.2. Diffusion schemes

The conventional finite element method can be used to solve parabolic differential equations such as heat diffusion. The heat diffusion equation can be written as (see eqn.(4.4)):

$$\gamma \frac{\partial T}{\partial t} = \nabla \cdot \lambda \nabla T \quad (4.40)$$

where  $\lambda$  is constant thermal conductivity of matrix and  $\gamma$  is given by:

$$\gamma = \phi \rho_f c_{pf} + (1 - \phi) \rho_m c_{pm} \quad (4.41)$$

For simplicity, we set matrix porosity to zero and matrix density and specific heat capacity to 1. Therefore the term  $\gamma$  is 1 for the simulations.

Equation (4.40) is commonly solved by a number of schemes such as Explicit, Fully implicit, Crank-Nicolson and Exponential methods. Explicit methods result in non-physical values if large a time-step is taken. Here, we show this problem and examine other three different solution schemes for temperature diffusion equation and compare the results with an analytical solution. To solve the eqn. (4.40) analytically, a transient localized heat source is defined in the middle of a 2D domain. The temperature of the heat source decreases exponentially with the distance to the center of domain following a Gaussian function:

$$T = \frac{T_0}{1 + \frac{4t\lambda}{\rho_m c_{pm} l^2}} \exp\left(-\frac{\Delta x^2 + \Delta y^2}{l^2 + \frac{4t\lambda}{\rho_m c_{pm}}}\right) \quad (4.42)$$

where  $l$  is the length of Gaussian function set to 1000 m and  $T_0$  is initial temperature at the center of domain, set to 1000°C. The thermal conductivity used in the simulations is set to  $1 \times 10^{-6}$  W/m/K. In general, boundary conditions can be defined by Neumann, Dirichlet or mixed methods. The domain is, however, taken large enough (30×30 km) in these simulations to avoid boundary effects.

#### 4.4.2.1. Analytical solution

The simulation result from analytical solution of the eqn. (4.40) after 150 ka of diffusion is shown in Figure 4-10. The initial temperature of heat source,  $T_0$ , is reduced from 1000 °C to 50 °C at this stage. According to eqn.(4.40), the heat transfer time from the heat source center to an arbitrary point in the matrix only depends on thermal conductivity of matrix and is independent to the initial temperature of heat source; therefore, it is not possible to expedite diffusion by initializing higher heat source temperature. We will later compare the results of the three numerical schemes mentioned above with the analytical solution. The diffusion equations in the three schemes are described for a one-dimensional domain using finite difference approach for simplicity.

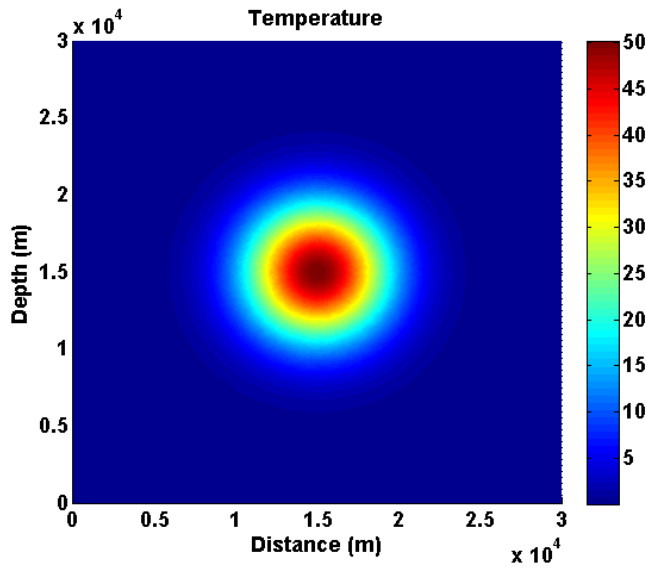


**Figure 4-10:** The analytical solution of a localized heat source in the middle of domain after 150 ka of conduction.

#### 4.4.2.2. Explicit method

Finite difference approximations employed in the solution of temperature diffusion are first defined as a function of only space, and subsequently, the time dependency in the equations is introduced. For a given 1D domain containing  $n$  grid nodes, the right-hand side of eqn. (4.40) can be written as:

$$\nabla \cdot \lambda \nabla T = \frac{1}{\Delta x} \left( \lambda_{i+1/2} \frac{\partial T}{\partial x_{i+1/2}} - \lambda_{i-1/2} \frac{\partial T}{\partial x_{i-1/2}} \right) \quad (4.43)$$

By taking the temperature at the center of two adjacent nodes, we can approximate the partial differential equations by finite difference terms using Taylor's series expansion:

$$\frac{\partial T}{\partial x_{i+1/2}} \approx \frac{T_{i+1} - T_i}{\Delta x} \quad (4.44)$$

By substituting eqn. (4.44) into eqn.(4.43), we can approximate the diffusion equations:

$$\frac{\partial}{\partial x} \left( \lambda \frac{\partial T}{\partial x} \right) \approx \frac{1}{\Delta x^2} \left[ \lambda_{i-1/2} T_{i-1} - (\lambda_{i-1/2} + \lambda_{i+1/2}) T_i + \lambda_{i+1/2} T_{i+1} \right] \quad (4.45)$$

Since we assumed that thermal conductivity is constant in space, the eqn. (4.45) can be re-written:

$$\frac{\partial}{\partial x} \left( \lambda \frac{\partial T}{\partial x} \right) \approx \frac{\lambda}{\Delta x^2} \left[ T_{i-1} - 2T_i + T_{i+1} \right] \quad (4.46)$$

As in explicit methods, the temperature at time  $n+1$  depends explicitly on the temperature at time  $n$ , by substituting eqn. (4.46) into eqn. (4.40) to add the time derivatives, we obtain:

$$T_i^{n+1} \approx T_i^n + \frac{\lambda \Delta t}{\gamma \Delta x^2} [T_{i-1}^n - 2T_i^n + T_{i+1}^n] \quad (4.47)$$

If we define a diffusion parameter by  $M = \frac{\lambda \Delta t}{\gamma \Delta x^2}$ , the eqn. (4.47) yields:

$$T_i^{n+1} \approx MT_{i-1}^n + (1 - 2M)T_i^n + MT_{i+1}^n \quad (4.48)$$

According to this equation, it is simply shown that if  $\Delta t > \frac{\gamma \Delta x^2}{2\lambda}$  this scheme becomes unstable because by taking large time steps, the second term in the RHS produces negative temperature and the solution confronts growing oscillations in time and finally unrealistic solution is achieved. Although this scheme is simple and computationally fast, the time-stepping limitation is its major drawback. Therefore, this method is not appropriate for high-resolution simulations, where large number of nodes is present and thus other stable methods should be employed instead. The presented solution can be easily generalized for 2D domains as well.

#### 4.4.2.3. Fully implicit method

In fully implicit scheme, similar formulation is derived except for the spatial derivatives which are evaluated at time step  $n+1$ . In other words, the eqn. (4.47) becomes:

$$T_i^{n+1} \approx T_i^n + M [T_{i-1}^{n+1} - 2T_i^{n+1} + T_{i+1}^{n+1}] \quad (4.49)$$

Therefore, to find the temperature at time step  $n+1$ , the following equation should be solved:

$$-MT_{i+1}^{n+1} + (1 + 2M)T_i^{n+1} - MT_{i-1}^{n+1} \approx T_i^n \quad (4.50)$$

The operator applied on time step  $n$  is a tridiagonal, symmetric and positive definite matrix and can be solved easily by computer programs. Clearly, by taking arbitrary large time steps, the stiffness matrix will not go negative and therefore, this scheme is stable and realistic. This scheme is first order in  $\Delta t$  as by taking half time-step, the accuracy will be improved by factor 2. To improve the accuracy of solution, one can employ a second-order scheme as a substitute for explicit and fully implicit methods.

#### 4.4.2.4. Crank-Nicolson method

The Crank-Nicolson scheme is a second-order scheme as it computes the temperature diffusion at a time-step  $T^{n+1/2}$ , where  $T^{n+1/2}$  is the temperature centered between time-steps  $n$  and  $n+1$ .

By evaluating the spatial derivatives on half time step forward, we obtain:

$$T_i^{n+1} \approx T_i^n + M \left[ T_{i-1}^{n+1/2} - 2T_i^{n+1/2} + T_{i+1}^{n+1/2} \right] \quad (4.51)$$

Rearranging eqn. (4.51) and assuming that temperature at half time-step is an average between the temperature of time step  $n$  and  $n+1$ , yields:

$$-MT_{i-1}^{n+1} + 2(1+M)T_i^{n+1} - MT_{i+1}^{n+1} \approx MT_{i-1}^n + 2(1-M)T_i^n + MT_{i+1}^n \quad (4.52)$$

This scheme is unconditionally stable; however the solution oscillates initially until convergence is achieved. A bit experience with crank-Nicolson shows that taking larger time steps may lead to larger numerical errors. The stability of this scheme means that the errors diminish with time, unlike the explicit method (which results in growing errors as time passes). In the next sections, we will see that for small time-steps, the accuracy of Crank-Nicolson is considerably better than fully implicit scheme.

#### 4.4.2.5. Exponential method

The exponential scheme is developed to keep the accuracy of Crank-Nicolson in small time-steps while producing realistic results and is unconditionally stable in large time-steps (Patankar and Baliga, 1978). In this scheme, the time-dependent equation for temperature diffusion yields:

$$T_i^{n+1} \approx T_i^n + M [T_{i+1} + T_{i-1} - 2T_i] \quad (4.53)$$

where the mean temperature over the time step,  $T_i$ , is defined as a function of temperature in time step  $n$  and time step  $n+1$ :

$$T_i = f_i T_i^{n+1} + (1 - f_i) T_i^n \quad (4.54)$$

where

$$f_i = \frac{1}{1 - \exp(-M)} - \frac{1}{M} \quad (4.55)$$

By substituting eqns.(4.54) and (4.55) into eqn.(4.53), we obtain:

$$(1 + Mf_i)T_i^{n+1} = \frac{M}{2} \left[ f_{i+1} T_{i+1}^{n+1} + f_{i-1} T_{i-1}^{n+1} + (1 - f_{i+1}) T_{i+1}^n + (1 - f_{i-1}) T_{i-1}^n + [1 - M(1 - f_i)] T_i^n \right] \quad (4.56)$$

This equation is a general form for solving temperature diffusion as all the four schemes described earlier can be derived from this equation. For example, by defining  $f_i = 0$ , the eqn. (4.56) becomes similar to eqn. (4.48) which describes the explicit scheme. Similarly, by defining  $f_i = 0.5$  and  $1$  we derive eqns.(4.50) and (4.52) representing fully implicit and Crank-Nicolson equations, respectively. The parameter  $f_i$  must be defined between  $0.5$  and  $1$  to ascertain the stability of solution.

### 4.4.2.6. Comparison

In this section, three simulations by different diffusion schemes in 2D domain are presented and compared to the analytical solution described in section 4.4.2.1. The localized heat source defined by eqn. (4.42) is initialized for all the numerical schemes and the model is run for 150 ka. The same thermal conductivity to analytical solution is used in all simulations. Figure 4-11 shows the results of temperature ratio of time step  $n+1$  to the time step  $n$  versus diffusion parameter,  $M$ . The temperature ratio is directly proportional to the time step. Fully implicit method does not experience negative values even by taking large time steps; therefore, this scheme is always stable. At a given time step, Crank-Nicolson scheme apparently results similar to fully implicit method, but by choosing large time steps, the negative ratio can translate to spurious oscillations in the solution. Similar to fully implicit scheme, the temperature ratio for exponential scheme does not go negative for any given time step.

To find the optimum solution, we need to compare the numerical solutions with the analytical solution. Figure 4-12 illustrates the difference in temperature of heat source at the center of domain between analytical and numerical solutions in the three schemes as a function of time. The simulation results show that the minimum difference is achieved when the temperature diffusion is solved by crank-Nicolson scheme at any given time, where the results of the other two schemes are also acceptable. At the late stage, however, all the simulations result in almost similar differences to the analytical solution.

To further explore the performance of the aforementioned schemes, temperature differences between analytical and numerical solutions after 150 ka of diffusion are plotted in Figure 4-13. Fully implicit and exponential methods show similar temperature differences, whereas in Crank-Nicolson scheme, the difference is significantly lower and it is restricted to the region close to the heat source. According to the results, the heat diffusion equation can be solved efficiently by Crack-Nicolson method; however, large time-steps should be

avoided. Nevertheless, Exponential scheme seems to be better solution method for heat diffusion problems as it is stable for any given time step.

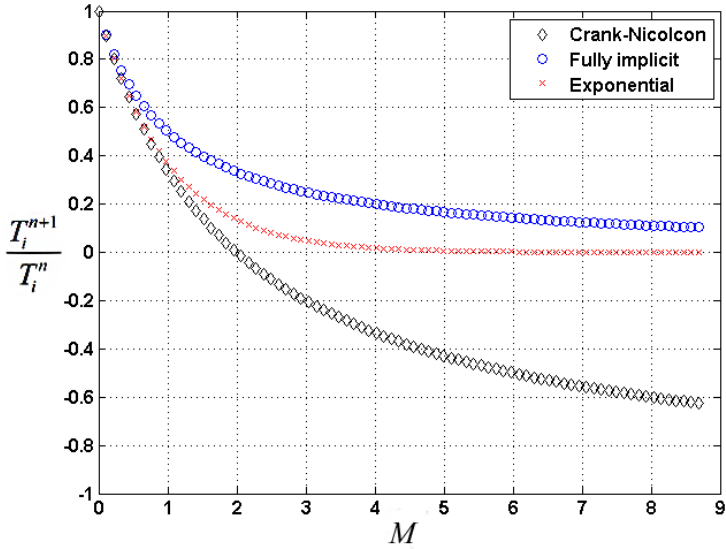


**Figure 4-11:** Temperature ratio during one time step as a function of a diffusion parameter.

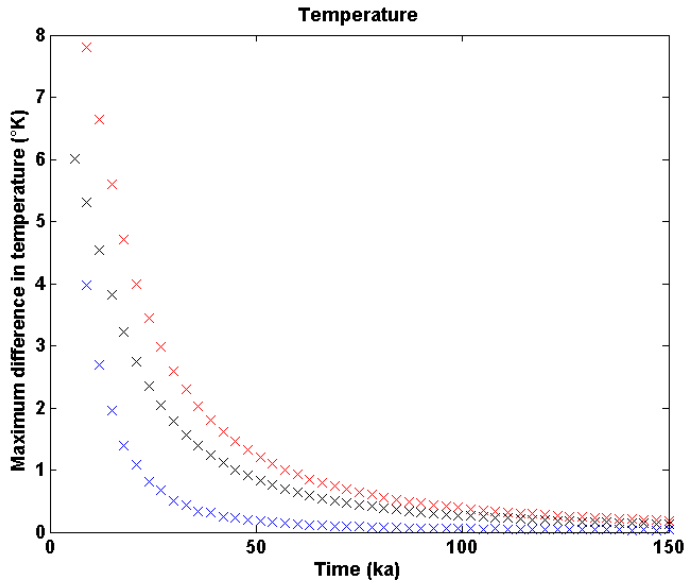


**Figure 4-12:** Maximum difference in temperature of domain center between numerical and analytical solutions calculated at each time step.

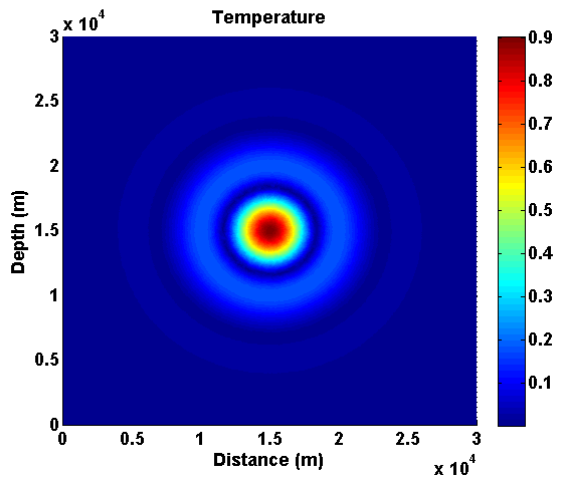
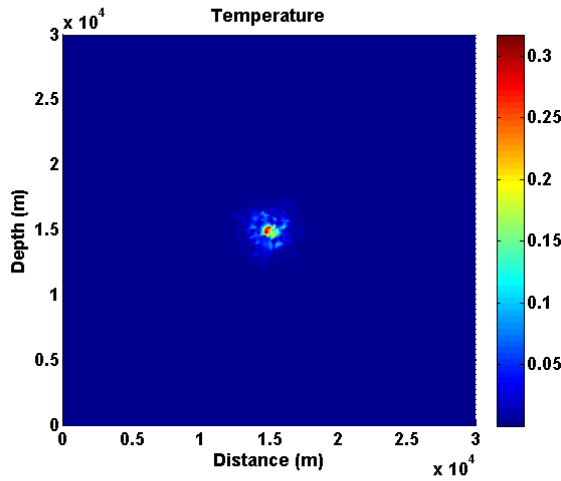
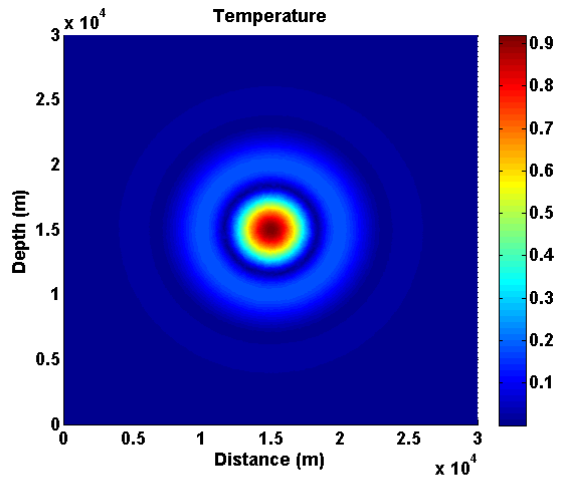


**Figure 4-13:** The misfit between the analytical and numerical schemes after 150 ka of conduction: a) Fully implicit scheme, b) Crank-Nicolson scheme and c) Exponential scheme.

### 4.4.3. Nusselt number

In heat transfer problems, the ratio of convective heat transfer to conductive heat transfer is called Nusselt number. Note that in this context, convection is conduction together with advection. Physically, this dimensionless number represents the type of convection, i.e. if the Nusselt number is close to 1, the magnitude of convection and conduction is similar and therefore the convection is sluggish. In contrast, if the Nusselt number is much larger than 1, the convection is vigorous. For free convection, Nusselt number is a function of Rayleigh number which is a dimensionless number associated with buoyancy-driven flow. The Rayleigh number accounts for the vigor of convection and is calculated by:

$$Ra = \frac{k \rho g z \alpha \Delta T}{\mu d} \quad (4.57)$$

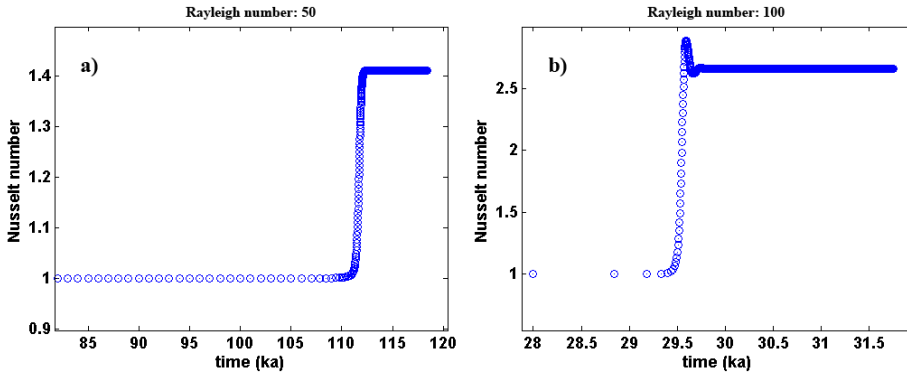
where  $z$  is the depth of the domain,  $d$  is thermal diffusivity and  $\alpha$  is the thermal expansion coefficient.

To calculate the Nusselt number in an open-top porous matrix that is uniformly and continuously heated from below, we should integrate the conduction and convection terms over the surface of the matrix. The vertical boundaries are adiabatic and impermeable and the bottom boundary is impermeable. All the values for matrix and fluid properties are set to 1 for simplicity and the fluids can only enter or exit the matrix through upper boundary. The Nusselt number which provides the measure of heat flux across the porous medium is obtained by:

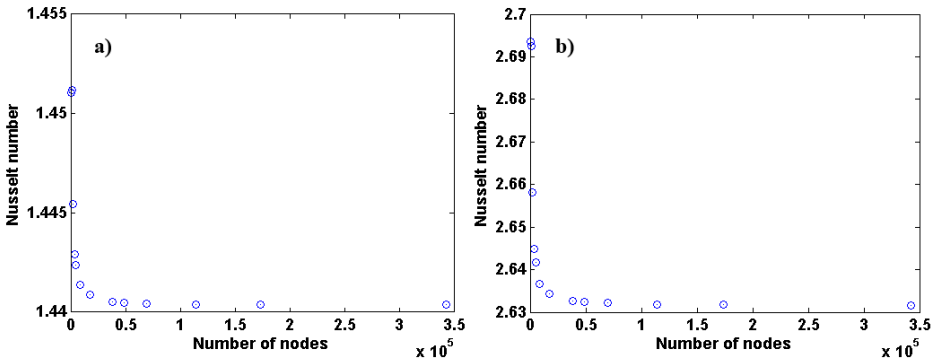
$$Nu = -\int_0^1 \frac{\partial}{\partial y} \left( \frac{T}{\Delta T} \right) \Big|_{y=0} dx \quad (4.58)$$

Figure 4-14 shows the calculation of Nusselt number in time where two Rayleigh numbers of 50 and 100 describe the convective behavior. The Nusselt number is initially 1 meaning that the heat only transfers by diffusion and fluid advection is not started yet. As soon as the temperature-induced pressure becomes large between the nodes in the matrix, fluid velocities become high enough to drive the fluids and the Nusselt number increases rapidly to certain value –which depends on fluid and matrix properties- and oscillates for a while until it converges to its steady-state value. The Nusselt numbers obtained in such settings are 1.44 and 2.63 corresponding to Rayleigh numbers of 50 and 100, respectively. These values are in good consistency with the results calculated by Cherkaoui and Wilcock (1999).

If the simulated domain is low-resolution, the Nusselt number is always over-estimated. To illustrate this fact, the Nusselt number is calculated as a function of number of nodes in the matrix (Figure 4-15). The results show that if at least 50,000 elements (equivalently ~100,000 nodes for a system of three-node element) are used in a unit of area in this particular test, the Nusselt number is well-estimated. In fact, for different matrix and fluid properties, the minimum number of elements used in the simulations should be calculated to find the closest estimation for Nusselt number. Nevertheless, recent fast computers provide ability to model the domains in high-resolution in a reasonable time.



**Figure 4-14:** Calculation of Nusselt number in a dimensionless system where a) Rayleigh number is 50 and b) Rayleigh number is set to 100.

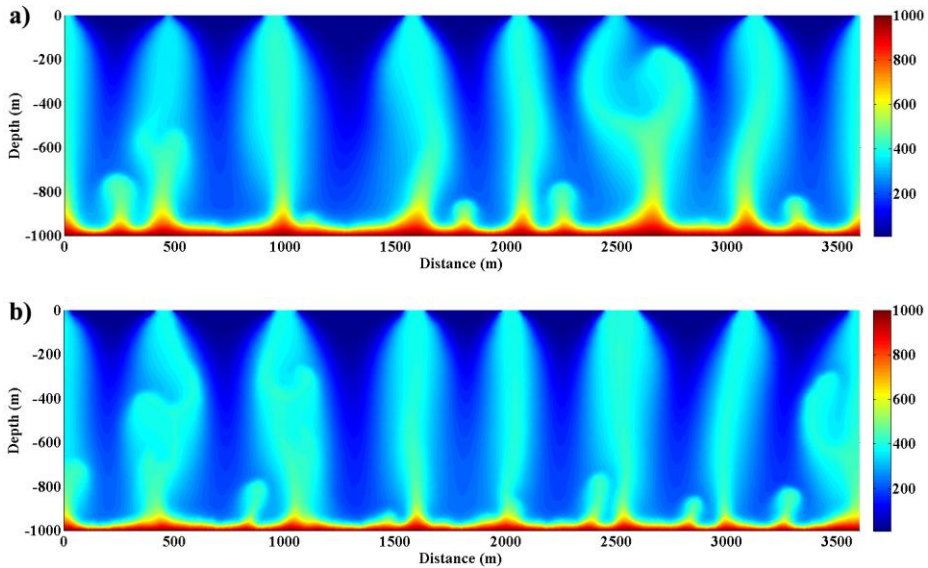


**Figure 4-15:** Calculation of Nusselt number as a function of domain resolution. This analysis suggests the minimum resolution required for a simulation.

#### 4.4.4. Hydrothermal convection

In this section, we simulate a real hydrothermal system and compare the two advection methods in an open-top box. In these simulations, heat transfer due to thermal diffusion is also taken into consideration. The fully implicit diffusion method, described in section 4.4.2.3, is used for both simulations. The spatially and temporally constant permeability and porosity used in both simulations are

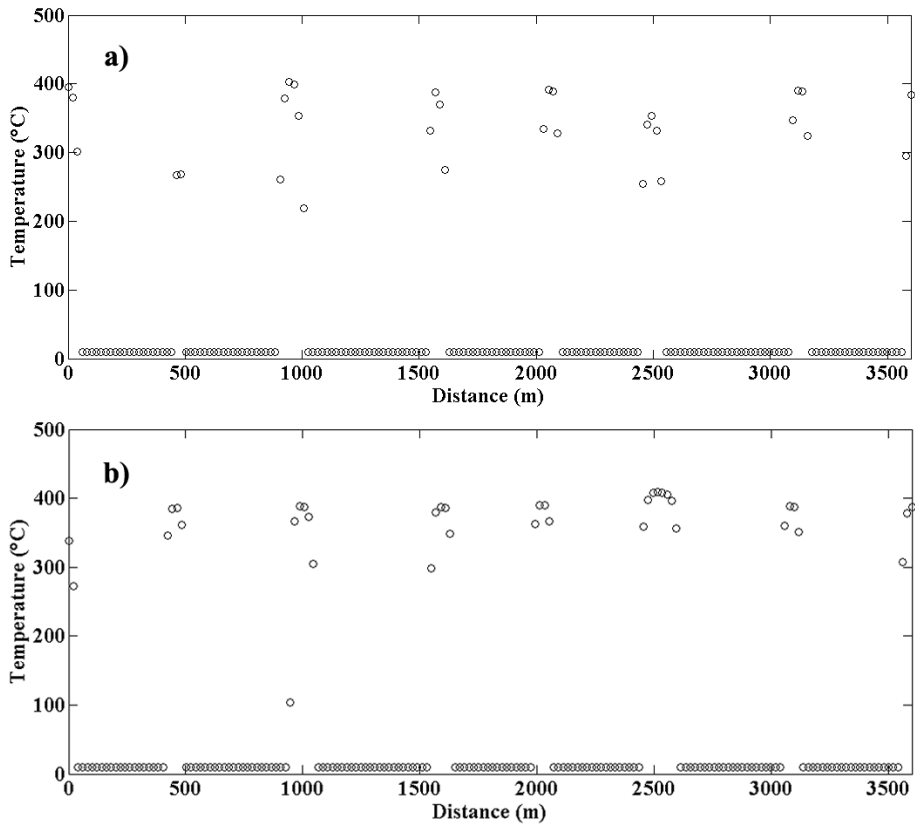
$5 \times 10^{-15} \text{ m}^2$  and 10%, respectively. Thermal conductivity, matrix density and specific heat capacity of matrix are prescribed to  $2 \text{ W.m}^{-1}.\text{K}^{-1}$ ,  $2700 \text{ kg.m}^{-3}$  and  $880 \text{ J.kg}^{-1}.\text{K}^{-1}$ , respectively.



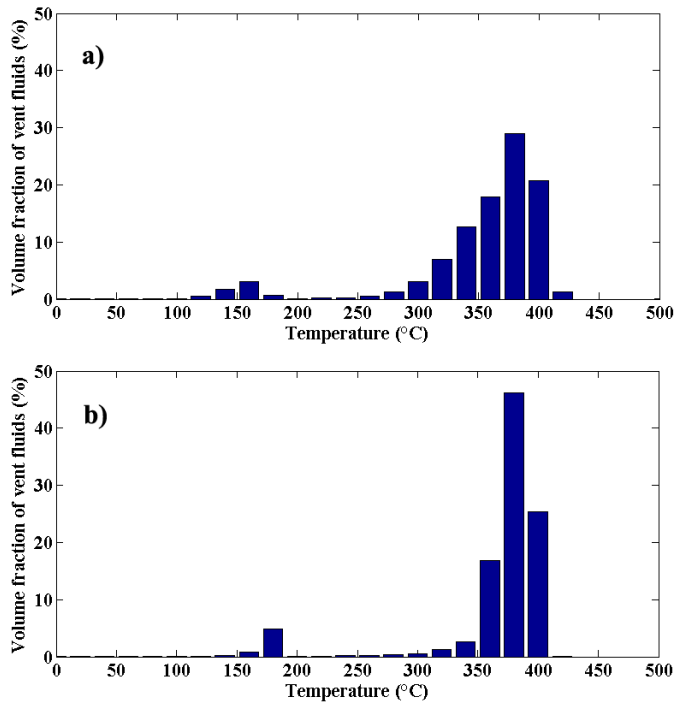
**Figure 4-16:** Hydrothermal circulation in an open box after 3000 years of convection by using a) Semi-Lagrangian method b) Finite volume method.

Figure 4-16 a and b show the simulation results of open top hydrothermal convection simulations performed by semi-Lagrangian method and FVM, respectively, after 3000 years of convection. The models advected by semi-Lagrangian and finite volume methods are sequentially solved using SL and CFL time-stepping criterions, explained in section 4.4.1, respectively. Second-order accuracy (*see* section 4.4.1) is applied on the FVM to maintain precision in the simulation. The hydrothermal plumes initiated at the base of the model reach the surface after a few hundred years. The simulation results at the late stage for both simulations exhibit eight plumes venting at the seafloor. The models are at quasi-steady state where plumes are continuously generated at the

bottom of model and merge to the established ones. Similar pattern of hydrothermal plumes in the two simulations and the same aspect ratio of the plumes credit both methods in simulating a real hydrothermal convection model. The simulation time for 3000 years of convection is approximately an order of magnitude higher when advection is solved by FVM rather than semi-Lagrangian method. Although FVM resolves the hydrothermal convection slightly better than semi-Lagrangian for similar parameters as discussed in section 4.4.1, semi-Lagrangian method is preferred as it preserves efficiency in time. High temperature zone ( $>800^{\circ}\text{C}$ ) is vertically limited to the first 50 m from the bottom of model in FVM method (Figure 4-16 b), whereas this zone extends up to 100 m in semi-Lagrangian method (Figure 4-16 a). The reason can be explained by diffusive nature of semi-Lagrangian method. Figure 4-17 shows vent temperature at the late stage of simulation. The vent temperatures for both methods do not exceed  $400^{\circ}\text{C}$  which confirms finding of Jupp and Schultz (2000) for mid-ocean ridge settings. The bar diagrams presented in Figure 4-18 show volume fraction of vent fluids as a function of vent temperature calculated from 1000 years of convection until quasi steady state is approached (3000 years of convection). The fluids venting at the tip of hydrothermal plumes possess temperatures slightly less than  $400^{\circ}\text{C}$  for both simulations. A small fraction of plumes vent at higher temperatures as a result of instability in convection associated with the given matrix permeability. These figures show that venting is more focused in the results of simulation by FVM. Nonetheless, the convection pattern as well as vent temperatures for both methods are rather similar suggesting validity of simulation results carried out by semi-Lagrangian method.



**Figure 4-17:** Vent temperature at the seafloor for simulations carried out by a) Semi-Lagrangian Method and b) Finite Volume Method.



**Figure 4-18:** Volume fraction of vent fluids as a function of temperature for simulations conducted by a) Semi-Lagrangian method and b) Finite Volume Method.



# Chapter 5

## Conclusions



## Conclusions

In this thesis, a new MATLAB-based finite element-finite volume (FEFVM) code that resolves single-phase fluid flow in highly heterogeneous media is developed. The simulations performed in this work are driven from the necessity to understand the observations and associated subsurface physical processes that occur at mid-ocean ridges and passive continental margins. Modeling can shape the perspectives of scientists on the aforementioned processes and possibly predict future physical processes in the Earth's interior in a step-wise manner.

The developed code allows simulating highly heterogeneous media including faults and fractures, as well as sill intrusions. This is achieved through the use of unstructured meshes, which permits the users to accurately simulate magmatic hydrothermal systems. These abilities in mesh generation and numerical solutions provide thorough insights into the Earth's interior processes during simulations.

To understand the effects of bathymetric relief on hydrothermal plume deviation and interaction in submarine settings, a systematic study is presented. The results show the extent to which a single plume can deviate from its origin as a result of the bathymetric effect. A linear relationship among plume deviation, surface slope, and depth from the heat source is found. To identify the effect of bathymetric relief on multiple plumes and to understand the interaction between the plumes during their ascent, a series of simulations with the assumption that the surface is defined by a sinusoidal function are conducted.

## Conclusions

---

These simulations show that high amplitudes are key controls in shifting hydrothermal plumes that result from pressure differences associated with density changes. The simulation results indicate that surface slope can indeed affect the vent-site location and show how plumes migrate toward bathymetric highs. To understand such processes in actual geological settings, hydrothermal convections in Lucky-Strike and East Pacific Rise 9° 30'N vent fields as case studies are modeled. The results of the simulations for both case studies show that axial high helps focusing venting at the ridge axis. This suggests that the effect of bathymetric relief should be accounted for to explain on-axis venting observed in case studies.

To examine the effect of transient heat sources in continental settings (volcanic passive margins), fluid flow is simulated in a case study on the Gjallar Ridge area, off Norway. Given that Gjallar Ridge is affected by a swarm of sills during North Atlantic continental break-up, a large number of hydrothermal vent sites have been observed. The simulation results show that the injected sills can trigger hydrothermal fluid flow and sustain convections up to approximately 10,000 years, during which the duration of high temperature venting (>200 °C) is limited to a millennium. The simulation results also elucidate that faults are key to heat transfer to upper sediment layers. Besides, the impermeable sills may confine ascending hydrothermal plumes. The presence of sills with the associated hydrothermal convections matures the organic matter buried in surrounding source rock and forms hydrocarbons. Vitrinite reflectance is used as an indication for maturity of source-rock. The remarkable differences in the results for heat dissipation in two different schemes of convection- and conduction-driven systems suggest that fluid advection is important in calculating the maturity of source rock.

The series of simulations presented in this work, also suggest the strengths and limitations of different numerical solution techniques. In these simulations, different temperature diffusion and advection schemes are explained, in which different heat sources and boundary conditions are present. The simulations show that choosing a large time step or an inappropriate solution method cause models to produce non-physical or oscillating results. The two most popular

advection schemes, i.e. semi-Lagrangian and FVM, are evaluated in resolving heat transfer by fluids. The mass-conserving FVM can almost accurately simulate the advection process, but this scheme suffers from limited time stepping. By contrast, the semi-Lagrangian method solves advection problems with reasonable precision in the results, where the time step can be chosen orders of magnitude higher than that of FVM for similar resolution. In addition, three different methods of diffusion solutions are evaluated and compared: fully implicit, Crank-Nicolson, and exponential methods. The results reveal that the fully implicit method is always stable and does not produce negative quantities, whereas the Crank-Nicolson method presents decaying spurious oscillations; however, it is unconditionally stable in time. Therefore, to minimize the oscillations in the results, small time steps should be used. The exponential method is also stable and does not produce non-physical values, but it differs from the analytical solution in that it is not as accurate as the Crank-Nicolson scheme. The simulation results suggest that a general optimum method cannot be defined as the accuracy of interest, structural complexities in matrix and modeling time varies from a model to another. Furthermore, dimensionless Nusselt numbers are evaluated and benchmarked against the previous studies. By these simulations, an estimate of the minimum resolution required in the simulations can be achieved. When the simulations are performed in low resolution, the Nusselt number is over-estimated.

The permeability structure at mid-ocean ridges is unknown and the ones used in our simulations are defined on the basis of previous numerical studies. The permeability structure in the Gjallar Ridge area is also estimated on the basis of depth-dependent porosity. The actual-nature permeability structure, however, may differ from the ones used in the models and may change simulation results. The effective porosity of rocks can also be derived only by direct sampling, but fracture networks can be traced by high-resolution seismic studies. According to the simulation results, the understanding of faulting mechanisms as the major effective factor for advective heat transfer draws special interest because the faults are extreme pathways along which fluid is

## Conclusions

---

channeled. Tectonic processes may lead to fault opening, which accelerates convection or fault closure as a consequence of rock melting that shuts down fluid convection. Mineral precipitations can also clog the faults. Together with the information on the lithology of sediments and chemical water-rock reactions, the fluid pathways can provide insights into ore formation processes. The presented results show two-dimensional behavior, whereas in reality, convection occurs inside a fault plane where some of its parts are recharging while other parts discharging. Three-dimensional simulations are therefore required to elucidate the flow mechanism in the faults. Moreover, the high temperature gradient close to heat sources causes vigorous convection in the highly fractured zones. Consequently, instabilities and non-physical oscillations may be observed during plume ascent because the fluid velocities do not obey Darcy's law. In such a case, system behavior should be considered in high Rayleigh and Nusselt number conditions, such as Rayleigh-Bénard convection. These processes should, therefore, be taken into account in next studies.

Although the simulations are performed in the presence of single-phase fluid, the necessity of simulations under multiphase conditions cannot be disregarded. Seawater contains chemical components, such as NaCl and CO<sub>2</sub>, which shift boiling curve and cause salt precipitation. These precipitations decrease the permeability by clogging the pathways and impede the convection. Simulations should therefore be performed in a system of CO<sub>2</sub>-NaCl-H<sub>2</sub>O using multiphase fluid formulation and taking the permeability structure into consideration. When the chemical interactions between fluids and rock in such a setting are understood, the observations can be accurately explained by simulations. These processes may affect the plume distribution in the magmatic system and facilitate the prediction of off-axis hydrothermal vents. Such simulations and processes are recommended to be addressed in future works.

# Bibliography

- Aarnes, I., Svensen, H., Connolly, J.A.D. and Podladchikov, Y.Y., 2010. How contact metamorphism can trigger global climate changes: Modeling gas generation around igneous sills in sedimentary basins. *Geochim. Cosmochim. Acta*, 74(24): 7179-7195.
- Allen, D.E. and Seyfried, W.E., 2003. Compositional controls on vent fluids from ultramafic-hosted hydrothermal systems at mid-ocean ridges: An experimental study at 400 degrees C, 500 bars. *Geochimica Et Cosmochimica Acta*, 67(8): 1531-1542.
- Alt, J., 1995. Subseafloor processes in mid-ocean ridge hydrothermal systems. . AGU Monograph Series, 91.
- Anderson, T.R. and Fairley, J.P., 2008. Relating permeability to the structural setting of a fault-controlled hydrothermal system in southeast Oregon, USA. *J. Geophys. Res.-Solid Earth*, 113(B5).
- Athy, L.F., 1930. Density, porosity and compaction of sedimentary rocks. *Bull. Amer. Assoc. Petrol. Geol.*, 14: 1-24.
- Audetat, A., Gunther, D. and Heinrich, C.A., 1998. Formation of a magmatic-hydrothermal ore deposit: Insights with LA-ICP-MS analysis of fluid inclusions. *Science*, 279(5359): 2091-2094.
- Aziz, K. and Settari, A., 1979. *Petroleum Reservoir Simulation*. Applied Science Publishers, Ltd, London.
- Bach, W., Garrido, C.J., Paulick, H., Harvey, J. and Rosner, M., 2004. Seawater-peridotite interactions: First insights from ODP Leg 209, MAR 15 degrees N. *Geochemistry Geophysics Geosystems*, 5.
- Baker, E.T., 2009. Relationships between hydrothermal activity and axial magma chamber distribution, depth, and melt content. *Geochem. Geophys. Geosyst.*, 10.

## Bibliography

---

- Baker, E.T. and German, C.R., 2004. On the Global Distribution of Hydrothermal Vent Fields. In: C.R. German, J. Lin and L.M. Parson (Editors), *Mid-ocean ridges: hydrothermal interactions between the lithosphere and oceans*. American Geophysical Union, Washington DC, pp. 318pp.
- Bani-Hassan, N., Iyer, K., Rüpke, L.H. and Borgia, A., 2012. Controls of bathymetric relief on hydrothermal fluid flow at mid-ocean ridges. *Geochem. Geophys. Geosyst.*, 13: Q05002.
- Baran, J.M., Cochran, J.R., Carbotte, S.M. and Nedimovic, M.R., 2005. Variations in upper crustal structure due to variable mantle temperature along the Southeast Indian Ridge. *Geochem. Geophys. Geosyst.*, 6: 21.
- Bartholomew, I.D., Peters, J.M. and Powell, C.M., 1993. Regional structural evolution of the North Sea; oblique slip and the reactivation of basement lineaments. In: *Petroleum Geology of Northwest Europe; Proceedings of the 4th Conference* (Ed. by J.R.Parker), The Geol. Soc. Lond., UK, 2: 109-1122.
- Bauer, O., 1998. PROST: Properties of Water and Steam. <http://www.enersim.de/download/>.
- Belytschko, T., Gracie, R. and Ventura, G., 2009. A Review of Extended/Generalized Finite Element Methods for Material Modelling. *Modelling Simul. Mater. Sci. Eng.*, 17.
- Berndt, C., Skogly, O.P., Planke, S., Eldholm, O. and Mjelde, R., 2000. High-velocity breakup-related sills in the Voring Basin, off Norway. *J. Geophys. Res.-Solid Earth*, 105(B12): 28443-28454.
- Blystad, P., Brekke, H., Færseth, R.B., Larsen, B.T., Skogseid, J. and Tørudbakken, B., 1995. Structural elements of the Norwegian continental shelf. Part II. The Norwegian Sea Region. *Norwegian Petroleum Directorate Bulletin*, 8: 45.
- Boetius, A., 2005. Lost city life. *Science*, 307(5714): 1420-1422.
- Boillot, G. and Froitzhelm, N., 2001. Non-volcanic rifted margins, continental break-up and the onset of sea-floor spreading: some outstanding questions. The Geological Society of London.

- Bostick, N.H., 1971. Thermal alteration of clastic organic particles as an indicator of contact and burial metamorphism in sedimentary rocks. *Geoscience and Man*, 3: 83-93.
- Brekke, H., 2000. The tectonic evolution of the Norwegian Sea continental margin with emphasis on the Vøring and Møre Basins. In: *Dynamics of the Norwegian Margin* (Ed. by A. Nøttvedt), *Geol. Soc. Spec. Publ.*, 167: 327-378.
- Brekke, H., Sjulstad, H.I., Magnus, C. and Williams, R.W., 2001. Sedimentary environments offshore Norway—an overview. *NPF Special Publication*, 10: 7-37.
- Buck, W.R., Carbotte, S.M. and Mutter, C., 1997. Controls on extrusion at mid-ocean ridges. *Geology*, 25(10): 935-938.
- Bukovics, C., Cartier, E.G., Shaw, N.D. and Ziegler, P.A., 1984. Structure and development of the Mid-Norway continental margin. In: *Spencer, A.M., Editor, , 1984. Petroleum geology of the north European margin, Norwegian Petroleum Society*: 407-423.
- Burnham, A.K. and Sweeney, J.J., 1989. A chemical kinetic model of vitrinite maturation and reflectance. *Geochemica et Cosmochemica Acta*, 53: 2649-2657.
- Canga, M.E. and Becker, E.B., 1999. An iterative technique for the finite element analysis of near-incompressible materials. *Comput. Meth. Appl. Mech. Eng.*, 170(1-2): 79-101.
- Cann, J.R., Elderfield, H. and Laughton, A., 1999. *Mid-ocean ridges: Dynamic of processes associated with creation of new ocean crust*. Cambridge University Press.
- Carbotte, S.M. and Macdonald, K.C., 1994. The axial topographic high at intermediate and fast spreading ridges. *Earth and Planetary Science Letters*, 128(3-4): 85-97.
- Carbotte, S.M., Mutter, C., Mutter, J. and Ponce-Correa, G., 1998. Influence of magma supply and spreading rate on crustal magma bodies and

## Bibliography

---

- emplacement of the extrusive layer: Insights from the East Pacific Rise at lat 16°N. *Geology*, 5: 455-458.
- Cathles, L.M., 1977. Analysis of cooling of intrusives by groundwater convection which includes boiling. *Economic Geology*, 72(5): 804-826.
- Cathles, L.M., Erendi, A.H.J. and Barrie, T., 1997. How long can a hydrothermal system be sustained by a single intrusive event? *Econ. Geol. Bull. Soc. Econ. Geol.*, 92(7-8): 766-771.
- Charlou, J.L., Donval, J.P., Douville, E., Jean-Baptiste, P., Radford-Knoery, J., Fouquet, Y., Dapoiny, A. and Stievenard, M., 2000. Compared geochemical signatures and the evolution of Menez Gwen (37 degrees 50 ' N) and Lucky Strike (37 degrees 17 ' N) hydrothermal fluids, south of the Azores Triple Junction on the Mid-Atlantic Ridge. *Chem. Geol.*, 171(1-2): 49-75.
- Charlou, J.L., Donval, J.P., Fouquet, Y., Jean-Baptiste, P. and Holm, N., 2002. Geochemistry of high H<sub>2</sub> and CH<sub>4</sub> vent fluids issuing from ultramafic rocks at the Rainbow hydrothermal field (36 degrees 14 ' N, MAR). *Chemical Geology*, 191(4): 345-359.
- Charlou, J.L., Donval, J.P., JeanBaptiste, P. and Dapoiny, A., 1996. Gases and helium isotopes in high temperature solutions sampled before and after ODP Leg 158 drilling at TAG hydrothermal field (26 degrees N, MAR). *Geophysical Research Letters*, 23(23): 3491-3494.
- Cherkaoui, A.S.M. and Wilcock, W.S.D., 1999. Characteristics of high Rayleigh number two-dimensional convection in an open-top porous layer heated from below. *J. Fluid Mech.*, 394: 241-260.
- Cherkaoui, A.S.M., Wilcock, W.S.D., Dunn, R.A. and Toomey, D.R., 2003. A numerical model of hydrothermal cooling and crustal accretion at a fast spreading mid-ocean ridge. *Geochem. Geophys. Geosyst.*, 4: 19.
- Choi, H.G., 2011. Comparison of a least-square weighted residual method and the Taylor-Galerkin method based on level set formulation for interface capturing. *Prog. Comput. Fluid Dyn.*, 11(3-4): 169-174.

- 
- Coakley, B.J. and Cochran, J.R., 1998. Gravity evidence of very thin crust at the Gakkel Ridge (Arctic Ocean). *Earth and Planetary Science Letters*, 162(1-4): 81-95.
- Connelly, D.P., Copley, J.T., Murton, B.J., Stansfield, K., Tyler, P.A., German, C.R., Van Dover, C.L., Amon, D., Furlong, M., Grindlay, N., Hayman, N., Huhnerbach, V., Judge, M., Le Bas, T., McPhail, S., Meier, A., Nakamura, K., Nye, V., Pebody, M., Pedersen, R.B., Plouviez, S., Sands, C., Searle, R.C., Stevenson, P., Taws, S. and Wilcox, S., 2012. Hydrothermal vent fields and chemosynthetic biota on the world's deepest seafloor spreading centre. *Nat. Commun.*, 3.
- Corfield, S.M., Wheeler, W., Karpuz, R., Wilson, M. and Helland, R., 2004. Exploration 3D Seismic over the Gjallar Ridge, Mid-Norway: Visualization of Structures on the Norwegian Volcanic Margin from Moho to Seafloor. *Geological Society, London, Memoirs*, 29: 177-186.
- Corliss, J.B., Baross, J.A. and Hoffman, S.E., 1981. An hypothesis concerning the relationship between submarine hot springs and the origin of life on Earth. *Oceanol. Acta*, 1: 59-69.
- Corliss, J.B., Dymond, J., Gordon, L.I., Edmond, J.M., von Herzen, R.P., Ballard, R.D., Green, K., Williams, D., Bainbridge, A., Crane, K. and van Andel, T.H., 1979. Submarine Thermal Springs on the Galapagos Rift. *Science*, 203(4385).
- Coumou, D., Driesner, T., Geiger, S., Heinrich, C.A. and Matthäi, S., 2006. The dynamics of mid-ocean ridge hydrothermal systems: Splitting plumes and fluctuating vent temperatures. *Earth and Planetary Science Letters*, 245(1-2): 218-231.
- Coumou, D., Driesner, T., Geiger, S., Paluszny, A. and Heinrich, C.A., 2009a. High-resolution three-dimensional simulations of mid-ocean ridge hydrothermal systems. *J. Geophys. Res.-Solid Earth*, 114: 15.
- Coumou, D., Driesner, T. and Heinrich, C.A., 2008a. The structure and dynamics of mid-ocean ridge hydrothermal systems. *Science*, 321(5897): 1825-1828.

## Bibliography

---

- Coumou, D., Driesner, T., Weis, P. and Heinrich, C.A., 2009b. Phase separation, brine formation, and salinity variation at Black Smoker hydrothermal systems. *J. Geophys. Res.-Solid Earth*, 114: 16.
- Coumou, D., Matthai, S., Geiger, S. and Driesner, T., 2008b. A parallel FE-FV scheme to solve fluid flow in complex geologic media. *Comput. Geosci.*, 34(12): 1697-1707.
- Dabrowski, M., Krotkiewski, M. and Schmid, D.W., 2008. MILAMIN: MATLAB-based finite element method solver for large problems. *Geochem. Geophys. Geosyst.*, 9.
- deMartin, B.J., Canales, R.A.R., Canales, J.P. and Humphris, S.E., 2007. Kinematics and geometry of active detachment faulting beneath the Trans-Atlantic Geotraverse (TAG) hydrothermal field on the Mid-Atlantic Ridge. *Geology*, 35(8): 711-714.
- Detrick, R.S., Buhl, P., Vera, E., Mutter, J., Orcutt, J., Madsen, J. and Brocher, T., 1987. Multichannel seismic imaging of a crustal magma chamber along the east pacific rise. *Nature*, 326(6108): 35-41.
- Dick, H.J.B., Lin, J. and Schouten, H., 2003. An ultraslow-spreading class of ocean ridge. *Nature*, 426(6965): 405-412.
- Doré, A.G., Lundin, E.R., Jensen, L.N., Birkeland, Ø., Eliassen, P.E. and Fichler, C., 1999. In: *Principal tectonic events in the evolution of the northwest European Atlantic margin. Petroleum Geology of Northwest Europe: Proceedings of the 5th Conference* (Ed. by A.J. Fleet & S.A.R. Boldy), Geol. Soc. Lond., UK, 1: 41-62.
- Dow, W.G., 1977. Kerogen studies and geological interpretations. *Journal of Geochemical Exploration*, 7: 79-99.
- Driesner, T., 2010. The interplay of permeability and fluid properties as a first order control of heat transport, venting temperatures and venting salinities at mid-ocean ridge hydrothermal systems. *Geofluids*, 10(1-2): 132-141.
- Driesner, T. and Geiger, S., 2007. Numerical simulation of multiphase fluid flow in hydrothermal systems. In: A. Liebscher and C.A. Heinrich

---

(Editors), Fluid-Fluid Interactions. Reviews in Mineralogy & Geochemistry. Mineralogical Soc Amer, Chantilly, pp. 187-212.

- Driesner, T. and Heinrich, C.A., 2007. The system H<sub>2</sub>O-NaCl. Part I: Correlation formulae for phase relations in temperature-pressure-composition space from 0 to 1000 degrees C, 0 to 5000 bar, and 0 to 1 X-NaCl. *Geochim. Cosmochim. Acta*, 71(20): 4880-4901.
- Dunn, R.A., Toomey, D.R. and Solomon, S.C., 2000. Three-dimensional seismic structure and physical properties of the crust and shallow mantle beneath the East Pacific Rise at 9 30'N. *Journal of geophysical Research*, 105.
- Durlafsky, L.J., 1993. A Triangle Based Mixed Finite Element—Finite Volume Technique for Modeling Two Phase Flow through Porous Media. *Journal of Computational Physics*, 105(2): 252-266.
- Dusunur, D., Escartin, J., Combiér, V., Seher, T., Crawford, W., Cannat, M., Singh, S.C., Matias, L.M. and Miranda, J.M., 2009. Seismological constraints on the thermal structure along the Lucky Strike segment (Mid-Atlantic Ridge) and interaction of tectonic and magmatic processes around the magma chamber. *Mar. Geophys. Res.*, 30(2): 105-120.
- Dyment, J., Tamaki, K., Horen, H., Fouquet, Y., Nakase, K., Yamamoto, M., Ravilly, M. and Kitazawa, M., 2005. A positive magnetic anomaly at Rainbow hydrothermal site in ultramafic environment. AGU fall meeting abstracts.
- Dziak, R.P., Smith, D.K., Bohnenstiehl, D.R., Fox, C.G., Desbruyeres, D., Matsumoto, H., Tolstoy, M. and Fornari, D.J., 2004. Evidence of a recent magma dike intrusion at the slow spreading Lucky Strike segment, Mid-Atlantic Ridge. *J. Geophys. Res.-Solid Earth*, 109(B12).
- Eldholm, O., Thiede, J. and Taylor, E., 1989. Evolution of the Vøring volcanic margin. *Proc. ODP Sci. Results*, 104: 1033–1065.
- Eldursi, K., Branquet, Y., Guillou-Frottier, L. and Marcoux, E., 2009. Numerical investigation of transient hydrothermal processes around intrusions: Heat-transfer and fluid-circulation controlled mineralization patterns. *Earth and Planetary Science Letters*, 288(1-2): 70-83.

## Bibliography

---

- Emmanuel, S. and Berkowitz, B., 2007. Phase separation and convection in heterogeneous porous media: Implications for seafloor hydrothermal systems. *J. Geophys. Res.-Solid Earth*, 112(B5).
- Escartin, J., Smith, D.K., Cann, J., Schouten, H., Langmuir, C.H. and Escrig, S., 2008. Central role of detachment faults in accretion of slow-spreading oceanic lithosphere. *Nature*, 455(7214): 790-U795.
- Faerseth, R.B. and Lien, T., 2002. Cretaceous evolution in the Norwegian Sea - a period characterized by tectonic quiescence. *Mar. Pet. Geol.*, 19(8): 1005-1027.
- Fairley, J.P., 2009. Modeling fluid flow in a heterogeneous, fault-controlled hydrothermal system. *Geofluids*, 9(2): 153-166.
- Faleide, J.I., Tsikalas, F., Breivik, A.J., Mjelde, R., Ritzmann, O., Engen, O., Wilson, J. and Eldholm, O., 2008. Structure and evolution of the continental margin off Norway and Barents Sea. *Episodes*, 31(1): 82-91.
- Finlayson, B.A. and Scriven, L.E., 1965. The method of weighted residuals and its relation to certain variational principles for the analysis of transport processes. *Chemical Engineering Science*, 20(5): 395-404.
- Fisher, A.T., 2003. Geophysical Constraints on Hydrothermal Circulation. in *Dahlem Workshop Report, Energy and Mass Transfer in Marine Hydrothermal Systems*, edited by P. E. Halbach, V. Tunnicliffe and J. R. Hein: 29-52.
- Fisher, A.T., Becker, K. and Narasimhan, T.N., 1994. Off-axis hydrothermal circulation - parametric tests of a refined model of processes at deep-sea drilling project ocean drilling program site 504. *J. Geophys. Res.-Solid Earth*, 99(B2): 3097-3121.
- Fisher, A.T., Becker, K., Narasimhan, T.N., Langseth, M.G. and Mottl, M.J., 1990. Passive, off-axis convection through the southern flank of the costa-rica rift. *Journal of Geophysical Research-Solid Earth and Planets*, 95(B6): 9343-9370.
- Fjeldskaar, W., Helset, H.M., Johansen, H., Grunnaleiten, I. and Horstad, I., 2008. Thermal modelling of magmatic intrusions in the Gjallar Ridge,

- Norwegian Sea: implications for vitrinite reflectance and hydrocarbon maturation. *Basin Res.*, 20(1): 143-159.
- Fontaine, F.J. and Wilcock, W.S.D., 2007. Two-dimensional numerical models of open-top hydrothermal convection at high Rayleigh and Nusselt numbers: Implications for mid-ocean ridge hydrothermal circulation. *Geochem. Geophys. Geosyst.*, 8: 17.
- Forster, C. and Smith, L., 1988. Groundwater-flow systems in mountainous terrain .1. Numerical modeling technique. *Water Resources Research*, 24(7): 999-1010.
- Foulger, G.R., 2010. *Plates Vs Plumes: A Geological Controversy*. John Wiley & Sons.
- Fouquet, Y., 1997. Where are the large hydrothermal sulphide deposits in the oceans? *Phil. Trans. R. Soc. Lond.*, 355: 427-441.
- Fouquet, Y., Ondreas, H., Charlou, J.L., Donval, J.P., Radfordknoery, J., Costa, I., Lourenco, N. and Tivey, M.K., 1995. Atlantic lava lakes and hot vents. *Nature*, 377(6546): 201-201.
- Fowler, C. and Nisbet, E., 1982. The thermal background of metamorphism II. Simple two-dimensional conductive models. *Geoscience Canada*, 9: 208-214.
- Gabrielsen, R.H., Odinsen, T. and Grunnaleite, I., 1999. Structuring of the Northern Viking Graben and the More Basin; the influence of basement structural grain, and the particular role of the More-Trondelag Fault Complex. *Mar. Pet. Geol.*, 16(5): 443-465.
- Galushkin, Y.I., 1997. Thermal effects of igneous intrusions on maturity of organic matter: A possible mechanism of intrusion. *Org. Geochem.*, 26(11-12): 645-658.
- Garg, S.K. and Pritchett, J.W., 1977. On pressure-work, viscous dissipation and the energy balance relation for geothermal reservoirs. *Advances in Water Resources*, 1(1): 41-47.

## Bibliography

---

- Gay, A. and Berndt, C., 2007. Cessation/reactivation of polygonal faulting and effects on fluid flow in the Voring Basin, Norwegian Margin. *J. Geol. Soc.*, 164: 129-141.
- Gay, A., Mourgues, R., Berndt, C., Bureau, D., Planke, S., Laurent, D., Gautier, S., Lauer, C. and Loggia, D., 2012. Anatomy of a fluid pipe in the Norwegian Basin: initiation, propagation and 3D shape. submitted.
- Geiger, S., Driesner, T., Heinrich, C.A. and Matthai, S.K., 2006. Multiphase thermohaline convection in the earth's crust: I. A new finite element - Finite volume solution technique combined with a new equation of state for NaCl-H<sub>2</sub>O. *Transp. Porous Media*, 63(3): 399-434.
- Geiger, S., Robert, S., Matthai, S.K., Zoppou, C. and Burri, A., 2004. Combining finite element and finite volume methods for efficient multiphase flow simulations in highly heterogeneous and structurally complex geologic media. *Geofluids*, 4(4): 284-299.
- Geoffroy, L., 2005. Volcanic passive margins. *C. R. Geosci.*, 337(16): 1395-1408.
- Gernigon, L., Lucazeau, F., Brigaud, F., Ringenbach, J.C., Planke, S. and Le Gall, B., 2006. A moderate melting model for the Voring margin (Norway) based on structural observations and a thermo-kinematical modelling: Implication for the meaning of the lower crustal bodies. *Tectonophysics*, 412(3-4): 255-278.
- Gu, G.S., Dickens, G.R., Bhatnagar, G., Colwell, F.S., Hirasaki, G.J. and Chapman, A.G., 2011. Abundant Early Palaeogene marine gas hydrates despite warm deep-ocean temperatures. *Nat. Geosci.*, 4(12): 848-851.
- Habashi, W.G., Nguyen, V.N. and Bhat, M.V., 1991. EFFICIENT DIRECT SOLVERS FOR LARGE-SCALE COMPUTATIONAL FLUID-DYNAMICS PROBLEMS. *Comput. Meth. Appl. Mech. Eng.*, 87(2-3): 253-265.
- Hansen, J.P.V., Cartwright, J.A., Huuse, M. and Clausen, O.R., 2005. 3D seismic expression of fluid migration and mud remobilization on the Gjallar Ridge, offshore mid-Norway. *Basin Res.*, 17(1): 123-139.

- 
- Hartline, B.K. and Lister, C.R.B., 1981. Topographic forcing of supercritical convection in a porous-medium such as the oceanic-crust. *Earth and Planetary Science Letters*, 55(1): 75-86.
- Haymon, R.M., Fornari, D.J., Edwards, M.H., Carbotte, S.M., Wright, D. and Macdonald, K.C., 1991. Hydrothermal vent distribution along the East Pacific Rise crest (9°09'–54'N) and its relationship to magmatic and tectonic processes on fast-spreading mid-ocean ridges. *Earth and Planetary Science Letters*, 104(2-4): 513-534.
- Haymon, R.M., Koski, R.A. and Abrams, M.J., 1989. Hydrothermal discharge zones beneath massive sulfide deposits mapped in the Oman ophiolite. *Geology*, 17(6): 531-535.
- Hesselbo, S.P., Grocke, D.R., Jenkyns, H.C., Bjerrum, C.J., Farrimond, P., Bell, H.S.M. and Green, O.R., 2000. Massive dissociation of gas hydrate during a Jurassic oceanic anoxic event. *Nature*, 406(6794): 392-395.
- Hochstein, M.P. and Soengko, S., 1997. Magnetic anomalies associated with high temperature reservoirs in the Taupo Volcanic Zone (New Zealand). *Geothermics*, 26(1): 1-24.
- Ingebritsen, S.E., Geiger, S., Hurwitz, S. and Driesner, T., 2010. Numerical simulation of magmatic hydrothermal systems. *Rev. Geophys.*, 47: 33.
- Ingebritsen, S.E., Sanford, W.E. and Neuzil, C.E., 2006. *Groundwater flow in geologic processes*. Cambridge University Press (2nd edition).
- Iqbal, S., 2011. Galerkin's Finite Element Formulation of the System of Fourth-Order Boundary-Value Problems. *Numer. Meth. Part Differ. Equ.*, 27(6): 1551-1560.
- Iyer, K., Austrheim, H., John, T. and Jamtveit, B., 2008. Serpentinization of the oceanic lithosphere and some geochemical consequences: Constraints from the Leka Ophiolite Complex, Norway. *Chem. Geol.*, 249(1-2): 66-90.
- Iyer, K., Rupke, L.H. and Morgan, J.P., 2010. Feedbacks between mantle hydration and hydrothermal convection at ocean spreading centers. *Earth and Planetary Science Letters*, 296(1-2): 34-44.

## Bibliography

---

- Jupp, T. and Schultz, A., 2000. A thermodynamic explanation for black smoker temperatures. *Nature*, 403(6772): 880-883.
- Kawada, Y., Seama, N. and Urabe, T., 2011. The role of seamounts in the transport of heat and fluids: Relations among seamount size, circulation patterns, and crustal heat flow. *Earth and Planetary Science Letters*, 306(1-2): 55-65.
- Kelley, D.S., Karson, J.A., Blackman, D.K., Fruh-Green, G.L., Butterfield, D.A., Lilley, M.D., Olson, E.J., Schrenk, M.O., Roe, K.K., Lebon, G.T., Rivizzigno, P. and Party, A.T.S., 2001. An off-axis hydrothermal vent field near the Mid-Atlantic Ridge at 30 degrees N. *Nature*, 412(6843): 145-149.
- Kelley, D.S., Karson, J.A., Fruh-Green, G.L., Yoerger, D.R., Shank, T.M., Butterfield, D.A., Hayes, J.M., Schrenk, M.O., Olson, E.J., Proskurowski, G., Jakuba, M., Bradley, A., Larson, B., Ludwig, K., Glickson, D., Buckman, K., Bradley, A.S., Brazelton, W.J., Roe, K., Elend, M.J., Delacour, A., Bernasconi, S.M., Lilley, M.D., Baross, J.A., Summons, R.T. and Sylva, S.P., 2005. A serpentinite-hosted ecosystem: The lost city hydrothermal field. *Science*, 307(5714): 1428-1434.
- Kent, G.M., Harding, A.J. and Orcutt, J.A., 1993. Distribution of Magma Beneath the East Pacific Rise Between the Clipperton Transform and the 9°17N Deval From Forward Modeling of Common Depth Point Data. *J. Geophys. Res.*, 98(B8): 13945-13969.
- Kleinrock, M.C., Tucholke, B.E., Lin, J. and Tivey, M.A., 1997. Fast rift propagation at a slow-spreading ridge. *Geology*, 25(7): 639-642.
- Koschinsky, A., Garbe-Schonberg, D., Sander, S., Schmidt, K., Gennerich, H.H. and Strauss, H., 2008. Hydrothermal venting at pressure-temperature conditions above the critical point of seawater, 5 degrees S on the Mid-Atlantic Ridge. *Geology*, 36(8): 615-618.
- Lister, C.R.B., 1980. Heat-flow and hydrothermal circulation. *Annu. Rev. Earth Planet. Sci.*, 8: 95-117.
- Lowell, R.P., 1980. Topographically driven subcritical hydrothermal convection in the oceanic-crust. *Earth and Planetary Science Letters*, 49(1): 21-28.

- Lowell, R.P., 1991. Modeling continental and submarine hydrothermal systems. *Rev. Geophys.*, 29(3): 457-476.
- Lowell, R.P., Rona, P.A. and Vonherzen, R.P., 1995. Sea-floor hydrothermal systems. *J. Geophys. Res.-Solid Earth*, 100(B1): 327-352.
- Lundin, E.R. and Dore, A.G., 1997. A tectonic model for the Norwegian passive margin with implications for the NE Atlantic: Early Cretaceous to break-up. *J. Geol. Soc.*, 154: 545-550.
- Macdonald, K.C., 2001. *Mid-ocean ridge tectonics, volcanism and geomorphology*. Academic Press.
- Marques, A.F.A., Barriga, F. and Scott, S.D., 2007. Sulfide mineralization in an ultramafic-rock hosted seafloor hydrothermal system: From serpentinization to the formation of Cu-Zn-(Co)-rich massive sulfides. *Mar. Geol.*, 245(1-4): 20-39.
- Matthäi, S.K., 2003. Fluid flow and (reactive) transport in fractured and faulted rock. *Journal of Geochemical Exploration*, 78-79(0): 179-182.
- McInerney, F.A. and Wing, S.L., 2011. The Paleocene-Eocene Thermal Maximum: A Perturbation of Carbon Cycle, Climate, and Biosphere with Implications for the Future. In: R. Jeanloz and K.H. Freeman (Editors), *Annual Review of Earth and Planetary Sciences*, Vol 39. *Annual Review of Earth and Planetary Sciences*. Annual Reviews, Palo Alto, pp. 489-516.
- McKenzie, J.A., 2003. Bridging geochemistry and microbiology through ocean drilling. *Goldsmid Conference abstracts*.
- Melchert, B., Devey, C.W., German, C.R., Lackschewitz, K.S., Seifert, R., Walter, M., Mertens, C., Yoerger, D.R., Baker, E.T., Paulick, H. and Nakamura, K., 2008. First evidence for high-temperature off-axis venting of deep crustal/mantle heat: The Nibelungen hydrothermal field, southern Mid-Atlantic Ridge. *Earth and Planetary Science Letters*, 275(1-2): 61-69.
- Mjelde, R., Digranes, P., Shimamura, H., Shiobara, H., Kodaira, S., Brekke, H., Egebjerg, T., Sorenes, N. and Thorbjornsen, S., 1998. Crustal structure

## Bibliography

---

- of the northern part of the Voring Basin, mid-Norway margin, from wide-angle seismic and gravity data. *Tectonophysics*, 293(3-4): 175-205.
- Morgan, J.P. and Chen, Y.J., 1993. The genesis of oceanic-crust - magma injection, hydrothermal circulation, and crustal flow. *J. Geophys. Res.-Solid Earth*, 98(B4): 6283-6297.
- Morgan, J.P., Parmentier, E.M. and Lin, J., 1987. Mechanisms for the origin of mid-ocean ridge axial topography - implications for the thermal and mechanical structure of accreting plate boundaries. *Journal of Geophysical Research-Solid Earth and Planets*, 92(B12): 12823-12836.
- Morrow, D.W. and Issler, D.R., 1993. Calculation of vitrinite reflectance from thermal histories - a comparison of some methods. *AAPG Bull.-Am. Assoc. Petr. Geol.*, 77(4): 610-624.
- Murton, B.J., Klinkhammer, G., Becker, K., Briais, A., Edge, D., Hayward, N., Millard, N., Mitchell, I., Rouse, I., Rudnicki, M., Sayanagi, K., Sloan, H. and Parson, L., 1994. Direct evidence for the distribution and occurrence of hydrothermal activity between 27-degrees-n-30-degrees-n on the mid-Atlantic ridge. *Earth and Planetary Science Letters*, 125(1-4): 119-128.
- Mutter, J.C., Buck, W.R. and Zehnder, C.M., 1988. Convective partial melting .1. A model for the formation of thick basaltic sequences during the initiation of spreading. *Journal of Geophysical Research-Solid Earth and Planets*, 93(B2): 1031-1048.
- Narasimhan, T.N. and Witherspoon, P.A., 1976. An integrated finite difference method for analyzing fluid flow in porous media. *Water Resour. Res.*, 12(1): 57-64.
- Nicolas, A., Mainprice, D. and Boudier, F., 2003. High-temperature seawater circulation throughout crust of oceanic ridges: A model derived from the Oman ophiolites. *J. Geophys. Res.-Solid Earth*, 108(B8).
- Ondreas, H., Cannat, M., Fouquet, Y., Normand, A., Sarradin, P.M. and Sarrazin, J., 2009. Recent volcanic events and the distribution of hydrothermal venting at the Lucky Strike hydrothermal field, Mid-Atlantic Ridge. *Geochem. Geophys. Geosyst.*, 10: 18.

- Patankar, S.V. and Baliga, B.R., 1978. A New Finite-Difference Scheme for Parabolic Differential Equations. *Numerical Heat Transfer, Part B: Fundamentals*, 1(1): 27-37.
- Polyansky, O.P. and Reverdatto, V.V., 2006. Contact metamorphism and metasomatism near the Talnakh intrusion: Fluid convection and heat transfer modeling on the basis of the finite-difference method. *Dokl. Earth Sci.*, 411(9): 1480-1484.
- Polycarpou, A.C., 2006. Introduction to the finite element method in electromagnetics. *Synthesis Lectures on Computational Electromagnetics*.
- Reemst, P. and Cloetingh, S., 2000. Polyphase rift evolution of the Voring margin (mid-Norway): Constraints from forward tectonostratigraphic modeling. *Tectonics*, 19(2): 225-240.
- Ren, S.C., Skogseid, J. and Eldholm, O., 1998. Late Cretaceous-Paleocene extension on the Voring Volcanic Margin. *Mar. Geophys. Res.*, 20(4): 343-369.
- Robert, P., 1981. *Organic Metamorphism and Geothermal History*. Elf-Aquitaine and D. Reidel Publishing Company, Dordrecht.
- Roberts, D.G., Thompson, M., Mitchener, B., Hossack, S., Carmichael, S. and Bjørnseth, H.-M., 1999. Palaeozoic to Tertiary rift and basin dynamics: mid-Norway to the Bay of Biscay-a new concept for hydrocarbon prospectivity in the deep water frontier. In: *Petroleum Geology of Northwest Europe: Proceedings of the 5th Conference* (Ed. by A.J. Fleet & S.A.R. Boldy), Geol. Soc. Lond., 1: 7-40.
- Rupke, L.H., Schmalholz, S.M., Schmid, D.W. and Podiadchikov, Y.Y., 2008. Automated thermotectonostratigraphic basin reconstruction: Viking Graben case study. *AAPG Bull.*, 92(3): 309-326.
- Rupke, L.H., Schmid, D.W., Hartz, E.H. and Martinsen, B., 2010. Basin modelling of a transform margin setting: structural, thermal and hydrocarbon evolution of the Tano Basin, Ghana. *Petrol. Geosci.*, 16(3): 283-298.

## Bibliography

---

- Schmidt, K., Koschinsky, A., Garbe-Schonberg, D., de Carvalho, L.M. and Seifert, R., 2007. Geochemistry of hydrothermal fluids from the ultramafic-hosted Logatchev hydrothermal field, 15 degrees N on the Mid-Atlantic Ridge: Temporal and spatial investigation. *Chemical Geology*, 242(1-2): 1-21.
- Schoofs, S. and Hansen, U., 2000. Depletion of a brine layer at the base of ridge-crest hydrothermal systems. *Earth and Planetary Science Letters*, 180(3-4): 341-353.
- Sclater, J.G., Jaupart, C. and Galson, D., 1980. The heat-flow through oceanic and continental-crust and the heat-loss of the Earth. *Rev. Geophys.*, 18(1): 269-&.
- Searle, R.C., Keeton, J.A., Owens, R.B., White, R.S., Mecklenburgh, R., Parsons, B. and Lee, S.M., 1998. The Reykjanes Ridge: structure and tectonics of a hot-spot-influenced, slow-spreading ridge, from multibeam bathymetry, gravity and magnetic investigations. *Earth and Planetary Science Letters*, 160(3-4): 463-478.
- Segerlind, L.J., 1989. Weighted residual solutions in the time domain. *International Journal For Numerical Methods In Engineering*, 28(3): 679-685.
- Shin, S. and Juric, D., 2002. Modeling three-dimensional multiphase flow using a level contour reconstruction method for front tracking without connectivity. *J. Comput. Phys.*, 180(2): 427-470.
- Simoneit, B.R.T., Brenner, S., Peters, K.E. and Kaplan, I.R., 1981. Thermal alteration of cretaceous black shale by diabase intrusions in the eastern atlantic .2. Effects on bitumen and kerogen. *Geochim. Cosmochim. Acta*, 45(9): 1581-1602.
- Singh, S.C., Crawford, W.C., Carton, H., Seher, T., Combier, V., Cannat, M., Canales, J.P., Dusunur, D., Escartin, J. and Miranda, J.M., 2006. Discovery of a magma chamber and faults beneath a Mid-Atlantic Ridge hydrothermal field. *Nature*, 442(7106): 1029-1032.
- Skogseid, J., Pedersen, T., Eldholm, O. and Larsen, V.B., 1992. Tectonism and magmatism during NE Atlantic continental breakup: the Vøring Margin. In: *Magmatism and the Causes of Continental Break-up* (Ed. by B.C. Sorey, et al.) *Geol. Soc. Spec. Publ.*, 68: 305–320.

- Smith, D.K. and Cann, J.R., 1992. The role of seamount volcanism in crustal construction at the mid-atlantic ridge (24-degrees-30-degrees-N). *J. Geophys. Res.-Solid Earth*, 97(B2): 1645-1658.
- Sohn, R.A., Hildebrand, J.A., Webb, S.C. and Fox, C.G., 1995. Hydrothermal microseismicity at the megaplume site on the southern Juan-de-fuca ridge. *Bulletin of the Seismological Society of America*, 85(3): 775-786.
- Stein, C.A. and Stein, S., 1994. Constraints on hydrothermal heat-flux through the oceanic lithosphere from global heat-flow. *J. Geophys. Res.-Solid Earth*, 99(B2): 3081-3095.
- Svensen, H., Planke, S. and Corfu, F., 2010. Zircon dating ties NE Atlantic sill emplacement to initial Eocene global warming. *J. Geol. Soc.*, 167(3): 433-436.
- Svensen, H., Planke, S., Malthe-Sorensen, A., Jamtveit, B., Myklebust, R., Eidem, T.R. and Rey, S.S., 2004. Release of methane from a volcanic basin as a mechanism for initial Eocene global warming. *Nature*, 429(6991): 542-545.
- Sweeney, J.J. and Burnham, A.K., 1990. Evaluation of a simple-model of vitrinite reflectance based on chemical-kinetics. *AAPG Bull.-Am. Assoc. Petr. Geol.*, 74(10): 1559-1570.
- Syam, M.I. and Attili, B.S., 2006. Weighted residual method for obtaining positive solutions of two-point nonlinear boundary value problems. *Appl. Math. Comput.*, 176(2): 775-784.
- Theissen-Krah, S., Iyer, K., Rüpke, L. and Morgan, J.P., 2011. Coupled mechanical and hydrothermal modeling of crustal accretion at intermediate to fast spreading ridges. *Earth and Planetary Science Letters*, 311(3-4): 275-286.
- Tissot, B. and Espitalie, J., 1975. Thermal evolution of organic-matter in sediments - application of a mathematical simulation - petroleum potential of sedimentary basins and reconstructing thermal history of sediments. *Rev. Inst. Fr. Pet.*, 30(5): 743-777.

## Bibliography

---

- Tivey, M.A., 1994. High-resolution magnetic survey over the Middle Valley mounds, northern Juan de Fuca Ridge. *Proc. Ocean Drill. Program, Sci. Results*: 29-34.
- Tivey, M.A., 2008. The Magnetic Signature of Hydrothermal Systems in Slow Spreading Environments. . *Geophysical Monograph Series*, 188.
- Tivey, M.K., 1998. How to build a black smoker chimney. . *Oceanus*, 41(2): 22-26.
- Tivey, M.K., 2007. Generation of Seafloor Hydrothermal Vent Fluids and Associated Mineral Deposits. *Oceanography*, 20(1): 50-65.
- Todesco, M. and Berrino, G., 2005. Modeling hydrothermal fluid circulation and gravity signals at the Phlegraean Fields caldera. *Earth and Planetary Science Letters*, 240(2): 328-338.
- Tolstoy, M., Bohnenstiehl, D.R., Edwards, M.H. and Kurras, G.J., 2001. Seismic character of volcanic activity at the ultraslow-spreading Gakkel Ridge. *Geology*, 29(12): 1139-1142.
- Tolstoy, M., Waldhauser, F., Bohnenstiehl, D.R., Weekly, R.T. and Kim, W.Y., 2008. Seismic identification of along-axis hydrothermal flow on the East Pacific Rise. *Nature*, 451(7175): 181-U187.
- Toomey, D.R., Solomon, S.C. and Purdy, G.M., 1994. Tomographic imaging of the shallow crustal structure of the East Pacific Rise at 9°30 N. *J. Geophys. Res.*, 99(B12): 24135-24157.
- Tu, J., Heng Yeoh, G. and Liu, C., 2008. *Computational Fluid Dynamics: A Practical Approach*. Elsevier.
- Tufar, W., Tufar, E. and Lange, J., 1986. Ore paragenesis of recent hydrothermal deposits at the cocos-nazca plate boundary (galapagos rift) at 85-degrees 51' and 85-degrees 55' W - complex massive sulfide mineralizations, non-sulfidic mineralizations and mineralized basalts. *Geol. Rundsch.*, 75(3): 829-861.
- Ungerer, P., Burrus, J., Doligez, B., Chenet, P.Y. and Bessis, F., 1990. Basin evaluation by integrated 2-dimensional modeling of heat-transfer, fluid-

- flow, hydrocarbon generation, and migration. *AAPG Bull.-Am. Assoc. Petr. Geol.*, 74(3): 309-335.
- Vogt, P.R. and Avery, O.E., 1974. Detailed magnetic surveys in Northeast Atlantic and Labrador-sea. *Journal of geophysical Research*, 79(2): 363-389.
- Von Damm, K.L., Lilley, M.D., Shanks, W.C., Brockington, M., Bray, A.M., O'Grady, K.M., Olson, E., Graham, A., Proskurowski, G. and Sou, E.P.R., 2003. Extraordinary phase separation and segregation in vent fluids from the southern East Pacific Rise. *Earth and Planetary Science Letters*, 206(3-4): 365-378.
- Von Herzen, R.P. and Uyeda, S., 1963. Heat flow through the eastern Pacific ocean floor. . *Journal of Geophysical Research*, 68.
- Vondamm, K.L., 1990. Seafloor Hydrothermal Activity - Black Smoker Chemistry and Chimneys. *Annual Review of Earth and Planetary Sciences*, 18: 173-204.
- Wang, X.T., Zhai, S.K., Meng, F.S., Li, H.M., Yu, Z.H., Sun, G. and Xue, G., 2006. Influence of permeability on hydrothermal circulation in the sediment-buried oceanic crust. *Sci. China Ser. D-Earth Sci.*, 49(7): 773-784.
- White, R.S., Spence, G.D., Fowler, S.R., McKenzie, D.P., Westbrook, G.K. and Bowen, A.N., 1987. Magmatism at rifted continental margins. *Nature*, 330(6147): 439-444.
- Wilcock, W.S.D., 1998. Cellular convection models of mid-ocean ridge hydrothermal circulation and the temperatures of black smoker fluids. *J. Geophys. Res.-Solid Earth*, 103(B2): 2585-2596.
- Ziegler, P.A., 1988. *AAPG Memoir 43* AAPG Memoir 43, AAPG, Tulsa, OK.
- Zierenberg, R., A, Adams, M.W.W., Arp, A.J., 2000. Life in extreme environments: Hydrothermal vents. *National Academy of Sciences of the USA*, 97(24).

## Bibliography

---

Zyvoloski, G.A., Robinson, B.A., Dash, Z.V. and Trease, L.L., 1996. Users Manual for the FEHMN Application. Los Alamos National Laboratory, LA-UR-94-3788.

# Curriculum Vitae

## Nasser Bani Hassan

+49 (176) 70187795

*Gabelsbergerstr.19, 24148 Kiel, Germany.*

*nbanihassan@geomar.de*

### **EDUCATIONAL BACKGROUND**

- **2008-2012:** PhD in Geophysics at Christian-Albrechts-University (CAU), Helmholtz centre for ocean research (GEOMAR), Kiel, Germany (Provisional confirmation).
- **2004-2006:** MSc in Geophysics (Exploration Seismology) at University of Tehran, Iran.
- **1997-2002:** BSc in Physics at Ferdowsi University of Mashhad, Iran.

### **WORK EXPERIENCES**

- Processing representative; National Iranian Oil Company (NIOC), (one year).
- Seismic data processing and onshore field QC in Koohestan-1 2D project; Terras Persia Seismic (TPS) Company (two years).